Feature Extraction of Moving Automotive Vehicles using Multi-Target Tracking on Polarimetric Doppler Radar Data

D. A. Bosma

Technische Universiteit Delft

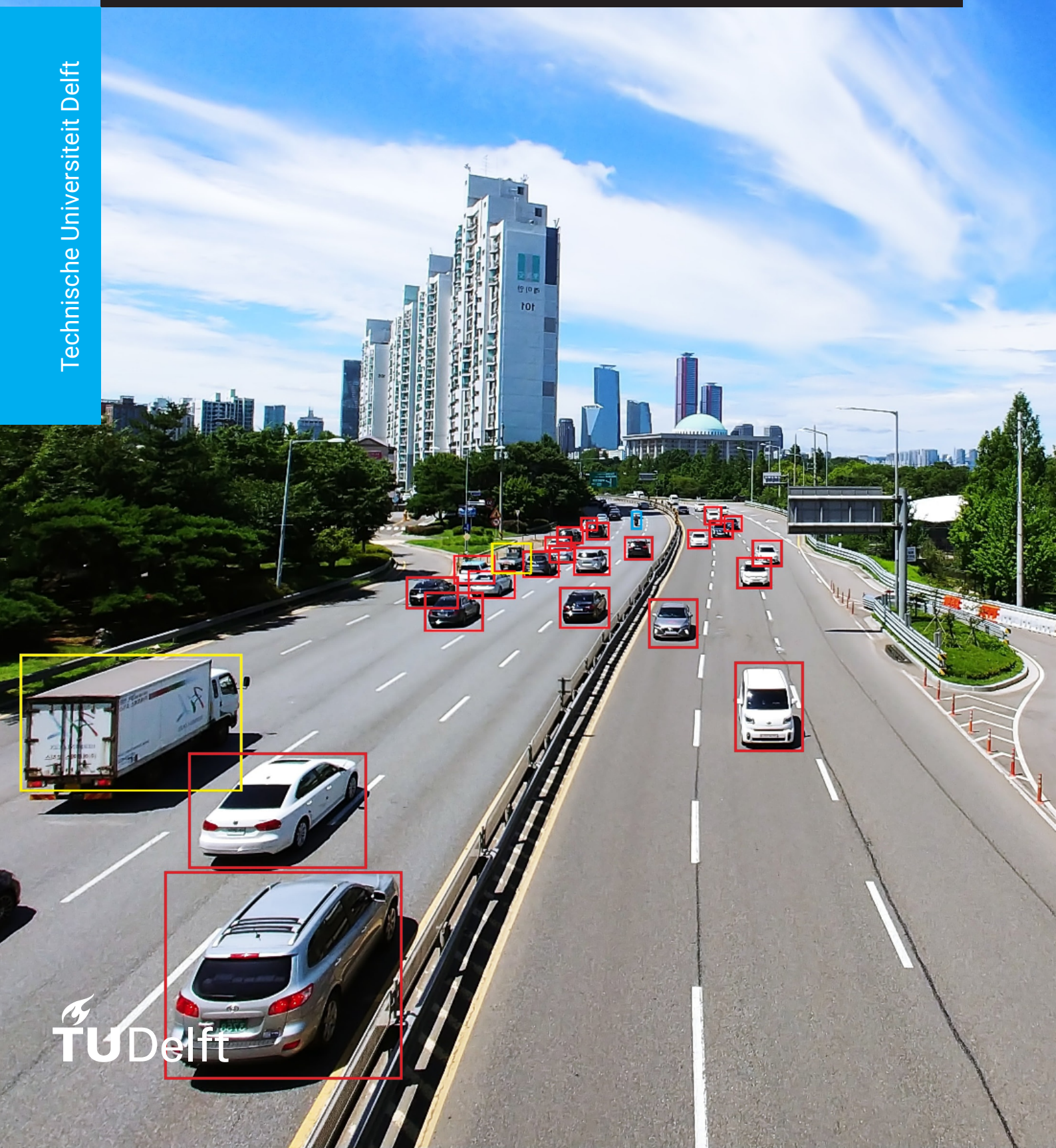

TU Delft

Feature Extraction of Moving Automotive Vehicles using Multi-Target Tracking on Polarimetric Doppler Radar Data

by

Detmer Bosma

to obtain the degree of Master of Science

at the Delft University of Technology,

to be defended publicly on November 19, 2021 at 09:30 AM.

Student number:	4347536	
Master programme:	MSc. Electrical Engineering - Signals & Systems	
Project duration:	March 1, 2021 – November 19, 2021	
Thesis committee:	prof. dr. A. Yarovoy,	TU Delft (MS3), Professor, chair
	dr. O. A. Krasnov,	TU Delft (MS3), Assistant Professor, supervisor
	dr. ir. J. Dauwels,	TU Delft (CAS), Associate Professor

An electronic version of this thesis is available at `http://repository.tudelft.nl/`.

Cover image description: Detection and classification of vehicles on a highway of different sub-classes, indicated by colored boxes [1]

TU Delft

Abstract

Nowadays, many practical radar applications require an automatic interpretation of the received data, including data processing algorithms and target classification. The exploitation of additional polarimetric information is a very promising concept to improve the performance of automotive target classification. In this thesis work, we aim to identify target features that can be used for the classification and definition of sub-classes of moving automotive vehicles driving on a highway. This analysis is based on a multi-dimensional polarimetric feature database, created from real observations from a fully polarimetric-Doppler S-band FMCW radar (PARSAX). The polarimetric information of the vehicles is extracted while tracking the targets in a multi-target environment in the range-Doppler domain. Therefore, a multi-target tracking algorithm, based on an OS-CFAR detector, polarimetric data fusion algorithm, and a classical Kalman filter, is used. In order to cope with Doppler ambiguity, a novel MHT-based approach has been introduced.

The feature extraction analysis shows that the polarimetric features of the observed targets provide well-defined reliable statistical relations between physically related features, but that blind classification based on our target feature database does not provide new insights that are useful for classification. Reliable clusters that are useful to describe the polarimetric signatures of the targets have not been found, except the polarimetric correlation coefficients, which, unfortunately, despite their physical clear sense, were not supported by the other analyzed features. Nevertheless, from similar feature analysis, it has been shown that the features originating from the incoherent polarimetric $H/A/\alpha$-decomposition form compact and well-separated clusters corresponding to target scattering and clutter scattering. Therefore, it can be concluded that these features can be used to accurately distinguish moving vehicles from static clutter.

Preface

With this thesis research project, an end has come to my studies at TU Delft. I would like to thank a few people that helped me through this entire process of the thesis project. I would like to express my gratitude to my supervisor dr. O. A. Krasnov for all his assistance, discussions, and helpful suggestions during the last couple of months. I enjoyed working with him and I really appreciated all his help, especially his assistance during the last weeks in order to finalize this research. I also would like to thank prof. dr. A. Yarovoy, the chair of the MS3 department. He completely guided me through the last year of my MSc. Electrical Engineering, inspired me to do my thesis project at his department and connected my interests to this thesis' topic. At last, I want to thank my family and friends, for supporting me during the whole process and accompanying me while enjoying many, many cups of coffee.

Detmer Bosma
Delft, November 2021

Contents

Page

Abstract **iii**

Preface **v**

List of Abbreviations **viii**

1 Introduction **1**
1.1 Motivation and goals . . . 1
1.2 Research problem definition . . . 2
1.3 Overview of the state-of-the-art . . . 3
1.4 Research novelty . . . 6
1.5 Thesis structure . . . 7

2 Radar Theory and Background **9**
2.1 A brief overview of radar fundamentals . . . 9
2.1.1 Basic principle of radar . . . 9
2.1.2 The radar equation . . . 11
2.1.3 Performance metrics . . . 12
2.1.4 FMCW radar . . . 13
2.2 Basic concept of radar polarimetry . . . 15
2.2.1 Plane waves and polarization . . . 15
2.2.2 Polarization Scattering Matrix . . . 16
2.2.3 Polarimetric radar . . . 17
2.3 Signal processing using PARSAX radar data . . . 18
2.3.1 Fully polarimetric radar PARSAX . . . 18
2.3.2 PARSAX characteristics . . . 19
2.3.3 Two-dimensional Fourier Transform . . . 20
2.3.4 Moving Target Indicator . . . 21
2.4 Conclusion . . . 22

3 Method for Feature Database Creation **23**
3.1 Target detection algorithm . . . 23
3.1.1 Basic detection theory . . . 23
3.1.2 Non-adaptive detector . . . 24
3.1.3 Constant False Alarm Rate (CFAR) detector . . . 25
3.1.4 Target detection in PARSAX radar data . . . 28
3.1.5 Improvements of detection algorithm . . . 30
3.2 Polarimetric sensor fusion . . . 33
3.2.1 Concept of sensor fusion . . . 33
3.2.2 Polarimetric data fusion . . . 33
3.2.3 Detection decision fusion . . . 36
3.2.4 Comparison sensor fusion methods . . . 36
3.3 Target clustering algorithm . . . 38

3.4 Multi-target tracking in range-Doppler domain . . . 39
3.4.1 Filtering and prediction: Measurement model . . . 40
3.4.2 Filtering and prediction: Kalman filter . . . 41
3.4.3 Filtering and prediction: State dynamics model . . . 41
3.4.4 Gating computations . . . 42
3.4.5 Measurement-to-track association: Method . . . 43
3.4.6 Measurement-to-track association: MHT with Doppler ambiguity . . . 45
3.4.7 Track management . . . 47
3.4.8 Simulation of multi-target tracking algorithm . . . 48
3.5 Feature database creation . . . 51
3.6 Conclusion . . . 52

4 Results of Feature Extraction **55**
4.1 Introduction to unsupervised learning approaches . . . 55
4.2 Analysis of target feature database . . . 57
4.2.1 Analysis of amplitude information . . . 57
4.2.2 Analysis of correlation between polarization channels . . . 58
4.2.3 Analysis of target length . . . 60
4.2.4 Analysis of target dynamics . . . 60
4.3 Feature database extension by polarimetric decomposition . . . 61
4.3.1 Huynen decomposition . . . 61
4.3.2 $H/A/\alpha$ decomposition . . . 61
4.3.3 Pauli decomposition . . . 64
4.3.4 Krogager decomposition . . . 65
4.4 Target feature extraction . . . 67
4.4.1 Normalization and standardization . . . 67
4.4.2 Clustering tendency . . . 67
4.4.3 Clustering quality . . . 69
4.4.4 Preliminary classification . . . 72
4.4.5 Preliminary conclusion of target feature extraction . . . 76
4.5 Resulted clutter features . . . 77
4.6 Conclusion . . . 79

5 Conclusion and Future Work **83**

Bibliography **87**

A PARSAX System and Signal Processing **93**

B CFAR detection maps **99**

C Signal- and data processing overview **101**

D Feature extraction analysis **103**

List of Abbreviations

ACC Adaptive Cruise Control.

ADAS Advanced Driving Assistance Systems.

ADC Analog-to-Digital Converter.

AEB Automotic Emergency Braking.

AICC Autonomous Intelligent Cruise Control.

CA Constant Acceleration.

CA-CFAR Cell Averaging CFAR.

CFAR Constant False Alarm Rate.

CNN Convolutional Neural Network.

DBSCAN Density-Based Spatial Clustering of Applications with Noise.

DoP Degree of Polarization.

FFT Fast Fourier Transform.

FMCW Frequency-Modulated Continuous-Wave.

GNN Global Nearest Neighbor.

GOCA-CFAR Greatest of Cell Averaging CFAR.

HPF High-Pass Filter.

ICA Independent Component Analysis.

IF Intermediate Frequency.

JPDA Joint Probabilistic Data Association.

LFM Linearly Frequency Modulated.

LHC Left-hand Circulation.

LRT Likelihood Ratio Test.

MHT Multiple Hypotheses Tracking.

MSE Mean-Square Error.

MTI Moving Target Indicator.

MTT Multiple Target Tracking.

NN Nearest Neighbor.

OPD Optimal Polarimetric Detector.

OS-CFAR Ordered Statistics CFAR.

PCA Principal Component Analysis.

PDA Probabilistic Data Association.

PDF Probability Density Function.

PMF Polarimetric Matched Filter.

PMSD Polarimetric Maximization Synthesis Detector.

PRF Pulse Repetition Frequency.

PRI Pulse Repetition Interval.

PSM Polarization Scattering Matrix.

PWF Polarization Whitening Filter.

RADAR Radio Detection and Ranging.

RCS Radar Cross Section.

RF Radio Frequency.

RHC Right-hand Circulation.

RMSE Root Mean Square Error.

ROC Receiver Operating Characteristic.

SAR Synthetic Aperture Radar.

SD Span Detector.

SINR Signal-to-Interference-plus-Noise Ratio.

SLRT Sequential Likelihood Ratio Test.

SNR Signal-to-Noise Ratio.

SOCA-CFAR Smallest of Cell Averaging CFAR.

SPRT Sequential Probability Ratio Test.

SVM Support Vector Machine.

1

Introduction

1.1. Motivation and goals

The futuristic concept of using autonomously driving vehicles in our daily lives becomes more realistic each day, because of big improvements in low-cost, high-performance technologies and due to the global growth of the human population, causing a stressful impact on our transportation infrastructure. A bigger population leads to an increasing number of vehicles and expanding infrastructure, resulting in more need for driver and driving safety. Despite the efforts of many governments to make use of existing technologies in order to improve road safety, the number of fatal road accidents keeps increasing, mainly caused by human errors. The technology behind autonomously driving vehicles is being explored to reduce these life-threatening situations on the road, making human transportation safer, more reliable, and more comfortable. These *smart* cars have many advantageous features, such as navigating on the road without human input by sensing the surrounding environment, performing quick maneuvers with a significantly short reaction time, and assisting the driver to drive safely and comfortably [2].

One of the most promising technologies for autonomous vehicles is radar. In modern technology of remote sensing, the number of possibilities with radar systems becomes bigger and bigger. While radar technology was mainly developed for military and surveillance applications during the 20^{th} century [3], nowadays it plays a significant role as a sensor in remote sensing (e.g., air- and road traffic control) [4], medical applications (e.g., cancer detection and tumor localization), robotics [5], and, obviously, in the automotive industry. Radar is hardly not affected by weather conditions and daylight, which is a promising feature for automotive applications. In the last decades, the automotive industry achieved big improvements with respect to reliability, safety, and costs of radar systems for autonomous vehicles, resulting in a greatly increasing popularity of autonomously driving cars. Although a lot of technical and non-technical challenges are still present, car manufacturers already succeeded in implementing advanced driver-assisting systems (ADAS), such as adaptive cruise control (ACC), autonomous emergency brake (AEB), and blind-spot detection [2]. Besides radar systems being used for these short- and medium-range applications, radars can also be utilized for long-range surveillance purposes, for example, to scan the environment at a traffic crossing or a parking spot [6].

One of these main challenges is the automatic tracking and classification of objects of interest observed by the radar, also known as targets. In this project, we are interested in advancing the state-of-the-art in automatic target detection, tracking and classification by exploiting modern polarimetric waveforms. These waveforms facilitate the ability to measure all four elements of the polarization scattering matrix (PSM) simultaneously. These elements consist of complex data, meaning

that both amplitude and phase information of the received signals are provided [7]. Radars capable of measuring these polarimetric characteristics of targets provide valuable additional information for more reliable target detection, more accurate target identification, and better parameter estimation. The exploitation of polarimetric-Doppler characteristics is a very promising concept for automotive target classification and can be applied in both automotive radar and surveillance radar applications, such as road traffic control and monitoring [8] or feature-aided tracking of vehicles [9].

The main goal of this thesis is to identify polarimetric target features that can contribute to the classification and definition of sub-classes of automotive targets driving on a highway from small compact cars to large trucks, based on a feature database extracted from real observations of a polarimetric-Doppler radar (PARSAX). To achieve this goal, the implementation and adaptation of radar data processing algorithms for reliable multi-target clustering and tracking of the observed targets in the range-Doppler domain are required. Subsequently, based on the polarimetric-Doppler characteristics of the moving targets, a multi-dimensional polarimetric feature database will be created, which can be used for target classification algorithms. This leads to the following sub-goals:

1. To be able to detect each target and to improve the detection performance by fusion of the data sets formed by the four polarization elements.
2. To be able to track each target within the complex multi-target situation during the time that a target is within the radar field of view and extract the timeline of polarimetric data.
3. To create a database of the polarimetric-Doppler characteristics of moving targets to identify target features can contribute to the classification of moving automotive vehicles.
4. To perform an analysis of the possibility and performance of the use of polarimetric features for the classification of moving automotive vehicles into an experimentally-defined set of classes.

1.2. Research problem definition

Nowadays, many practical radar applications require an automatic interpretation of the received data, including data processing algorithms for automatic tracking and classification of objects of interest, also called targets. Many classification algorithms are lacking due to a shortage of labeled data sets and information about the characteristics of the object of interest. The accuracy and the reliability of the classification of moving automotive vehicles can significantly be improved by exploiting the polarimetric scattering information of these vehicles. To provide the classifier with this information, the polarimetric signatures of moving automotive vehicles need to be known.

During this thesis project, a feature database of polarimetric Doppler radar data will be created through collecting data of moving automotive targets from the fully polarimetric-Doppler S-band FMCW radar PARSAX. A unique feature of the PARSAX radar is its ability to measure all four elements of the PSM *simultaneously* during one sounding sweep by using dual-orthogonal digitally-generated sounding signals. This property will be exploited in two stages. Firstly, in order to create this feature database, it is required to detect and track each target in the range-Doppler domain of the given data. The polarization information shall be used to improve the target detection and tracking. Secondly, the amplitude and phase information over time of each target's complex data point(s) of all polarization elements will be extracted and collected for feature extraction analysis. From this analysis, the possibility to identify polarimetric target features that can contribute to the classification and definition of sub-classes of moving automotive targets will be investigated.

1.3. Overview of the state-of-the-art

In this section, the state-of-the-art of polarimetric features and attributes of automotive targets for classification purposes will be described. A brief overview of the history of polarization-based detection and classification will be given, after which all research on polarimetric signatures of automotive targets will be discussed in detail. Subsequently, a few other applications of polarization-based classification in the automotive sector will be described shortly. Finally, the current problems and limitations of these studies will be summarized and the novelties of this project will be presented.

In 1960 the first article that described the fundamentals of classification using polarimetric properties was published by Copeland [10]. Because of the advancing technology of polarimetric radar being able to provide full polarimetric data, in the next oncoming years, many papers, articles and books followed, introducing new concepts of exploiting polarimetric information for object identification and classification [11–14]. Later on, theoretical insights from among others Huynen [15, 16] and Boerner [17–19] brought new impulses into radar polarimetry theory and its relations with target identification problems. According to Huynen's theorem, the dynamic behavior of the scattering matrix can be considered for polarization-based target classification and identification, provided that a complete measurement of the PSM is available [20].

During these years, many synthetic aperture radar (SAR) applications already made improvements to their classification performances (classification of e.g., earth terrain, [21–23], military vehicles [24] and other ground vehicles [25]) by adding polarimetric features to the obtained radar information [8]. A few decades ago, scientists and engineers in the automotive sector started to investigate detection and classification systems using full polarimetric radar sensors as well. Early experiments were mainly focused on road surface classification, which can be used to inform the driver about critical road situations (e.g., aquaplaning, snow and icy surfaces) [26–28], and detection of road debris and faults that could lead to fatal accidents and damage of property [29].

Furthermore, experiments on the classification of automotive vehicles were conducted as well. Nevertheless, based on the results of [30], where only the ratio of the co-polarized and cross-polarized amplitudes have been considered to be useful, it was found that similar classification could be achieved by only using the co-polarized signals. For that reason, the use of polarimetric information would not be cost-effective. However, a significant and crucial part of the polarimetric information for classification purposes, such as the complete complex PSM, was not used. Fortunately, due to the increasing interest in automated driving, automotive polarization radar sensors became more popular for many applications. All these applications have in common that they increase the safety and comfort of the driver by contributing to the reliability of ADAS, e.g., Autonomous Intelligent Cruise Control (AICC) and Automatic Emergency Braking (AEB). In order to improve these system performances, automatic traffic scene interpretation is required, where classification of automotive vehicles is an important processing task [31]. In the past ten years, a lot of research on polarimetric features of automotive vehicles has been carried out.

For the purpose of having suitable vehicle models for radar simulations, Schipper et al. provided measurements of the radar cross-section (RCS) of several automotive vehicles (e.g., motor scooter, small cars, estate cars, vans, etc.) using a full polarimetric radar operating in the frequency range from 23 GHz to 27 GHz. These measurements were performed in an anechoic chamber, where the targets were placed on top of a turntable, as can be seen in Fig. 1.1. From the results, it can be seen that reflections measured in the co-polarized configuration have a higher return amplitude than measurements in the cross-polarized configuration. Moreover, they show that the horizontally polarized reflections of two-wheeled vehicles (e.g., bicycles, motor scooters, etc.) have an increased amplitude compared to vertically polarized reflections. The RCS of four-wheeled vehicles with a comparable size is similar, regardless of the angle aspect when measured in the horizontally polar-

(a) (b) (c)

Figure 1.1: An anechoic chamber with a large turntable to provide measurements of automotive vehicles for different angle aspects, with (a) a small car (VW Golf V), (b) a large car (Audi A4 estate) and (c) a motorbike [32]

ized configuration. As can be expected, the van tends to have a larger RCS, especially when pointing the radar towards the side of the vehicle. Unfortunately, vertically polarized measurements are not shown [32].

In [33, 34], Geary et al. performed measurements on static automotive target signatures as a function of polarization in both the K-band (22 GHz to 29 GHz) and the W-band (76 GHz to 81 GHz) frequencies. It can be seen that reflections of the horizontal polarized electromagnetic waves show a less noisy frequency response and ground clutter return compared to vertical polarization, especially for the K-band frequencies. From this, it can be stated that horizontal polarization is less sensitive to clutter characteristics from real-world roads. When several automotive targets (e.g., sedan, van, pick-up truck, etc.) were placed in front of the radar, it appears that for each target its peak return amplitude is relatively polarization independent. Unfortunately, no comparison between horizontal and vertical polarization among the return amplitudes of all targets was made. Despite this, the results for horizontal polarization show that the RCS of the vehicles do not differ significantly from each other, in both frequency bands. They have also concluded that the RCS, and thus the return signal amplitude, is strongly affected by the orientation of a target vehicle, especially for the W-band frequencies.

According to Trummer et al., this dependency on the relative orientation and geometrical shape can be minimized by extending automotive radar sensors to circular polarization, instead of linear polarization. When transmitting and receiving both right-hand circulation (RHC) and left-hand circulation (LHC) polarized waves, both orthogonal signal components can be analyzed for target classification. The data originated from RHC and LHC can be combined to improve the information quality about the surface of the target [35]. However, isolation of these two polarizations, defined by the cross-polarization discrimination, poses a challenge to this system: when the received signal amplitude of circular co-polarization and cross-polarizations is equal, the system considers it as linearly polarized. Real-world measurements of a passenger car with a 79 GHz polarimetric radar with a bandwidth of 2.6 GHz (i.e., a range resolution of ~58 mm) have been performed. These show that co-polarization mainly covers signals with an even number of reflections, whereas cross-polarization mainly consists of signals with an odd number of reflections [36], as is in line with the theory stated in [16]. This allows to easily distinguish the vehicle from the environment and other unwanted detections, based on its co-polarized and cross-polarized signature, as has been verified with radar data from a real-world scenario of a parking car [37].

More measurements have been performed by Alaqeel et al., using a fully polarimetric radar with a relatively good angle resolution due to its operating frequency at 222 GHz. They found that the reflections of a vehicle are not originated from a strong scattering point, but due to contributions from all scattering points [38]. Furthermore, they analyzed the statistical behavior of radar return signals from vehicles. The measurements show that the Weibull distribution provides the best fit for the scattering strength of individual spots on the vehicle, with different parameter values for different

polarization combinations and different vehicle types [39]. It was again verified that the reflected signal varies significantly when changing the viewing angle, but they found that the statistics of the return signals from all scattering points of the vehicle is independent of this angle and only depends on the vehicle's physical and scattering properties [40].

So far, no paper investigating the use of the complete polarimetric information for classification purposes with automotive radar has been published yet. In 2017 Visentin et al. presented for the first time full polarimetric signatures of stationary two-wheeled vehicles, with 77 GHz automotive radar pointing towards several static objects rotating around their center in an anechoic chamber. Based on the polarimetric Pauli decomposition, color-coded images visualized the measurements containing much more information compared to the aforementioned approaches, since this decomposition considers the relative phase between the polarized components as well [41]. Each Pauli component is related to a physical interpretation, representing scatterers that reflect with an odd number (single) of bounces, with an even number (double) of bounces or as volume scatterer (i.e., cross-polarized scatterers) [8] (see Section 4.3.3). A similar approach is presented in [6], where a 3D-image showing the scattering points of a car based on the Pauli-components is reconstructed, which can be seen in Fig. 1.2. Although a clear way to distinguish the different targets from each other based on their polarimetric scattering signature is not presented, these results confirmed again the potential of target classification capability based on polarimetric measurements. This promising concept is further demonstrated and exploited with advanced classification algorithms based on a deep learning approach using a convolutional neural network (CNN) in [42]. It was shown that the accuracy of the classification algorithm using additional polarimetric information reached the same accuracy as a single polarized radar with an angle resolution three times better.

Motivated by this recent work, Tilly et al. researched polarimetric signatures of passenger cars using a 77 GHz automotive polarimetric radar as well. Real-world measurements from various aspect angles with respect to the vehicle show that polarimetric information makes it possible to identify car segments and can be used for estimating orientation and extent of the vehicles [44]. Very recently, this has been extended to a more dynamic scenario in an urban environment, where all detected object clusters were assigned to one of the four classes: vehicles (passenger cars), large vehicles (trucks, buses), two-wheeled vehicles (bicycles, motorbikes) and pedestrians. Based on a random forest classifier, a significant performance improvement has been shown by using the additional polarimetric features instead of only using single-polarization scattering information. An analysis on the permutation importance of the polarimetric features verifies that this information indeed contributes to determining the correct classes from some more complex cases [45].

Besides using additional polarimetric information for vehicle classification, this concept contributed to other automotive challenges as well, such as new approaches to separate objects with different polarimetric features in a multi-path environment (e.g., due to reflections on guardrails and on roads) [46], a more robust system for identification of guideposts and traffic signs by polari-

Figure 1.2: A reconstructed 3D-image of simulated X-band scattering data from Civilian Vehicle Domes (CVDOME) [43] of a Toyota Camry, applied with a Pauli basis color mapping, representing the physical interpretation of the Pauli components of all scattering points [6]

metric analysis [47] and new algorithms for sensing the environment around the vehicle for self-localization [48].

An overview of all mentioned authors can be found in Table 1.1. As can be seen, almost all research papers related to the polarimetric signature of automotive vehicles have been conducted with automotive polarimetric radars, operating with center frequencies in the W-band with a bandwidth in the order of GHz. All measurements of automotive targets performed in these experiments are of single, static targets that are relatively close to the radar (within 100 m), mostly in a known environment (i.e., an anechoic chamber, often similar as shown in Fig. 1.1).

Table 1.1: An overview of research papers related to the polarimetric signature of automotive vehicles

Author	**Related work(s)**	**Center frequency**	**Polarization**
Schipper et al.	[32]	25 GHz	Linear
Geary et al.	[33, 34]	25.5 GHz; 78.5 GHz	Linear (only co-polarized)
Trummer et al.	[35–37]	79 GHz	Circular
Alaqeel et al.	[38–40]	222 GHz	Linear
Visentin et al.	[41, 42, 46]	77 GHz	Linear
Tilly et al.	[44, 45]	77 GHz	Circular
Iqbal et al.	[47]	77 GHz	Linear
Weishaupt et al.	[48]	77 GHz	Circular

1.4. Research novelty

The goal of this research is to automatically extract polarization-based target features from a feature analysis of polarimetric-Doppler radar data while tracking moving targets, to identify polarimetric target features, and define sub-classes of automotive vehicles. In contrast with the studies described in the previous section, where mainly automotive radars were used, this thesis will use data from an S-band polarimetric surveillance radar operating at 3.3 GHz with a bandwidth of only 50 MHz. Therefore, the wavelength will be significantly larger, which will directly affect the scattering behavior of both the targets as the environment. Moreover, in our research, the vehicles will only be considered as a single point scatterer, or just a few range-Doppler bins, whereas the automotive radars show much higher performance in terms of range resolution, such that the vehicles are considered as extended targets. Besides, instead of analyzing measurements of a static vehicle in a known environment, this research work is based on a data set representing a dense environment with multiple targets that are moving with high velocity.

To track multiple targets in the range-Doppler domain, a classical Kalman filter with a data association algorithm based on the GNN method is implemented. Due to limitations of the FMCW Doppler processing, ambiguity in the Doppler domain can occur. In that case, the target's velocity measurement is not correct, resulting in an incorrect state prediction, and thus a decreased tracking performance. In order to mitigate this problem, a novel MHT-based approach is introduced. The likelihood ratio of two hypotheses, whether the Doppler frequency (i.e., folded velocity) of a new track is folded or not, is computed to determine the next predicted state in the consecutive range-Doppler frames. To improve the computational complexity of the MHT algorithm, it is assumed that Doppler folding can only occur once.

The feature extraction analysis on the polarimetric scattering of moving automotive vehicles did not lead to well-defined polarimetric features that can be useful for the classification of different sub-classes of these vehicles. Nevertheless, the polarimetric characteristics of the targets have been compared with the characteristics of static clutter. It has been found that polarimetric features,

originating from the $H/A/\alpha$-decomposition, are potentially very useful to classify observed targets either as moving vehicles or as static clutter. Therefore, with these features, even without velocity information, a classifier should be able to accurately distinguish moving vehicles from static clutter.

1.5. Thesis structure

In this report, the thesis will be structured as follows. This chapter introduces the research topic and includes the motivation and the goal of this thesis project. Furthermore, an overview of the state-of-the-art of polarimetric signatures of automotive vehicles is presented. The rest of the thesis is organized as follows. In Chapter 2 the fundamental basics of radar systems, radar polarimetry, and FMCW radar signal processing, which are important to understand the rest of the thesis, are summarized. The methodology of creating a target feature database while tracking all vehicles in a multi-target environment in the range-Doppler domain is presented in Chapter 3. Subsequently, Chapter 4 presents the feature extraction analysis approach and provides the results of this analysis based on the polarimetric signatures of moving automotive vehicles and static clutter. At last, the methodology and the results will be summarized and this research will be concluded in Chapter 5.

2

Radar Theory and Background

This chapter will cover basic radar theory and background information that is required to understand the content of the rest of this work. First, a brief overview of the radar fundamentals will be given, including the basic principles of a radar system and the concept of FMCW-radar. Secondly, the concept of radar polarimetry will be explained. At last, the radar used for this thesis will be introduced.

2.1. A brief overview of radar fundamentals

2.1.1. Basic principle of radar

Radar, standing for Radio Detection and Ranging RADAR, is a commonly used sensor that uses radio waves to detect the presence of objects and to find their positions. The principle of a radar system is based on a transmitted radio signal, which will be scattered by anything on its path and propagating back to a radio receiver, often placed near the transmitter. A basic radar system transmits pulses with a very high pulse power of a continuous signal with a certain radio frequency (RF), often referred to as the carrier frequency f_c, on and off. Once a short pulse of energy with duration τ_p is transmitted by an antenna, the system waits for the radio wave to travel away from the radar with the speed of light ($c \approx 3 \times 10^8$ m/s), is scattered from an object and is obtained by the receiver antenna again. The small part of the reflected signal that propagates in the direction of the radar is called the backscatter. The distance from the radar to the target, i.e., the range R, can then be calculated from the duration of the electromagnetic wave that has propagated back and forth to the object, as

$$R = \frac{c\tau_d}{2}, \tag{2.1}$$

where τ_d is the time delay of the signal. The rate at which pulses are transmitted is called the Pulse Repetition Frequency (PRF), usually in the order of kHz for long-range radar systems and MHz for short- and medium-range. Then, the time interval between the start of each pulse, also known as the Pulse Repetition Interval (PRI = 1/PRF), is often even smaller than 1 ms. This design parameter defines the maximum range of a target to be detected without any ambiguity: when a reflection of an object with a range larger than this maximum unambiguous range R_{max} is received by the radar, it is not possible to assign this echo to a single transmitted pulse. Therefore, it holds that

$$R_{max} = \frac{c \cdot \mathrm{PRI}}{2} = \frac{c}{2 \cdot \mathrm{PRF}} \tag{2.2}$$

This principle of a pulse radar is visualized in Fig. 2.1, where it can be seen that the second echo can be interpreted as a return from either the first pulse or the second pulse. This illustrates the relations described in the equations above. For example, a PRF of 1 kHz or 1 MHz results in a maximum unambiguous range R_{max} of 150 km and 150 m, respectively. Moreover, the ratio of the pulse length τ_p and the PRI is known as the the duty cycle $\delta = \tau_p/\text{PRI}$.

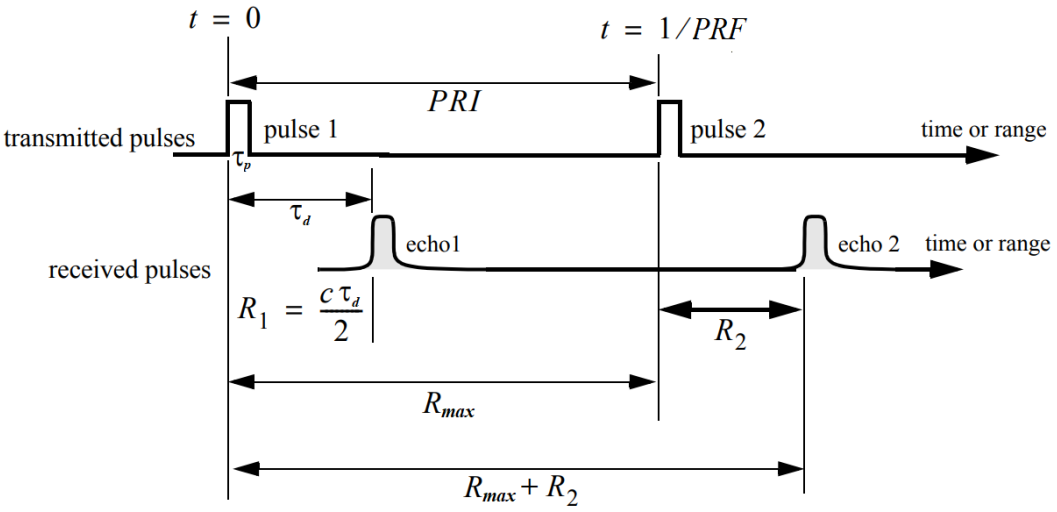

Figure 2.1: The working principle of a pulsed radar [49]

Besides measuring the range of a target, one can also be interested in estimating its velocity. There are two methods to measure the speed of a target:

1. Observation of the change in range of a certain target after N pulses can be used to easily derive its velocity. This method is used in *incoherent* radar systems, in which the receiver is not phase-locked and is therefore unaware of any small drifts in the frequency domain.

2. Make use of the so-called Doppler shift, which is the change in frequency of the radio signal caused by the motion of the target. Only *coherent* radar systems, in which the transmitter and receiver are phase-locked, can reveal these small differences in the echo frequency.

Although the first method is simple, it is not very accurate and therefore is often not considered in a radar system design. The Doppler effect occurs due to that each radio signal reflected by a target in motion has to travel a shorter/longer distance, resulting in a continuously changing phase over time. A distance change of λ m will change the echo phase by 2π. Therefore, if a target moves with a velocity of $\lambda/2$ m/s, the radar would detect a frequency change of 1 Hz. Hence, the Doppler shift f_D is given by

$$f_D = -\frac{2v_r}{\lambda} = -\frac{2v\cos\theta}{\lambda}, \tag{2.3}$$

where v_r is the radial component of the target velocity towards the radar, with θ being the aspect angle. Here it is assumed that $v_r \ll c$. As can be seen, the velocity component perpendicular to the radar view angle does not contribute to the Doppler shift, because the target is neither approaching nor receding from the radar. Note that the Doppler shift of a target moving perfectly along the radar view angle is zero [50]. Moreover, note that the convention is that a positive sign of the Doppler shift is defined so that the target is approaching the radar, thus a negative velocity, and vice versa.

Generally, the Doppler shift is estimated by analyzing the phase of the received signal for a fixed time, called the coherent integration time T_i. During this time N_{Sweeps} consecutive pulses are received, which are used to estimate the Doppler frequency shift f_D, computed by the complex Fast Fourier Transform (FFT). Note that the sampling frequency is thus equal to the PRF. According to the Nyquist sampling theorem, the maximum unambiguous Doppler shift f_D^{max} is ±PRF/2. Assuming that the radar itself is static, the maximum unambiguous velocity v_r^{max} is given by

$$v_r^{max} = \pm \frac{\lambda \cdot \text{PRF}}{4} \tag{2.4}$$

If the radial velocity is outside this interval, a phase change $\geq 2\pi$ will occur, and therefore, there is a Doppler ambiguity folding. When comparing Eq. (2.2) and Eq. (2.4), the PRF shows a trade-off between the maximum unambiguous range R_{max} and the maximum unambiguous velocity v_r^{max}. Modern radar systems make use of an adaptive PRF which changes continuously based on the target's behavior [51].

2.1.2. The radar equation

To be able to detect the presence of a target, the Signal-to-Noise Ratio (SNR) of the received signal should be sufficient. The SNR is expressed in terms of the *radar equation*, which depends on many parameters, such as the transmitter power P_t, the antenna gain of both the transmitter G_t and the receiver G_r, the wavelength λ, the reflected energy, the losses and the target range R. To start with, the total power received by the target is the transmitted peak power output P_t, amplified with gain G_t and divided by $4\pi R^2$, the area of a sphere of radius R through which all power must pass. The target only re-radiates a portion of this incident power. This ratio of intercepted power and power radiated back to the radar is called the Radar Cross Section (RCS), represented by the symbol σ with units of area. The RCS indicates how large the target appears to be as viewed by the radar. The reflected wave propagates back to the radar, attenuates again with factor $4\pi R^2$. This brings us to the following equation for the received power P_r,

$$P_r = \frac{P_t G_t \sigma A_e}{\left(4\pi R^2\right)^2}, \tag{2.5}$$

where A_e is the effective antenna area of the receiver. This parameter can be described by the antenna gain G_r and the wavelength λ

$$A_e = \frac{G_r \lambda^2}{4\pi}, \tag{2.6}$$

with the wavelength λ being inversely proportional to the center frequency f_c, given by

$$\lambda = \frac{c}{f_c} \tag{2.7}$$

Finally, losses and noise are inevitable, introduced by the system loss factor L_s, which is always between 0 and 1, and the average noise power N represents both internal noise coming from the electronics and external noise. Substitution of Eq. (2.5) and Eq. (2.7) brings us to the final equation for the SNR:

$$\text{SNR} = \frac{P_r}{N} = \frac{P_t G_t G_r \sigma \lambda^2 L_s}{(4\pi)^3 R^4 N} \tag{2.8}$$

As mentioned before, the SNR depends on many parameters related to the radar system design. One of the main parameters is the center frequency f_c, which directly is related to the wavelength, but also affects the antenna gain, the radar cross-section, the system losses, and other parameters. This center frequency can range from a few MHz to hundreds of GHz. The reason for this wide range is due to its trade-off between propagation losses over range, antenna size, the number of unwanted echoes, velocity resolution, and more performance metrics. The frequency spectrum is divided in RF frequency bands, of which each of them is assigned with a code letter, for security purposes during World War II, and nowadays still in use by radar engineers [50].

2.1.3. Performance metrics

To analyze 'how well' a radar can measure the range and velocity of a target, the performance metrics *resolution* and *accuracy* should be introduced. Here, the resolution is used to indicate the minimum difference that is needed to resolve two peaks, and the accuracy shows the uncertainty in a measurement. For range measurements, two closely-spaced targets can be resolved if the time delay between the two echoes from both objects is greater than the pulse duration τ_p. Hence, the shorter the pulse length, the better the range resolution ΔR. Also, the shorter the pulse, the higher the frequency of the sinusoids needed to reproduce its shape. Therefore, the pulse length can be approximated by $\tau_p \simeq 1/B$, where B is the bandwidth of the system. Converting this pulse duration into an analogous radar range measurement, the range resolution becomes

$$\Delta R = \frac{c\tau_p}{2} = \frac{c}{2B} \tag{2.9}$$

Often the radar is sampling each τ_p seconds, thus with sampling frequency B, so that each sample represents a distance ΔR, called a *range bin*. The accuracy of the range measurement δR is determined by the SNR of the received pulse and is given by

$$\delta R \simeq \frac{c}{2B\sqrt{2 \cdot \text{SNR}}} \tag{2.10}$$

To analyze the velocity resolution Δv_r, the time needed to resolve two Doppler frequencies separated by Δf_D needs to be considered. It is known from the Fourier analysis that this is the integration time T_i, which is the total time of N_{Sweeps} sweeps with pulse length τ_p. Given that $\Delta f_D \simeq 1/T_i$, the velocity resolution will be

$$\Delta v_r = \frac{\lambda}{2T_i} = \frac{\lambda}{2\tau_p N_{Sweeps}} \tag{2.11}$$

Similar to Eq. (2.10), the accuracy of the Doppler frequency estimation δf_D, and thus accuracy of the velocity measurement δv_r, depends on the SNR, given by

$$\delta v_r \simeq \frac{\lambda}{2\tau_p N_{Sweeps}\sqrt{2 \cdot \text{SNR}}} \tag{2.12}$$

Here the equations for the range accuracy δR and radial velocity accuracy δv_r are not exact, because it also depends on the shape of the pulse (known as the waveform), the effective bandwidth, and other radar system parameters [50]. A special type of waveform, driving the FMCW radar PARSAX, is the Linear Frequency Modulation (LFM) waveform, which will be examined in the next section.

2.1.4. FMCW radar

In contrast to the pulsed radar, a more advanced approach is to transmit a high-frequency signal continuously. This so-called Continuous-Wave (CW) radar has the ability to constantly measure the Doppler frequency by comparing the frequency of the transmitted signal and the received signal but is not capable of determining the range directly, since it is not possible to assign the received signals to a certain time delay. To resolve this problem, frequency modulation is introduced and is implemented in the Frequency-Modulated Continuous-Wave (FMCW) radar system.

An FMCW radar transmits a so-called *chirp signal*, also known as a *chirp*: a sinusoidal signal of which its frequency periodically changes over time. When this frequency is linearly increasing, it is referred to as an up-chirp, and when linearly decreasing, a down-chirp signal. This chirp signal is characterized by its center frequency f_c, bandwidth B and chirp duration time T_c (also known as the *sweep time*), as follows:

$$f(t) = f_c \pm \frac{B}{T_c} t, \tag{2.13}$$

where T_c between $[-T_c/2, T_c/2]$ and where the $\pm$ depends on having an up-chirp or down-chirp signal. As can be seen in Fig. 2.2, the received signal will be a delayed chirp signal with the same frequency-time slope and an additional Doppler frequency shit f_D. Whereas a pulsed radar must wait until the transmitted pulse is returned, an FMCW radar can continuously measure the target range by estimating the frequency difference between the transmitted and received signal at a certain time, known as the *beat frequency* f_b. This is achieved by mixing (multiplying) the transmitted and received signals and filtering the signal to get the lower frequency part. This beat frequency can be seen as a single peak in the intermediate frequency (IF) spectrum, of which its value is proportional to the delay between the transmitted and received waveform, and thus the target range, which is then given by

$$R = \frac{c\,|\Delta f|}{2\left(\frac{\partial f(t)}{\partial t}\right)} = \frac{c f_b T_c}{2B} \tag{2.14}$$

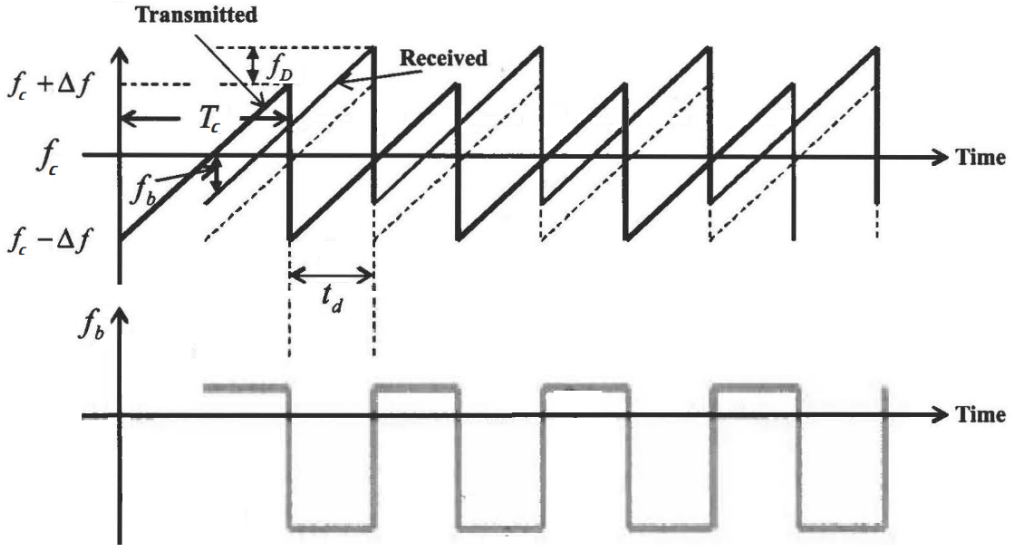

Figure 2.2: The frequency-time characteristics (top) and its corresponding beat frequency (bottom) of a linear sawtooth FMCW waveform, where Δf is equal to $B/2$ [52]

To obtain the beat frequency f_b, an FFT is applied. Therefore, the range resolution ΔR depends on the ability to resolve two peaks in the IF-spectrum. This again depends on the observation time of the signal, which is the chirp time T_c. Given that $\Delta f_b \simeq 1/T_c$ and following Eq. (2.14), the range resolution is similar as for the pulse radar, given by Eq. (2.9). Moreover, the maximum observable range depends here on the maximum beat frequency, which is, according to the Nyquist sampling theorem, half of the sampling frequency, and is thus limited by the ADC sampling rate [52].

Obviously, as Fig. 2.2 shows, the superimposed Doppler frequency f_D affects the value of the beat frequency f_b, and thus the target range measurement. Therefore, a target with a velocity causes an error in the range measurement, which is known as the range-Doppler coupling phenomenon. This can be compensated for by estimating the Doppler frequency over multiple chirps and subtracting it from the beat frequency.

An alternative solution is to use a linear triangular waveform, as shown in Fig. 2.3. The main property of this waveform is that it consists of both up-chirps and down-chirps. As can be seen, the absolute beat frequency f_b consists of two values, which are different when the target is non-stationary. The best estimation of the range is to extract the part caused by the Doppler shift and average the beat frequencies f_b^+ and f_b^- over an entire modulation cycle, assuming that range-related beat frequency is greater than its part caused by the Doppler shift. This waveform will be further exploited for polarimetric orthogonality, which will be explained in Section 2.2.

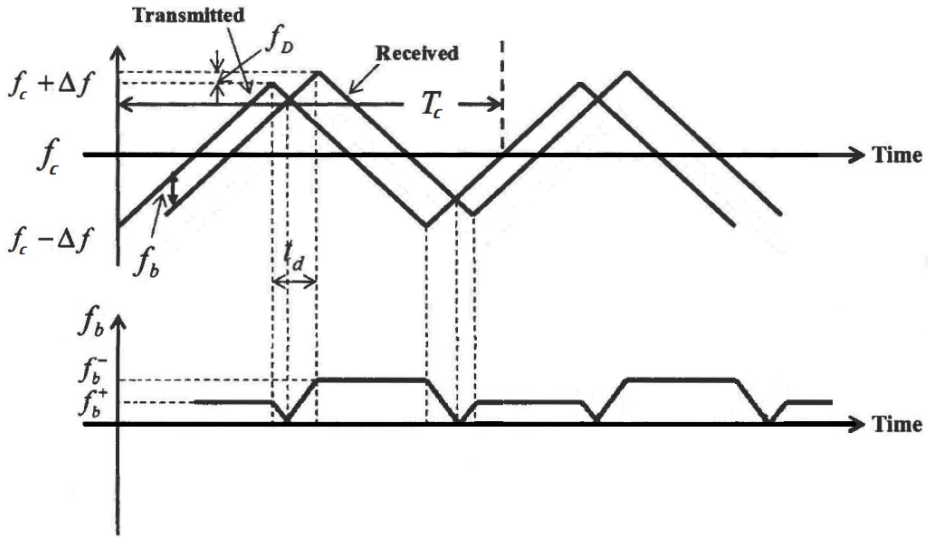

Figure 2.3: The frequency-time characteristics (top) and its corresponding beat frequency (bottom) of a linear triangular FMCW waveform, where Δf is equal to $B/2$ [52]

To estimate the velocity of the target, a similar approach as used in the classical pulsed radar is applied. Again the phase change between the pulses, referred to as the chirps, are exploited to estimate the Doppler shift. The time within each chirp is labeled as the *fast time*, and the time between the chirps is called the *slow time*. For each fast time an FFT is applied to compute the range, and subsequently a second FFT over N_{Sweeps} chirps (known as a *burst*) is performed to estimate the Doppler frequency. This 2D-FFT results into the range-Doppler spectrum, or range-velocity, of a single burst, as depicted in Fig. 2.4. Before this two-dimensional FFT, a window is applied to both the fast time and the slow time signals for sidelobe level and spectral leakage reduction. Optionally zero-padding can be applied to get a N_{FFT}-point FFT-operation for efficiency purposes and in order to improve the frequency resolution. Peaks in this range-Doppler spectrum represent targets at a certain range with a certain velocity [42]. Multiple *frames* of such a spectrum results in a three-dimensional data set of range-Doppler maps over time, also known as the *radar cube* [31].

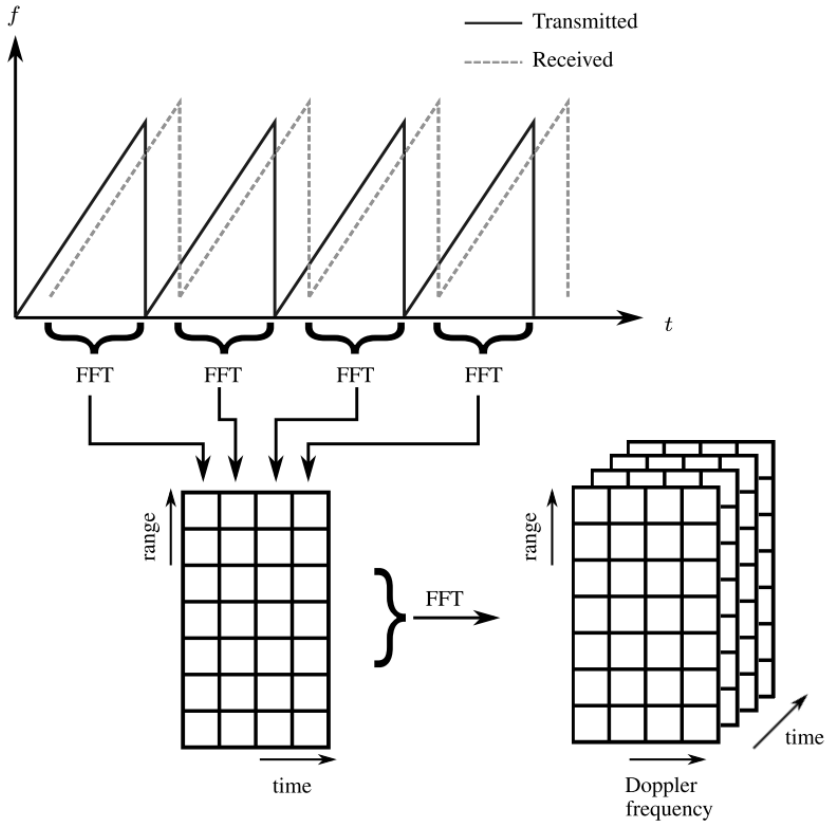

Figure 2.4: Signal processing chain to form the radar cube, a three-dimensional data set of the range-Doppler spectra over time as a result from a 2D-FFT operation [42]

2.2. Basic concept of radar polarimetry

To understand the working principle of a fully polarimetric radar and to analyze the polarimetric radar data, it is useful to gain knowledge of the basic concept of radar polarimetry. The fundamentals of electromagnetic waves, the polarization state, the polarization scattering matrix, and the mathematical background of a polarimetric radar will be introduced.

2.2.1. Plane waves and polarization

An electromagnetic wave is composed of, as its name already suggests, oscillating electric and magnetic fields. An electromagnetic wave has a propagation direction indicated by $\vec{k}$, an electrical field vector $\vec{E}$ and a magnetic field vector $\vec{H}$, all perpendicular to each other. This is illustrated in Fig. 2.5a. The wave polarization is defined as the oscillation direction of the electrical field $\vec{E}$, which can be decomposed into vertically and horizontally polarized parts. Hence, the plane wave can be described as a two-dimensional vector consisting of the two complex components $\vec{E}_x$ and $\vec{E}_y$:

$$\vec{E} = \begin{bmatrix} E_x(t) \\ E_y(t) \end{bmatrix} = \begin{bmatrix} E_x^0 e^{j(\omega t - k_0 z_0 + \phi_x)} \\ E_y^0 e^{j(\omega t - k_0 z_0 + \phi_y)} \end{bmatrix}, \tag{2.15}$$

where E_x^0 and E_y^0 are the field component amplitudes in respectively horizontal and vertical direction, ω is the angular frequency equivalent to $2\pi f$ with f the wave frequency, k_0 describes the wave number in free space from observation plane $z = z_0$ and ϕ_x, ϕ_y are the corresponding phase delays for horizontal and vertical polarization direction [16, 42]. As can be seen, only the amplitude and

phase depend on the wave polarization. Therefore, the polarization state of the electromagnetic wave can be denoted by

$$\vec{E} = \begin{bmatrix} E_x^0 e^{j\phi_x} \\ E_y^0 e^{j\phi_y} \end{bmatrix}, \tag{2.16}$$

where for convenience the exponential propagation vector $\exp\left(j\left(\omega t - k_0 z_0\right)\right)$ is dropped. This attenuation factor is equal for both elements and is therefore not required to describe the wave polarization. This notation is known as the Jones vector [16], as is illustrated as in Fig. 2.5b. The polarization state can be described in the form of an ellipse, of which its ellipticity angles are defined by the amplitudes E_H^0, E_V^0 and their corresponding phases ϕ_H, ϕ_V, where the subscripts H and V replace x and y, and refer to horizontal and vertical polarization, respectively. In the case of linear polarization, the polarization state can be described by a vector along the x- or y-axis, whereas for circular polarization, its state vector follows an ellipsoid form over time [19].

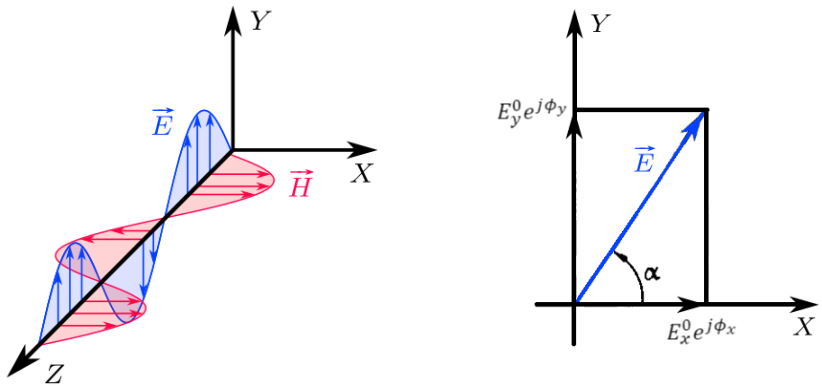

Figure 2.5: Illustration of an electromagnetic plane wave: (a) in three-dimensional space, propagating in the z-direction and polarized in the y-direction [42] and (b) in fixed plane with polarization angle α and corresponding phases $\phi_{x,y}$, equivalent to $\phi_{H,V}$ [19]

2.2.2. Polarization Scattering Matrix

When an electromagnetic wave is reflected from a target, its polarization state will likely be different from that of the incident wave. The Polarization Scattering Matrix (PSM), denoted by **S**, describes the change of the polarization state and represents the scattering characteristics of the target. For linear polarized waves, the relationship between the incident electric field $\vec{E}_i$ and the reflected electric field $\vec{E}_r$, is described by

$$\vec{E}_r = \mathbf{S} \cdot \vec{E}_i, \tag{2.17}$$

where each element of **S** is a complex number. Here **S** is independent of the polarisation state of the incident wave but depends on the frequency and geometrical and electrical properties of the scatterer [8]. The PSM is then given by the complex 2-by-2-matrix

$$\mathbf{S} = \begin{bmatrix} S_{HH} & S_{VH} \\ S_{HV} & S_{VV} \end{bmatrix}, \tag{2.18}$$

with $S_{HV} = S_{VH}$ for the reciprocal monostatic case [16, 53]. The first and second subscript H, V refers to the horizontal and vertical polarization of the transmitted signal and received signal, respectively. The total scattered power P_s can then be described by the span of **S**:

$$P_s = |S_{HH}|^2 + 2|S_{HV}|^2 + |S_{VV}|^2, \tag{2.19}$$

where again the monostatic case is assumed. The basis of this S-matrix can be converted by using unitary matrix transformations, for example, to transform linear polarization into circular polarization. For circular polarization waves, where the horizontal and vertical polarized components are 90° out of phase, the relation with linear polarization is given by

$$\begin{bmatrix} E_H \\ E_V \end{bmatrix} = \frac{1}{\sqrt{2}} \begin{bmatrix} 1 & 1 \\ j & -j \end{bmatrix} \begin{bmatrix} E_R \\ E_L \end{bmatrix}, \tag{2.20}$$

which will expressed by the circular polarized S-matrix as follows:

$$\mathbf{S} = \begin{bmatrix} S_{RR} & S_{RL} \\ S_{LR} & S_{LL} \end{bmatrix}, \tag{2.21}$$

where the subscripts R and L represent right-handed circular (RHC) and left-handed circular (LHC) polarization, respectively [54].

2.2.3. Polarimetric radar

The concept of a fully polarimetric radar is that it can measure all four elements of the S-matrix, so it can provide more information about the scattering properties of the target as single polarized radars, which can be beneficial for classification purposes. In order to be able to measure the full S-matrix simultaneously, the radar has to meet two requirements. Firstly, the transmitter side needs to be able to transmit both vertically and horizontally polarized waves orthogonally. Secondly, the receiver side must be orthogonally polarized as well and needs to be able to receive the orthogonal signals simultaneously. The transmitter and receiver channels need to be isolated as well as possible [42]. The relation between the transmitted and received signal can then be simply be written as a linear operator as follows,

$$\vec{E}_{RX}(t-\tau_d) = \mathbf{S}(t,\tau_d) \cdot \vec{E}_{TX}(t), \tag{2.22}$$

where τ_d is the time delay between the transmitted and received signal. This vector representation becomes in matrix form

$$\begin{bmatrix} E_H^{RX}(t-\tau_d) \\ E_V^{RX}(t-\tau_d) \end{bmatrix} = \begin{bmatrix} S_{HH}(t,\tau_d) & S_{VH}(t,\tau_d) \\ S_{HV}(t,\tau_d) & S_{VV}(t,\tau_d) \end{bmatrix} \begin{bmatrix} E_H^{TX}(t) \\ E_V^{TX}(t) \end{bmatrix}, \tag{2.23}$$

where, as can be seen, only two signals, E_H^{RX} and E_V^{RX}, are received. In order to separate each signal into a part originating from E_H^{TX} and a part coming from E_V^{TX}, orthogonality in time-domain or in frequency-domain needs to be exploited. Further elaboration on this can be found in [55]. After the signal processing steps as introduced in the previous section (two-dimensional FFT, MTI, etc.) four range-Doppler spectra, corresponding to each element of the S-matrix, can be computed. Each bin of this spectrum can then be described by Eq. (2.18) as

$$\mathbf{S} = \begin{bmatrix} S_{HH}(\tau_d, f_d) & S_{VH}(\tau_d, f_d) \\ S_{HV}(\tau_d, f_d) & S_{VV}(\tau_d, f_d) \end{bmatrix}, \tag{2.24}$$

where the time delay τ_d is proportional to the range and Doppler frequency f_d represents the velocity [56]. Again, considering a monostatic case, the cross-polarized elements S_{VH} and S_{HV} are equal.

2.3. Signal processing using PARSAX radar data

In this section, an introduction to the fully polarimetric radar PARSAX, developed by the TU Delft, is given and its radar characteristics are presented. Subsequently, the basic radar signal processing chain is visualized with data captured by PARSAX.

2.3.1. Fully polarimetric radar PARSAX

The PARSAX radar is an S-band high-resolution FMCW radar and is generally used as long-range surveillance or weather radar (see Fig. 2.6). A unique feature of this radar is its ability to transmit and receive horizontally and vertically polarized electromagnetic waves in parallel. Therefore, all four complex elements of the scattering matrix can be measured *simultaneously*, to describe the amplitude, phase, and polarization state of each range-Doppler bin. The ability to utilize sounding signals with orthogonally-polarized components is a strong advantage compared to many other existing polarimetric radar systems, which measure the elements of the polarization scattering matrix by switching the transmitter and/or receiver polarization mode from pulse-to-pulse. This causes a temporal measurement mismatch, which is not desirable when using polarization information for target detection and classification algorithms [7, 57].

A critical point for polarimetric radar is the orthogonality of the sounding signals, which strongly affects the isolation between the polarimetric radar channels. Bad polarimetric isolation limits the system's ability to observe weak targets in an environment with other strong targets and clutter. A novel method for quasi-simultaneous measurement of the PSM is developed for the PARSAX radar [58]. Based on the work of Babur et al. [59], a pair of LFM-signals with a positive slope (see Fig. 2.2) are time-shifted from each other to allow occupation of different frequency bands continuously. Due to this relative time delay, corresponding to a frequency shift, orthogonality can be considered and a high polarimetric isolation level can be achieved. Here the first signal is transmitted with horizontal polarization, whereas the shifted LFM-signal is vertically polarized. The FMCW de-ramping technique provides the possibility to mix each received signal with both transmitted signals, resulting in beat frequency spectra (using FFT), corresponding to all range bins and all scattering matrix elements. Unfortunately, this technique has some limitations. The time delay between the two LFM-signals is required to achieve orthogonality but also leads to quasi-simultaneity of the measurements. Moreover, this time shift introduces a limitation for the maximum unambiguous range, which will be discussed further in the next section. Despite these limitations, these sounding signals with dual-orthogonal continuous waveforms are able to provide high-level isolation between the polarimetric channels, independent of the observed radar target [58]. A detailed block diagram illustrating the system of the PARSAX radar can be found in Appendix A.1 [55].

Figure 2.6: The PARSAX radar on top of the EEMCS faculty of the TU Delft

2.3.2. PARSAX characteristics

This fully polarimetric radar operates at 3.315 GHz with a maximum bandwidth of 50 MHz. A single sweep, consisting of both the up-chirp and the down-chirp part, has a duration of 1 ms, which is sampled with 400 MHz with 14-bit resolution. The FPGA-based digital processing makes it possible to use different classes of waveforms and to implement complicated algorithms for signal and data processing purposes in real-time with low noise, clutter, external and cross-channel interference characteristics [55]. An overview of the main characteristics of the PARSAX radar can be found in Table 2.1.

Table 2.1: Main characteristics of the PARSAX radar [55]

Category	**Parameter**	**Value**	
System characteristics	Center frequency (f_c)	3.315 GHz (S-band)	
	Modulation bandwidth (B)	2 MHz to 50 MHz	
	Range Resolution (ΔR)	3 m to 75 m	
	Sweep time (T_c)	1 ms	
Antenna characteristics		TX	RX
	Number of antennas	1	1
	Antenna diameter	4.28 m	2.12 m
	Antenna beamwidth	1.8°	4.6°
	Antenna gain	40.0 dB	32.8 dB
	RX-TX isolation (HH-polarized)	−100 dB	
	RX-TX isolation (VV-polarized)	−85 dB	
	Antenna type	Parabolic reflectors	
Power characteristics	Max. power per channel	100 W	
	Transmitter attenuation	80 dB	
ADC characteristics	Max. sampling frequency	400 MHz	
	ADC resolution	14-bit	
	Spur-free Dynamic Range (SFDR)	≥70 dB	

From these characteristics, a number of limitations and performance metrics from Section 2.1 can be derived already:

- R_{max} - Given that the PRI is equal to the sweep time T_c, according to Eq. (2.2) the maximum unambiguous range R_{max} is approximately 153 km, which easily meets the requirements.

- v_r^{max} - From Eq. (2.4) it can be seen that the maximum radial velocity v_r^{max} is ±22.1 m/s, equivalent to ±79.8 km/h.

- ΔR - To derive the range resolution, the bandwidth needs to be examined. Since only 90% of the total sweep time data is acquired, the maximum effective bandwidth B_{eff} is 45 MHz. This results in a range resolution ΔR of 3.3 m.

- Δv_r - To derive the velocity resolution, the number of sweeps per burst N_{Sweeps} needs to be determined. Usually, the FFT of 512 sequential profiles is computed [7], equivalent to an integration time T_i of approx. 0.52 s. Following Eq. (2.11) this results in a velocity resolution Δv_r of 0.087 m/s, or 0.31 km/h.

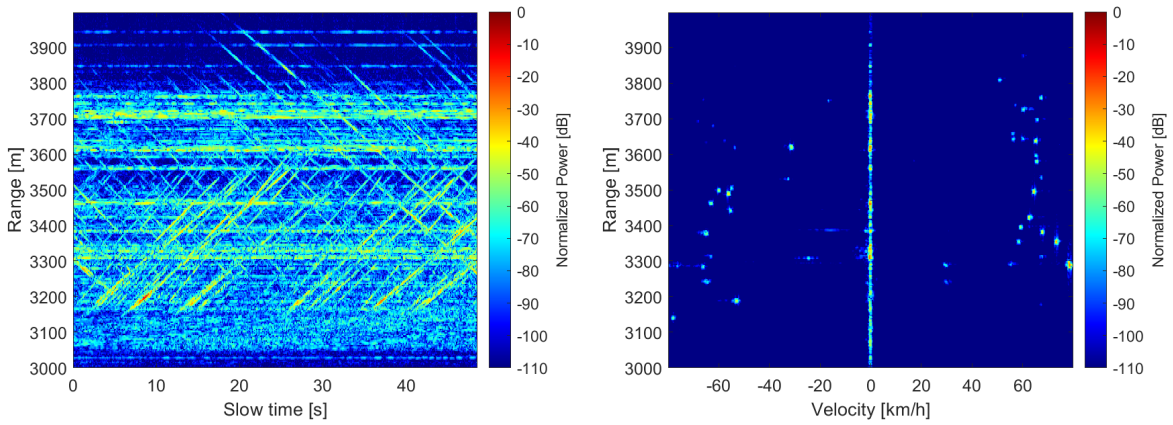

(a) (b)

Figure 2.7: (a) A normalized range-time plot and (b) a normalized range-Doppler spectrum of the HH-polarized data set generated by the PARSAX radar pointed towards a dense highway

These parameters will be of great importance for target detection and target tracking, which will be discussed in both Section 3.1 and Section 3.4. Especially due to the choice of PRF the maximum unambiguous radial velocity v_r^{max} can be a critical factor for the tracking performance since it is relatively low with respect to a realistic target's true velocity. The maximum unambiguous range R_{max} will not be considered as a limitation for our application of interest.

2.3.3. Two-dimensional Fourier Transform

As described in Section 2.1.4, a two-dimensional FFT needs to be performed to get a range-Doppler map of a burst of N_{Sweeps} pulses. Radar data is captured by the PARSAX radar while pointing towards a highway (i.e., the A13 highway between Rotterdam and Delft). The raw, complex data is pre-processed first, where the first FFT is performed to get the return amplitude at each range bin, given by the *fast time* delay, over *slow time*. Only the range bins describing the area of interest (from 3330 m to 4330 m) have been considered. In Fig. 2.7a the normalized power of the HH-polarized, complex range-time data is presented. The clearly visible diagonal lines represent the reflections of the vehicles moving away from the radar (with increasing range) and approaching the radar (with decreasing range). The other reflections are coming from noise and unwanted echoes from other objects, known as *clutter*. Many of these objects are static and are represented by straight, horizontal lines, indicating that the range is fixed over time.

Subsequently, a 2$^{\text{nd}}$ FFT will be performed to get the range-Doppler spectrum of a single burst. Beforehand, an 80 dB-Chebyshev window function is applied to the data in order to reduce the sidelobe levels and spectral leakage [56], such that the sidelobe level is constant [3]. Given that the total time of the captured data is approx. 17 s and that each frame contains 512 pulses, this data set can be split into 93 frames. The normalized range-Doppler spectrum of the first frame is shown in Fig. 2.7b. As can be seen, the moving vehicles are indicated by peaks at a certain range and a certain velocity, which can either be negative (approaching the radar) or positive (receding from the radar). The static clutter can clearly be seen around 0 km/h.

The range-time and range-Doppler plots of the other polarization elements (i.e., HV-polarized, VH-polarized and VV-polarized) can be found in Appendix A.2 and A.3, respectively. The values are normalized to the maximum value of all four data sets. Although the plots of all four polarization elements are similar, the power values of the cross-polarized elements are significantly smaller than the power values of the co-polarized elements.

2.3.4. Moving Target Indicator

As described in the previous section, the static clutter is represented by strong reflections around 0 km/h. Since we are only interested in targets with high velocity, and thus with high Doppler frequency, clutter can be filtered out by a high-pass filter (HPF). From prior knowledge of the area of interest, it is assumed that the targets are not moving orthogonal to the radar view angle, i.e., the aspect angle θ from Eq. (2.3) is not approaching 90°, so that radial velocity of the observed targets is near 0 km/h as well. The most common technique is the Moving Target Indicator (MTI), where each echo from a given range bin is subtracted coherently from a delayed version of the previous echo in order to inspect the phase change, which is related to the velocity. Therefore, this so-called *delay line canceling MTI* acts as an HPF for slow targets [50]. This is illustrated in Fig. 2.8. To maintain the signals of the targets with low velocity, an improved HPF with a steeper slope is chosen to be used: a 6^{th}-order Butterworth-filter is implemented, because its frequency response is maximally flat in the passband [60], with its cut-off frequency at 122 Hz, equivalent to 20 km/h.

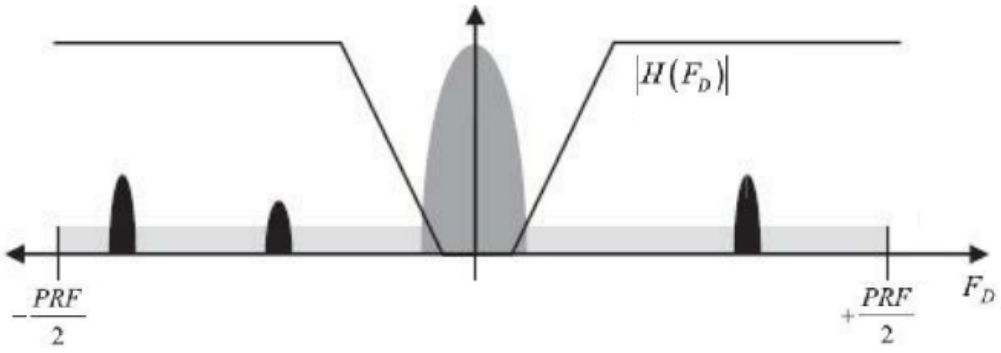

Figure 2.8: The principle of the MTI, acting as a HPF and filtering out static clutter [3]

This filter has been applied to the HH-polarized, complex data set shown in Fig. 2.7. As can be seen in the range-time plot of the filtered data in Fig. 2.9a, the horizontal lines representing the static clutter are attenuated significantly. Moreover, the vertical line around 0 km/h in the range-Doppler spectrum has completely disappeared, as shown in Fig. 2.9b. The range-time and range-Doppler plots of the other polarization elements can be found in Appendix A.4 and A.5, respectively. Again, the values are normalized to the maximum value of all four data sets.

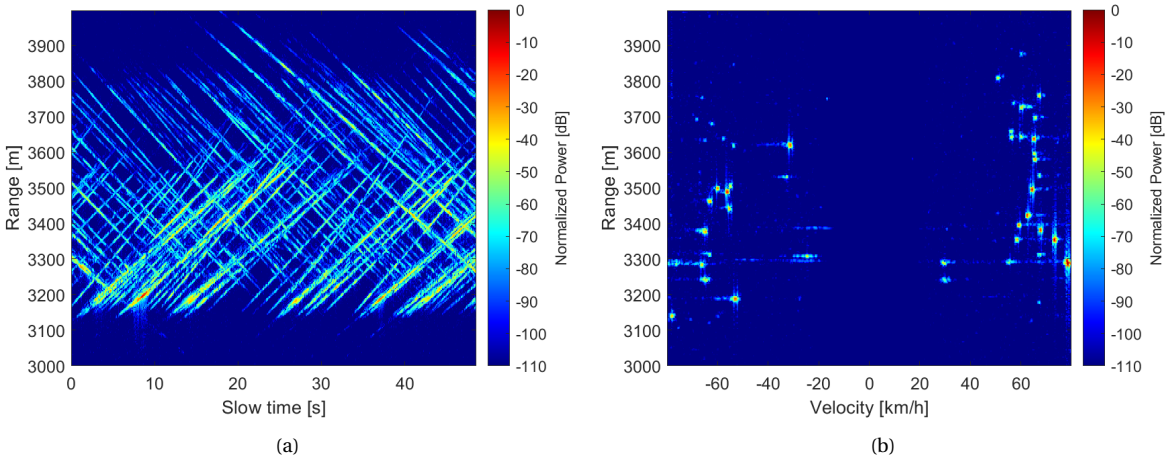

Figure 2.9: (a) A normalized range-time plot and (b) a normalized range-Doppler spectrum of the HH-polarized data set generated by the PARSAX radar pointed towards a dense highway, after a HPF has been applied

2.4. Conclusion

In this chapter the theory and background to understand the basics of radar systems and radar signal processing has been provided. It has been explained that the concept of radar is exploited to estimate the range of an object of interest, known as a target, through the time delay between the transmitted and received RF signal. In addition to that, the target's radial velocity can be estimated by exploiting the frequency shift between the transmitted and received signal, known as the Doppler shift. Generally, this Doppler shift is computed by a complex FFT over N_{Sweeps} consecutive pulses. The maximum of both range and velocity estimation is limited by the PRF, which introduces a trade-off for selecting the PRF. Moreover, the radar equation has been introduced and has led us to an equation for the received signal's SNR. Furthermore, performance metrics like the resolution and accuracy of the range and velocity estimation have been discussed. It has been shown that the range resolution is directly related to the system's bandwidth and that the velocity resolution is dependent on the signal's wavelength, the pulse duration, and N_{Sweeps}. Subsequently, the basic principle of an FMCW radar system has been introduced and both the linear sawtooth and the linear triangular LFM waveforms are presented. This waveform requires a two-dimensional FFT to estimate the target's range and velocity over time, leading into a three-dimensional data set of range-Doppler maps over time, known as the radar cube.

The basic concept of radar polarimetry has been discussed as well. An electromagnetic plane wave is mathematically described as a vector of two complex components, related to an electric field vector and a magnetic field vector. Each component has a certain amplitude, frequency, and phase delay and is perpendicular to each other, corresponding to horizontal polarization and vertical polarization. The polarization state is derived to describe the scattering characteristics of a target by the PSM. This complex 2-by-2 matrix represents the relationship between the incident electric field and the reflected electric field and is given for both linear polarized and circularly polarized waves. This concept is also used to describe the relationship between the transmitted and received signal of a polarimetric radar, which is able to measure all four elements of the PSM simultaneously.

With these fundamentals, the radar signal processing chain has been applied to radar data originating from the PARSAX radar, a fully polarimetric FMCW radar operating at 3.315 GHz. The main characteristics are presented, and its limitations and performance metrics are derived from these. A critical limitation is its maximum radial velocity ($\pm$79.8 km/h), which with our field of interest will result in many targets with folded velocity. The captured complex radar data, representing the reflections from a highway, is pre-processed, a 2D-FFT is performed, and the data is presented in both range-time and range-Doppler domain for all four polarization elements. After applying a high-pass filter, an improved Moving Target Indicator, the static clutter, represented by a strong reflection around 0 km/h, has completely disappeared and only targets remain visible in both range-time and range-Doppler domain.

3

Method for Feature Database Creation

In the previous chapter, it can be seen how the raw data is processed to a three-dimensional radar data cube, consisting of range-Doppler spectrum frames over time. To create a feature database of the vehicles that can be observed in these range-Doppler frames, one must be able to track the vehicles, and therefore each target must be detected first. In this chapter, the fundamentals of detection theory will be explained and the used detection method will be introduced. Since the PARSAX radar provides full polarimetric information, several methods for polarimetric fusion will be explained. Subsequently, the detections will be clustered and filtered so that each cluster represents a single target. Following upon, a multi-target tracking problem will be introduced and discussed. Finally, the creation and the content of the feature database will be presented.

3.1. Target detection algorithm

The first step in this data processing chain is to detect the vehicle in the range-Doppler domain. Before comparing the different methods for detection, the fundamentals of detection theory will be presented. Finally, the outcome of this detection algorithm is a binary detection map for each polarized data set.

3.1.1. Basic detection theory

Detection theory concerns the distinguishing of one or more target signals from noisy measurement signals or interference signals. Therefore, detection means making a decision for each range-Doppler bin whether a target is present or not. Hence, for each complex radar measurement sample, two hypotheses can be true: hypothesis $\mathscr{H}_0$ meaning that no target is present and noise or interference is measured, and hypothesis $\mathscr{H}_1$ means that a target is present at the range-Doppler coordinates of that measurement. Often this decision is based on a threshold with respect to the amplitude/power measurement of the range-Doppler bin. Under the so-called *Neyman-Pearson criterion*, the goal of the decision process is to determine a threshold that maximizes the probability of detection P_D for a fixed acceptable probability of false alarm P_{FA} [50]. Since a radar often makes thousands, sometimes even millions of measurements per second, a commonly used value for P_{FA} is in the range of 10^{-4} to 10^{-9}. Moreover, for any threshold, there will be a situation that a target is present, but not detected. This is denoted by the probability of missed detections P_M, equal to $1-P_D$.

Because the signals can be described statistically, one is interested in the probability density function (PDF) of a measurement y under each of the two hypothesis, denoted by $p(y|\mathscr{H}_0)$ and $p(y|\mathscr{H}_1)$.

To determine an optimal threshold γ following the Neyman-Pearson decision rule, the *likelihood ratio test* (LRT) $\Lambda(y)$ will be introduced: the ratio between the probability that a target is present, given by hypothesis $\mathscr{H}_1$, or that a target is not present, given by $\mathscr{H}_0$:

$$\Lambda(y) = \frac{p(y|\mathscr{H}_1)}{p(y|\mathscr{H}_0)} \underset{\mathscr{H}_0}{\overset{\mathscr{H}_1}{\gtrless}} \gamma \tag{3.1}$$

As can be seen, this likelihood ratio defines the probability of whether a measurement exceeds a certain threshold. In case that the natural logarithm is taken on both sides, to simplify computations, the obtained ratio is referred to as the *log-likelihood ratio test*.

For example, in case of detection of the presence of a target with constant amplitude A in zero-mean Gaussian noise with variance σ_n^2, a single measurement y could either represent hypothesis $\mathscr{H}_0$ ($y = n$) or hypothesis $\mathscr{H}_1$ ($y = A+n$), where n is a noisy measurement. Both hypothesis distributions can then be described as

$$\begin{cases} \mathscr{H}_0 : \ y \sim \mathscr{N}(0, \sigma_n^2) \\ \mathscr{H}_1 : \ y \sim \mathscr{N}(A, \sigma_n^2) \end{cases} \tag{3.2}$$

The PDF of each hypothesis $p(y|\mathscr{H}_i)$ can then be expressed as,

$$\begin{cases} p(y|\mathscr{H}_0) = \frac{1}{\sqrt{2\pi\sigma_n^2}} \exp\left(-\frac{1}{2}\frac{y^2}{\sigma_n^2}\right) \\ p(y|\mathscr{H}_1) = \frac{1}{\sqrt{2\pi\sigma_n^2}} \exp\left(-\frac{1}{2}\frac{(y-A)^2}{\sigma_n^2}\right) \end{cases} \tag{3.3}$$

which can directly be used to derive the likelihood ratio $\Lambda(y)$ and the log-likelihood ratio $\ln\Lambda(y)$, following Eq. (3.1). This carries all the information needed to determine the threshold γ for the desired false alarm probability P_{FA}. The threshold should be chosen such that the integral of the Gaussian PDF of $\mathscr{H}_0$ from the threshold value to $+\infty$ is equal to P_{FA}. Therefore, the threshold strongly depends on the mean and variance of the PDFs of the hypothesis. This is illustrated in Fig. 3.1a. As can be seen, a higher SNR, meaning a higher mean value of $p(y|\mathscr{H}_1)$, results in improved detection performance. Moreover, increasing the threshold leads to a smaller P_{FA}. However, it also decreases the probability of detection P_D. Hence, there is always a trade-off between improving detections and reducing false alarms. In this example, the probability of detection is related to P_{FA} and the SNR according to

$$P_D = P_{FA}^{\frac{1}{1+\mathrm{SNR}}}, \tag{3.4}$$

which shows that P_D approximates 1 when the SNR is increasing. Note that this relation is only valid for a single sample detection for a particular target model.

The performance of a detector is indicated by these probabilities and is often assessed by its Receiver Operating Characteristic (ROC) curve. This curve is related to the variables P_D, P_{FA}, σ_n^2 and the SNR. Here P_D is a result of the often fixed P_{FA} and the latter two, which are characteristics of the given signals [3]. The ROC curve is plotted for several SNR-values in Fig. 3.1b.

3.1.2. Non-adaptive detector

The most simple approach to determine whether a target is present or not is to set a threshold that is fixed for all range-Doppler bins. The magnitude of each sample of the received signal is analyzed and compared to this threshold. If it is above this threshold, it is assumed that the high amplitude is due to the presence of a target, and vice versa. Often this threshold level is an outcome of a statistical

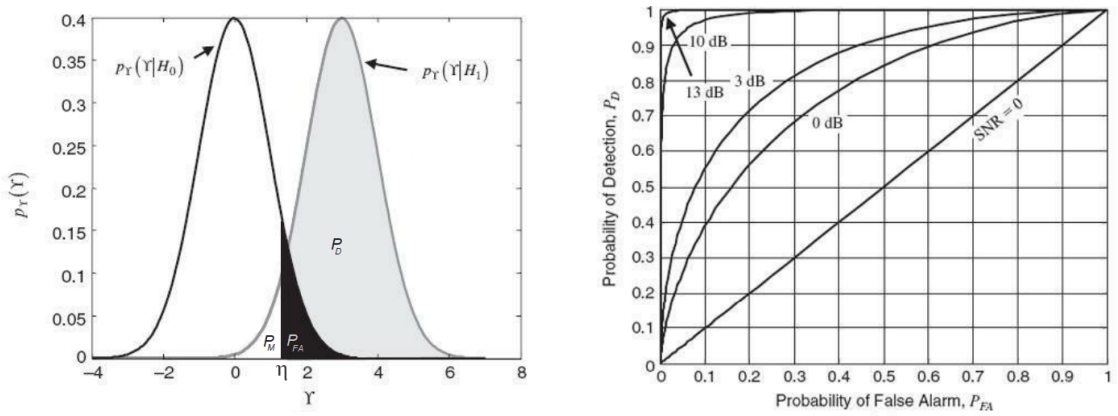

(a) (b)

Figure 3.1: An illustration of a simple detection scenario, (a) indicating the probability of false alarm P_{FA}, probability of detection P_D and probability of missed detections P_M for a fixed threshold η and a known PDF of the noise, and (b) the relation between P_D and P_{FA} for a given SNR, known as the ROC curve [3]

process and is therefore not perfect. For example, the threshold level could be exceeded by a noisy spike, resulting in a false alarm. As has been shown before, a higher SNR will lead to a smaller P_{FA}. However, since interference signals can also exceed the threshold and lead to a false alarm, not the SNR but the Signal-to-Interference-plus-Noise Ratio (SINR) should be taken into account [3]. Again, the threshold can be set for a fixed P_{FA}, when the distribution of the noise and clutter is prior knowledge. From this PDF, the threshold can be defined by the area of P_{FA}, illustrated by Fig. 3.1a. This can be translated into a threshold based on the mean noise power, plus a certain margin that depends on the P_{FA} again [50].

For this reason, all data captured by the PARSAX radar includes a noise-only data set. This is measured by disabling the transmitter, separately from the regular measurements, so that no reflections are present and the receiver only measures thermal noise and system noise. Since we are only interested in moving targets, static clutter will be filtered out (see Section 2.3.4) and can be ignored for now. Note that moving clutter cannot be filtered out and is therefore not included in this distribution estimation. The PDF of the noise can be estimated by analyzing the histogram of both the real and imaginary part of each complex noise data sample for each polarization. As can be seen from Fig. 3.2, the real and imaginary parts show both a zero-mean normal distribution, which characterizes complex white Gaussian noise. Moreover, the absolute value of the complex amplitude follows a Rayleigh distribution, and the noise power (i.e., amplitude squared) is exponentially distributed, which again verifies that complex, white Gaussian noise can be considered. The noise statistics shown in this figure are only of HH-polarization. Nevertheless, the statistics in other polarization states are similar (see Appendix A.6).

3.1.3. Constant False Alarm Rate (CFAR) detector

A non-adaptive fixed threshold is only feasible when the noise and interference level is known and is identically distributed in each detection cell. In practice, this is not the case. A commonly used adaptive detection method is the *Constant False Alarm Rate* (CFAR) detector, designed to get an improved prediction of the detection and false alarm rate in more practical scenarios. Instead of estimating the mean noise power from the noise-only data, CFAR dynamically computes the local noise level of each *cell under test* (i.e., each range-Doppler bin) by finding the mean of some *reference test cells*, which are close to the cell under test. The test cells that are too close to the cell under test and are contaminated by the presence of the target are often not included in the mean and are

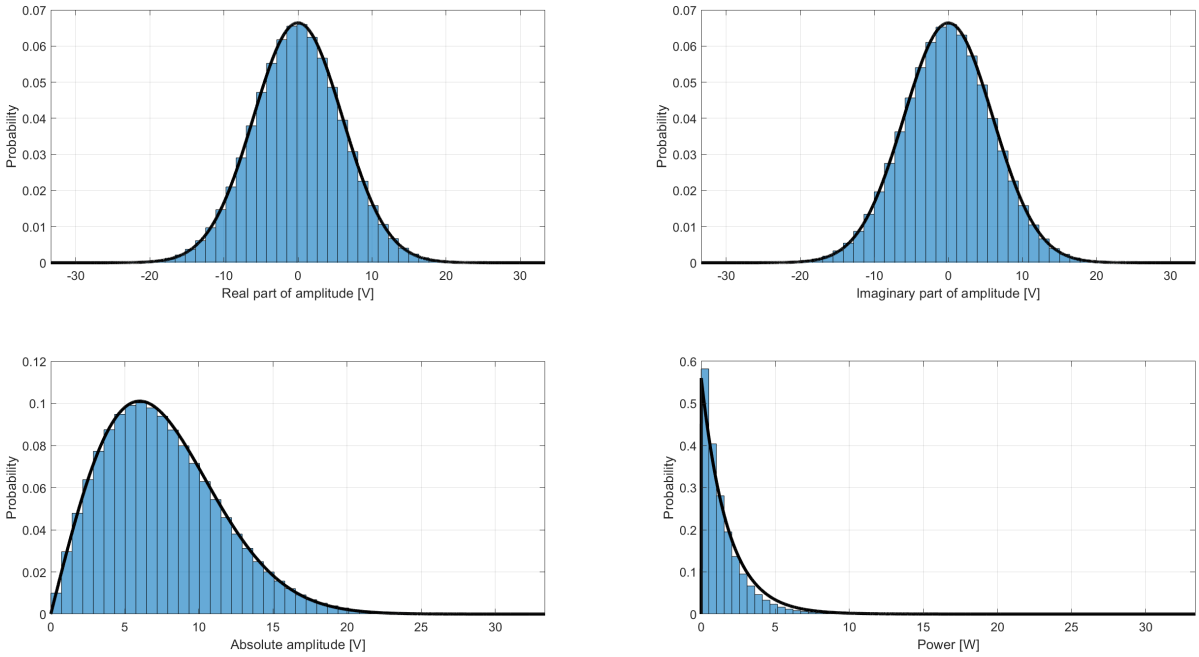

Figure 3.2: The noise statistics of zero-mean complex Gaussian noise captured by the PARSAX radar

referred to as the *guard cells*. The cell under test, reference test cells, and guard cells combined are referred to as the *CFAR window*, which is depicted in Fig. 3.3. The number of test cells N_t and the number of guard cells N_g depends on the target size and the background variation and must be optimized for each radar application. The threshold is again defined by the mean noise power, plus a margin based on maintaining a constant P_{FA}, as the name of this technique already suggests [50].

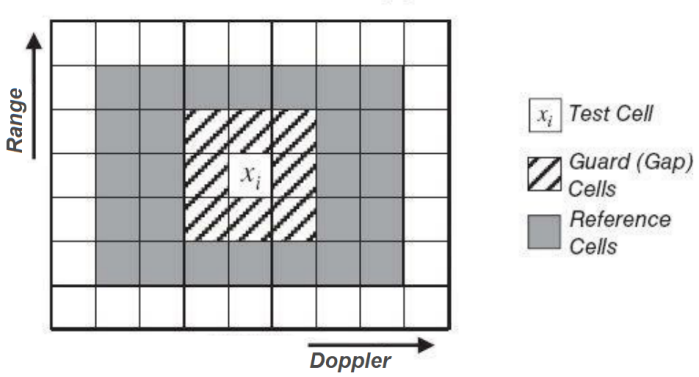

Figure 3.3: A two-dimensional CFAR window in range-Doppler domain, where the cell under test is indicated by x_i and where $N_g = [1,1]$ and $N_t = [2,1]$ [3]

For this detection technique, it is assumed that the training cells contain noise and interference with independent and identical distribution as in the cell under test (i.e., the noise and interference is homogeneous) and that these cells do not contain any targets. In real-life scenarios, the noise and interference are often non-homogeneous due to clutter. Moreover, in the scenario with a high density of targets, the latter assumption can limit the detection performance significantly. To have a good estimation of the noise level, all targets should be separated from each other by at least the CFAR window size. When a cell under test represents a target and one or more other targets are located among the reference test cells, the threshold will increase such that the target in the test

cell will be missed. This is called *target masking*, and obviously this will decrease the probability of detection P_D [3].

So far it is explained that the noise statistics are estimated by taking the mean of all reference test cells, commonly known as the *cell averaging* CFAR, abbreviated by CA-CFAR. This method is widely used for FMCW radar applications since it can automatically adapt to noise variance changes and often it can meet the earlier mentioned assumptions. This method achieves an optimal detection performance in a homogeneous background with well-separated targets, however, this is often not realistic. To overcome this problem, an alternative approach is introduced: instead of estimating the noise background with the mean of all reference test cells, the *ordered statistics* detector (OS-CFAR) chooses the test statistics within the ordered set of values of the reference test cells. This method simply ranks the received amplitudes/powers according to their value, and the k^{th} sample of these ranked values will be selected. If chosen correctly, outliers due to non-homogeneous background noise or target present in the test cells will be discarded, at the price of a slightly decreased detection performance [3, 5]. It has been shown in [61] that choosing $k \approx 3N/2$ (with N being the number of total reference test cells) leads to an optimal detection performance, similar to the CA-CFAR detector under true homogeneous background noise. In Fig. 3.4, a comparison between CA-CFAR and OS-CFAR in a scenario with two closely spaced targets is visualized. As can be seen, the rank of the OS-CFAR has been chosen correctly and therefore both targets are detected correctly, while with a CA-CFAR detector, the target with lower SNR is masked.

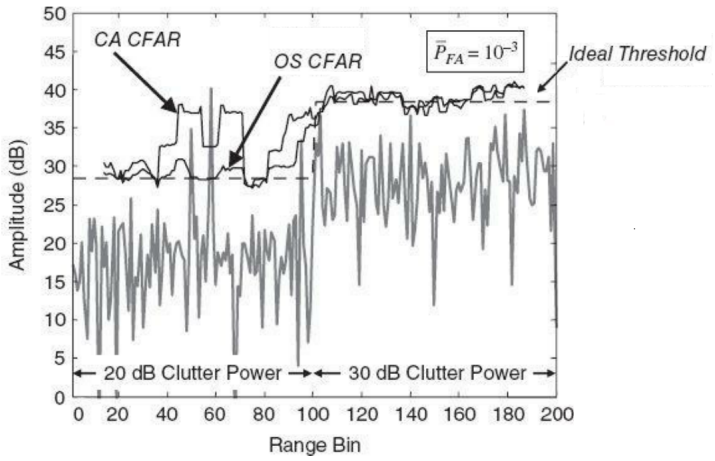

Figure 3.4: A comparison of one-dimensional CA-CFAR and OS-CFAR in a scenario with two closely spaced targets with respectively an SNR of 15 dB and 20 dB [3]

Other extensions of the CA-CFAR detector are the SOCA-CFAR and the GOCA-CFAR, which both make use of separating the mean estimation in both the mean of only half of the reference test cells, at one side of the cell under test and the mean of the other half of the reference test cells on the other side of the cell under test. In a scenario with densely spaced targets, the SOCA-CFAR chooses the lowest noise level and therefore easily detects two closely spaced targets, since only the mean of the reference cells that do not include a target is considered to estimate the noise level. When the noise is highly non-homogeneous, this detector will produce false alarm detections at a so-called clutter edge, from where the noise level suddenly increases. In contrast, the GOCA-CFAR chooses the greatest noise level. This ensures that the number of false alarms due to a clutter edge is reduced significantly, but closely spaced targets will be masked and therefore missed more often.

3.1.4. Target detection in PARSAX radar data

The discussed detection methods are implemented in MATLAB and are applied to radar data captured by PARSAX. The detectors will be compared by analyzing their performance when trying to detect the targets that can clearly be seen in the range-Doppler plot from Fig. 2.9b on page 21. Note that an MTI-filter has been applied to suppress static clutter so that only targets with nonzero Doppler velocity are analyzed. This drops some valid detections of observed vehicles with low radial velocity, especially when the car moves orthogonal to the sight vector. For all detectors, the probability of false alarm P_{FA} is set to 10^{-8}, which is in the range of commonly-used values for the P_{FA}. With 512 pulses per burst and 300 range bins, only one or two cells will result in a false alarm, which is acceptable.

First, the non-adaptive detector will be analyzed. The fixed threshold depends on the noise statistics as provided in Fig. 3.2 and Appendix A.6. From these figures, it can be derived that for a fixed, given P_{FA}, the threshold will be set at approximately 42 dBm. The analyzed range-Doppler frame and the resulting detection map can be seen in Fig. 3.5, where all detections are indicated by a red rectangular box. These plots show that most targets that are clearly visible, are detected. However, the targets with a smaller return amplitude are not detected, and therefore this non-adaptive threshold approach does not provide a good detection performance. Decreasing the threshold could solve this problem, but will also result in an increased number of targets that are merged into a single cluster. Therefore, there is a trade-off between the number of missed detections and the number of merged target detections.

As discussed, a more robust approach is the CFAR-detector, which dynamically estimates the local noise characteristics and computes a threshold for each cell, such that the probability of false alarm P_{FA} is kept constant. Different CFAR techniques applied in the range-Doppler domain can be implemented utilizing the `phased.CFARDetector2D`-object in MATLAB. Again, the probability of false alarm P_{FA} is set to 10^{-8}. Moreover, the number of guard cells N_g is set to $[6,4]$, the average size of a target in the range-Doppler spectrum, and the number of training cells N_t is fixed at $[6,6]$. Both the CA-CFAR and OS-CFAR are implemented and the resulted detection maps can be found in Fig. 3.6 and Fig. 3.7, respectively.

In comparison with the non-adaptive threshold detector, the CFAR detectors show a more realistic target detection map, with each cluster having a similar length in range direction. As has been discussed before, the CA-CFAR indeed struggles with detecting targets in a densely spaced environment. Many targets that are closely spaced in the range-Doppler map are missed, and many noise peaks are marked as a detection, which is not desired. To overcome these problems, the OS-CFAR is applied and indeed shows a better detection performance. Nevertheless, still, some detections with unrealistic size and unrealistic velocity are detected. Therefore, a filter will be applied, as will follow in Section 3.1.5.

In order to compare these detectors in more detail, a two-dimensional slice of a range-Doppler frame with the corresponding (non-normalized) threshold values is plotted in Fig. 3.8, similar as Fig. 3.4. It can be seen that the fixed threshold shows a bad detection performance by only detecting one peak. Moreover, the CA-CFAR-detector misses a few peaks that are clearly representing a target due to target masking, for example, the peaks around 3670 m and 3810 m. The OS-CFAR is able to cope with these closely spaced peaks. Thus, the OS-CFAR shows the best detection performance and therefore it will be used for further processing. The range-Doppler spectra and the detection maps resulted from the OS-CFAR detector for other polarizations can be found in Appendix B.1 and B.2.

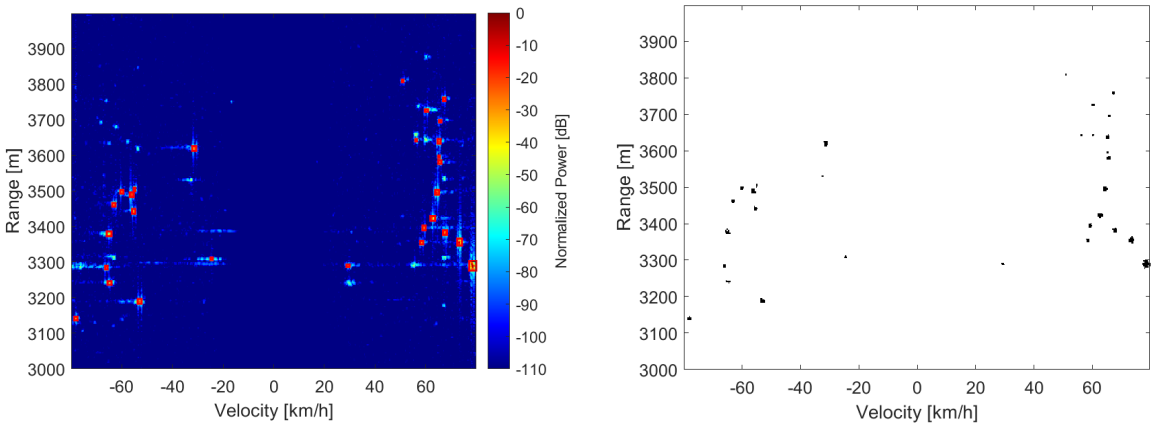

Figure 3.5: Results of the non-adaptive threshold detector, visualized in the first range-Doppler frame (HH-polarized) and the corresponding binary detection map

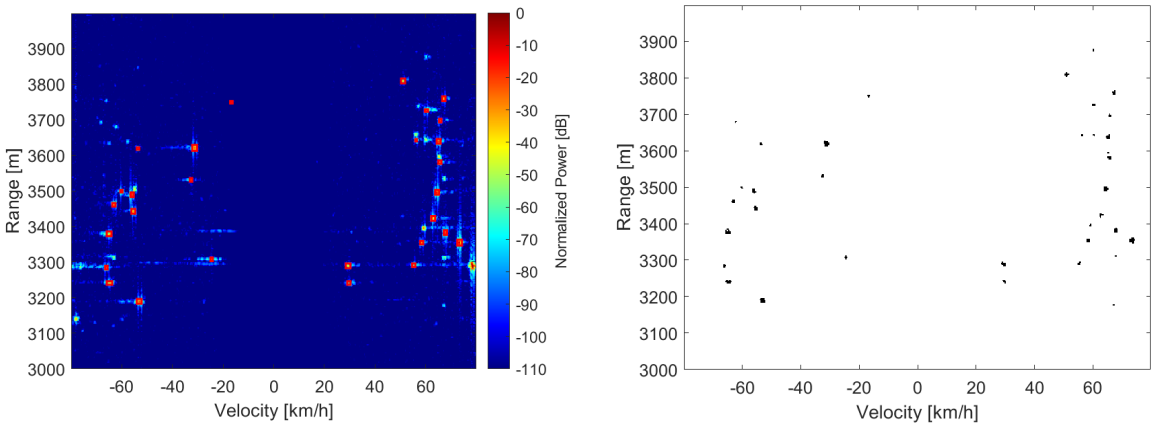

Figure 3.6: Results of the CA-CFAR detector, visualized in the first range-Doppler frame (HH-polarized) and the corresponding binary detection map

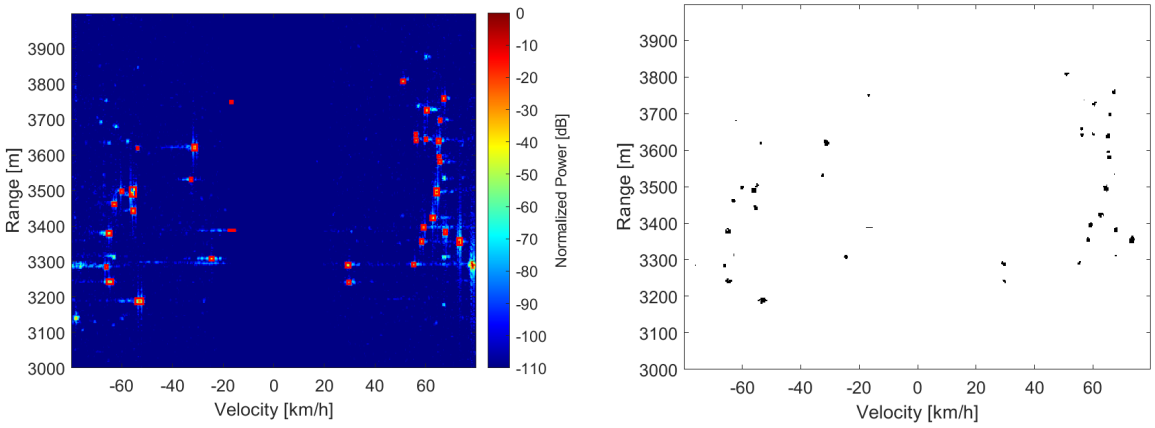

Figure 3.7: Results of the OS-CFAR detector, visualized in the first range-Doppler frame (HH-polarized) and the corresponding binary detection map

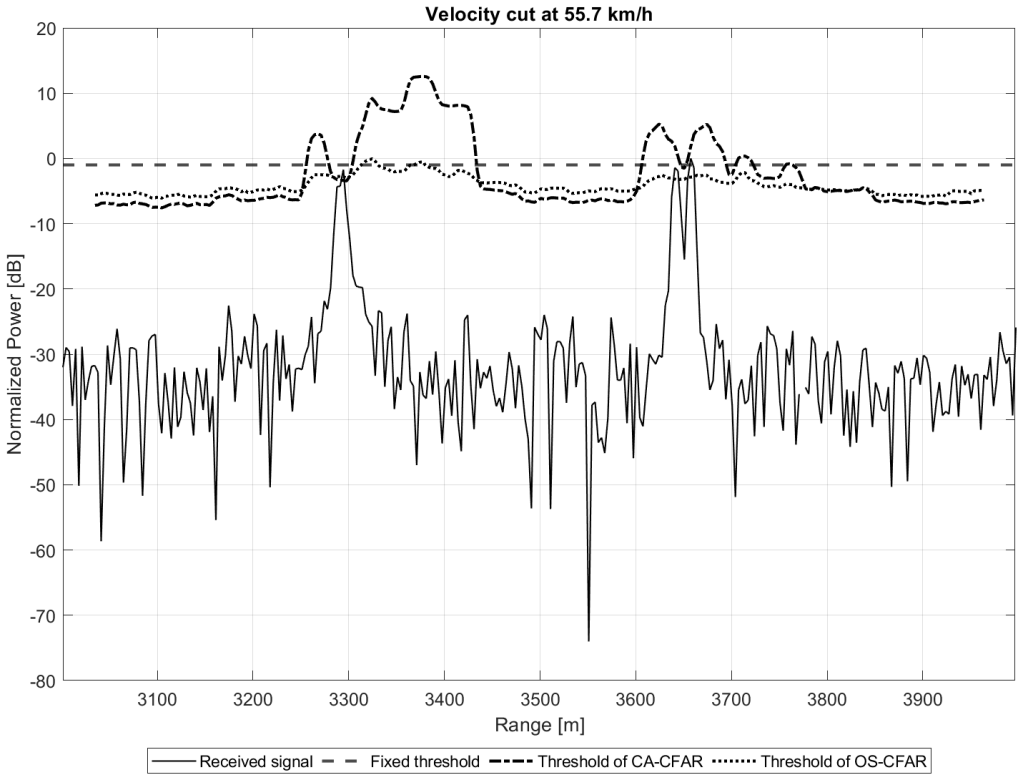

Figure 3.8: A two-dimensional slice at $v = 55.7$ km/h of the range-Doppler spectrum with the corresponding threshold values in order to compare the non-adaptive detector, CA-CFAR detector and OS-CFAR detector

3.1.5. Improvements of detection algorithm

The binary detection maps in Fig. 3.5b, 3.6b and 3.7b still contain some imperfections and distortions due to noise and the limitations of the target detection algorithm. For example, each target is represented by various detection cells, also known as clusters, which often do not represent the target correctly due to holes and protruded cells. Besides, clusters with a relatively small extent are probably false alarms and do not represent a target. Moreover, the CFAR-detector is not able to test all cells in the range-Doppler map. An approach to (partly) resolve this limitation will be introduced. At last, targets with a relatively small velocity, which are not filtered out in the signal processing chain by the MTI, can be discarded as well.

Morphological filter A morphological filter can be applied to compensate for imperfections and distortions of the clusters, and extract the relevant structures of the targets in the range-Doppler spectrum. The first morphological operator applied to each detection map is a *hole filler*. As the name already suggests, this operator fills the undetected cells that are surrounded by detected cells. The probability that this undetected cell is a missed detection is so high, that it can be assumed that it represents a target. Therefore, filling the holes will improve the target detection performance, as can be seen in Fig. 3.9b.

The second processing stage is probing each cluster with another known shape, referred to as a *structuring element*, which can be a disk, a hexagon, a square, a diamond, etc. The two fundamental morphological operators in this stage are *erosion* and *dilation*. The first operator checks whether the cluster fits a certain structuring element and keeps all detection cells such that the shape is included in the cluster itself. In contrast, the latter operator ensures that a cluster fits a certain shape by adding a layer of detection cells to the cluster. Hence, erosion will shrink a cluster dilation

expands the cluster. Often, these operators are performed after each other. Note that the order significantly affects the resulting image. When applying erosion before dilation, clusters that are smaller than this structural element will vanish completely, even before dilation takes place. On the other hand, when performing dilation before erosion, the original cluster will always remain, but there is a risk that closely spaced clusters will merge into one big cluster. Also, note that the shape itself needs to be selected properly [62]. The resulted binary output of applying first erosion, then dilation, with a disk-shaped element, can be seen in Fig. 3.9c. This clearly shows that small targets, which are probably false alarms due to noise peaks or clutter, are discarded.

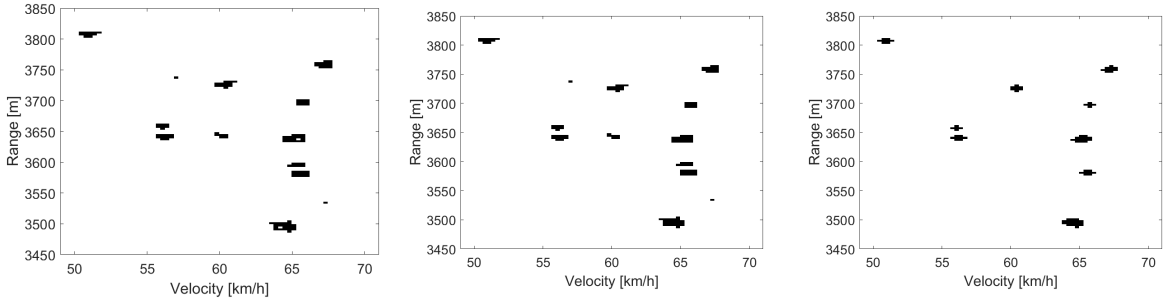

Figure 3.9: A zoomed-in version of the detection map (see Fig. 3.7b), with (a) the original map, (b) after *hole filling* and (c) after *erosion* and *dilation*

Limitation of CFAR-algorithm One disadvantage of the CFAR-algorithm is that not all cells in the range-Doppler map are tested. A few test cells are discarded due to the absence of reference test cells on one side, because of the width of the CFAR window. When investigating the range-Doppler maps in Fig. 3.6a and 3.7a in more detail, it can be seen that targets that are close to the outer sides of the two-dimensional map are not detected. Note that in the direction of the range axis, this is no problem, since no targets are present close to the top and bottom edges. On the other hand, along the velocity axis, this is the case and clearly visible targets are missed.

To mitigate this problem, the concept of Doppler ambiguity will be exploited. Due to the limitation of the sampling frequency in the Doppler domain (see Section 2.1) and due to the properties of the Fourier transformation, the data is circular along the Doppler axis, corresponding to the velocity axis. This means that the velocity axis can be extended bidirectionally, such that the left side of the range-Doppler map can be (partly) duplicated and re-used at the right-sided extension, and vice versa. By extending the range-Doppler map on both the left and right side with the corresponding width of the CFAR window, the number of reference test cells is increased. This means that cells close to the right and left edge can be tested as well. Illustrated by Fig. 3.10, it can be seen that the range of reference test cells is extended to the full velocity axis of the original range-Doppler map. After applying the CFAR detection algorithm to the extended range-Doppler map, the binary detection map will be cut into the original dimensions of the range-Doppler map. As can be seen, the targets close to the maximum unambiguous velocity are detected as well. Note that the morphological filter is applied as well and that therefore this plot shows improved results compared to the plot that can be seen in Fig. 3.7a.

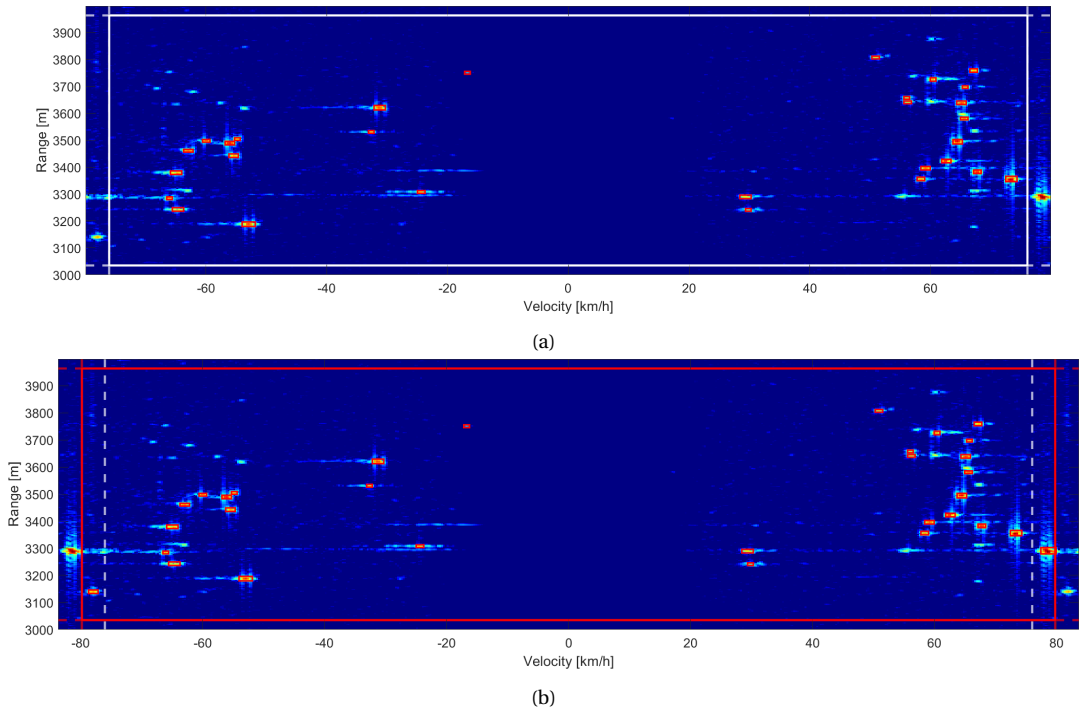

Figure 3.10: Results of the OS-CFAR detector, visualized in the first range-Doppler frame (HH-polarized) with (a) original dimensions and (b) extended dimensions, where the tested cells are enclosed by a white and a red rectangular box, respectively.

Additional high-pass filter In Section 2.3.4 on page 21 the principle of a Moving Target Indicator is explained. A 6^{th}-order Butterworth HPF is applied to filter out static clutter with a cut-off frequency that is equivalent to 20 km/h. However, this does not filter out all reflections from objects with a lower velocity completely. Therefore, an additional rectangular high-pass filter is applied to discard the detections that have a velocity smaller than 20 km/h. This is illustrated in Fig. 3.11, where a single cluster, indicated by a red box, will be discarded as a result of this additional HPF.

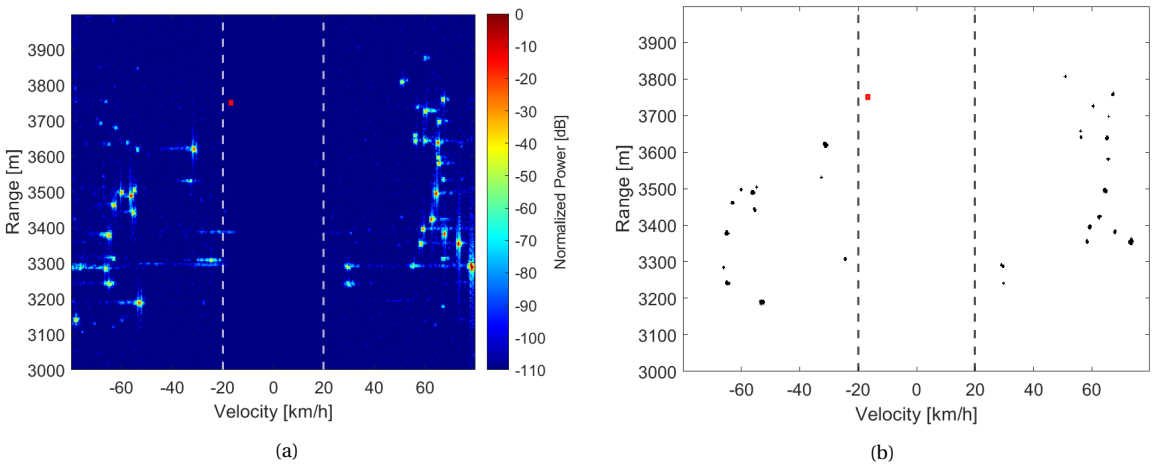

Figure 3.11: Results of the OS-CFAR detector, visualized in the first range-Doppler frame (HH-polarized) and the corresponding binary detection map. Here all targets with a velocity smaller than 20 km/h are indicated by a red box and will be filtered out.

3.2. Polarimetric sensor fusion

The proposed target detection algorithm, including the additional filters and mitigation of some limitations, is applicable to each data set corresponding to each element of the PSM. To take full advantage of the full polarimetric data set, all four data sets are exploited by a sensor fusion method to improve the detection performance. First, the concept of sensor fusion will be introduced. Subsequently, *polarimetric data fusion* and *detection decision fusion* will be explained and compared.

3.2.1. Concept of sensor fusion

Nowadays, dealing with enormous data sets that are generated by a high number of different types of sensors becomes a huge challenge. To create the ability to cope with this problem and to process such amount of data for the system, *sensor fusion*, often also referred to as *data fusion* or *information fusion*, is needed. Sensor fusion is combining two or more data sources in a way that generates a better understanding of the system, where *better* applies to more consistency, higher accuracy, and less dependency of data, resulting in higher quality and more relevant information. The goal of sensor fusion is to improve the quality of the data, implying less noise, less uncertainty, improved resolution, and fewer deviations from the actual system, and to increase the system's reliability. Nevertheless, due to a continuous inflow of different types of information from multiple sensors, various problems, such as data association, sensor uncertainty and management of data arise. The sensor fusion algorithm should be able to cope with these problems while improving the system performance in the area of data representation, measurement certainty (e.g., higher SNR), measurement accuracy, and data completeness [63].

The term *sensor fusion* is not completely in its place when talking about polarimetric radar, which is only a single sensor. However, since this type of radar is able to measure four polarizations simultaneously, sensor fusion methods can still be applied. Per burst of pulses, there are four range-Doppler frames and thus four detection maps. Two methods for the fusion of polarimetric radar data are described below.

3.2.2. Polarimetric data fusion

The first method to fuse polarimetric radar data is to merge the range-Doppler spectra of all four polarization elements into a single range-Doppler frame. The target detection algorithm will be applied to this final range-Doppler frame, and a single detection frame will be used for further processing. This is illustrated in Fig. 3.12.

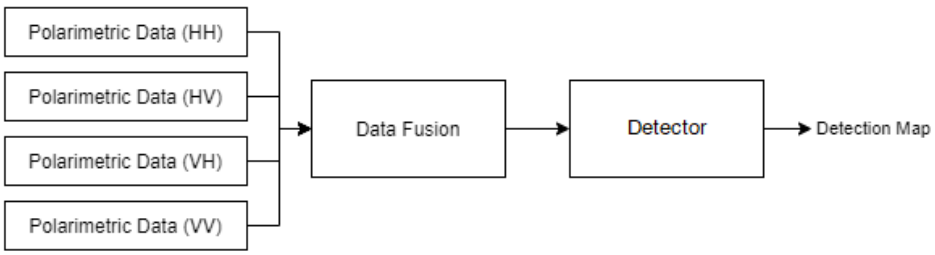

Figure 3.12: Data fusion of four range-Doppler spectra corresponding to the four elements of the PSM, after which a target detection algorithm is applied to a single range-Doppler frame

One approach of data fusion is the so-called *polarimetric matched filter* (PMF), which maximizes the target-to-clutter ratio. This method creates a detection map by fusing the data and applying a detection algorithm sequentially. Other techniques exist that combine the data fusion and the

detection algorithm processing step. For instance, the *optimal polarimetric detector* (OPD) incorporates polarimetric information in the likelihood ratio test (LRT). Unfortunately, since both the PMF and the OPD rely on the assumption that the polarimetric characteristics of both the target and the clutter are known, it is often not applicable to real-life scenarios.

However, other sub-optimal detectors that only require the characteristics of the clutter exist as well. One of these detectors is the *polarization whitening filter* (PWF), which minimizes the ratio of the standard deviation and the mean of the signal amplitude. This is achieved by using the (estimated) covariance matrix of the clutter $\mathbf{\Sigma}_c$ in the test statistic for the LRT. This can then be described by

$$\Lambda(\mathbf{S}) = \mathbf{X}^H(\mathbf{S}) \cdot \mathbf{\Sigma}_c^{-1} \cdot \mathbf{X}(\mathbf{S}), \tag{3.5}$$

where $\Lambda(\cdot)$ is the likelihood ratio as in Eq. (3.1) on page 24 and where $\mathbf{X}(\mathbf{S})$ is a vector of all complex elements of the S-matrix. Unfortunately this detector still requires additional information of the clutter.

Other examples of a full polarimetric detector are the *span detector* (SD) and the *polarimetric maximization synthesis detector* (PMSD), which both do not require any a priori information. These approaches are based on a non-coherent summation of all polarization elements as a test statistic for the LRT, defined by

$$\Lambda(\mathbf{S}) = |S_{HH}|^2 + |S_{HV}|^2 + |S_{VH}|^2 + |S_{VV}|^2, \tag{3.6}$$

and

$$\begin{aligned}\Lambda(\mathbf{S}) = &\frac{1}{2}\left(|S_{HH}|^2 + |S_{HV}|^2 + |S_{VH}|^2 + |S_{VV}|^2\right) + \\ &\frac{1}{2}\sqrt{\left(|S_{HH}|^2 - |S_{VV}|^2\right)^2 + 4\left|S_{HH}^* S_{HV} + S_{VV} S_{VH}^*\right|^2},\end{aligned} \tag{3.7}$$

respectively, where the PMSD has been proposed as an improvement with respect to the SD. A comparison between these two detectors indicates that the PMSD indeed shows the best practical detection performance [64, 65].

The PMSD has been implemented to merge the four range-Doppler maps, corresponding to the four elements of the PSM. Instead of using the fused data points as a test statistic for the LRT, an OS-CFAR detector will be applied to the fused range-Doppler map. Note that some CFAR input parameters, like N_t, N_g, P_{FA} and the rank may be adjusted for this new data set. The procedure for polarimetric data fusion is illustrated in Fig. 3.13. Here it is shown that the four range-Doppler maps are fused into a single range-Doppler map and that the OS-CFAR detector is applied to create a single binary detection map that can be used for further processing. As can be seen, the quality of data of the fused range-Doppler map is improved significantly compared to the single polarization data sets. The targets are clearly visible and can easily be detected by the proposed detector.

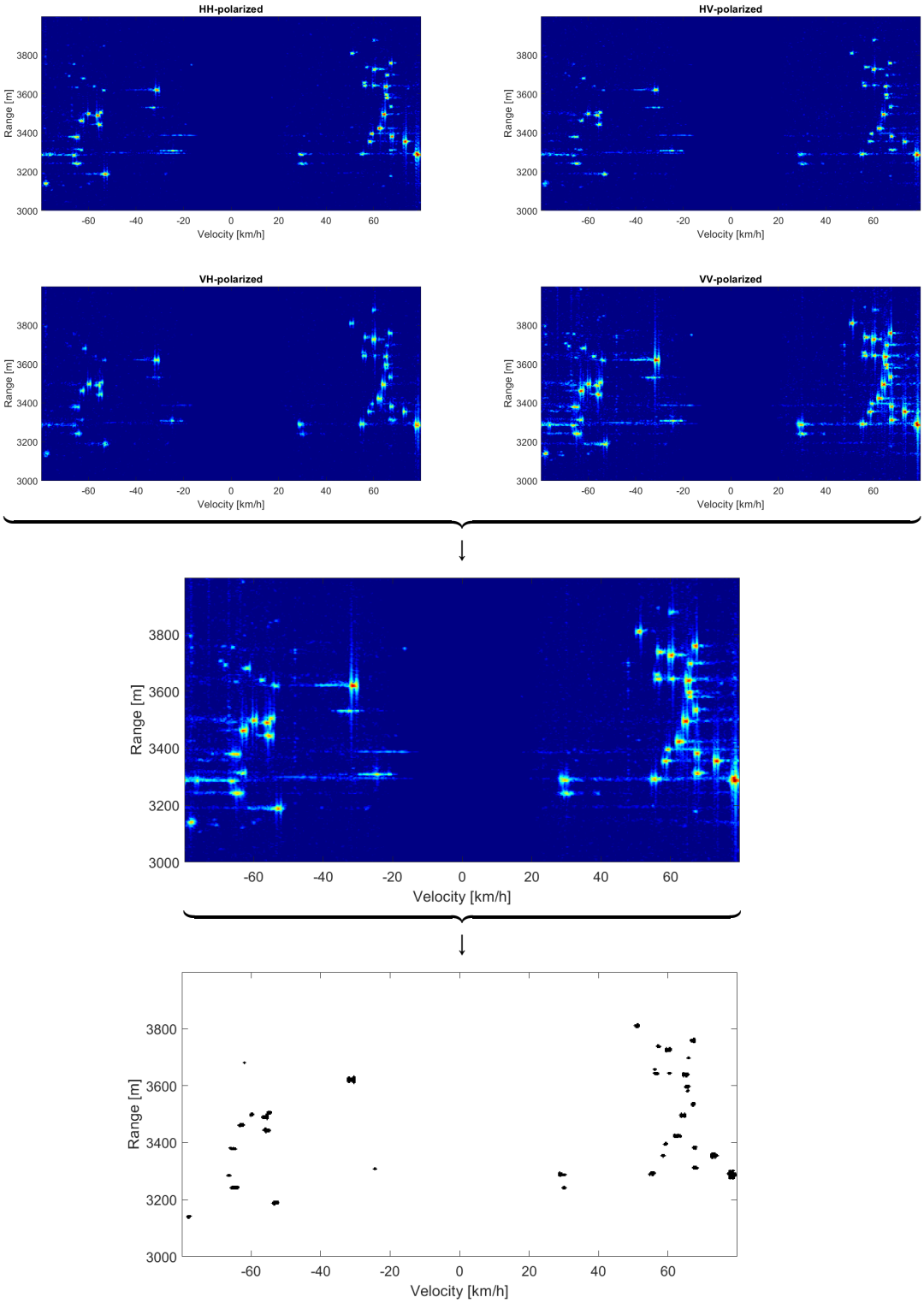

Figure 3.13: The process of polarimetric data fusion combining the polarimetric maximization synthesis detector (PMSD) and an OS-CFAR detector

3.2.3. Detection decision fusion

The second method of fusion is based on binary decision fusion. In contrast to the previous method, here the target detection algorithm is applied to all four range-Doppler frames of all four polarization elements, resulting in four detection maps. A decision fusion technique is implemented in order to combine these detection maps into a single, final detection frame for further processing. This decision fusion process should result in a detection map with a higher detection performance than any detection map from a single polarization channel [66]. This is illustrated in Fig. 3.14.

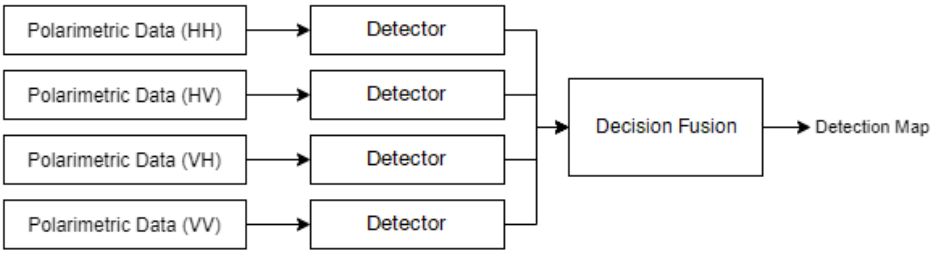

Figure 3.14: Decision fusion of four detection maps, before a target detection algorithm is applied to four range-Doppler frames, corresponding to the four elements of the PSM

Since the detection frames are binary maps, this fusion method often uses logical operators, referred to as *logical fusion*. In [67] several combinations of logical AND (denoted by $\cap$) and OR (denoted by $\cup$) operations on the four detection maps have been investigated. It turns out that the detection maps corresponding to cross-polarized range-Doppler frames are quite similar (due to reciprocal monostatic case [16]), but that co-polarized frames show strong variations due to the nature of the targets. It has been found that the following combination has the highest correlation with the data across all channels:

$$D' = (D_{HH} \cap D_{VV}) \cup (D_{HV} \cap D_{VH}), \tag{3.8}$$

where D' is the final detection map and where $D_{H,V}$ is the logical detection map corresponding to the four polarization elements HH, HV, VH, and VV, as given by the S-matrix. This method is applied to the detection map resulting from the OS-CFAR detector, after applying the morphological filter as discussed in Section 3.1.5. The zoomed-in version of the same detection maps as in Appendix B.2 are combined utilizing the polarimetric decision fusion as discussed above. The results of this fusion as described by Eq. (3.8) can be seen in Fig. 3.15

3.2.4. Comparison sensor fusion methods

One of the main advantages of the detection decision fusion method is its simplicity and effectiveness. However, the polarimetric data fusion method makes use of the amplitude information of all data sets directly and is, therefore, more realistic. It improves the quality of information and decreases the algorithm's computational costs. Hence, polarimetric data fusion will be selected for further processing. Based on [65], the PMSD shows the best detection performance in case of no knowledge about the clutter and therefore will be implemented.

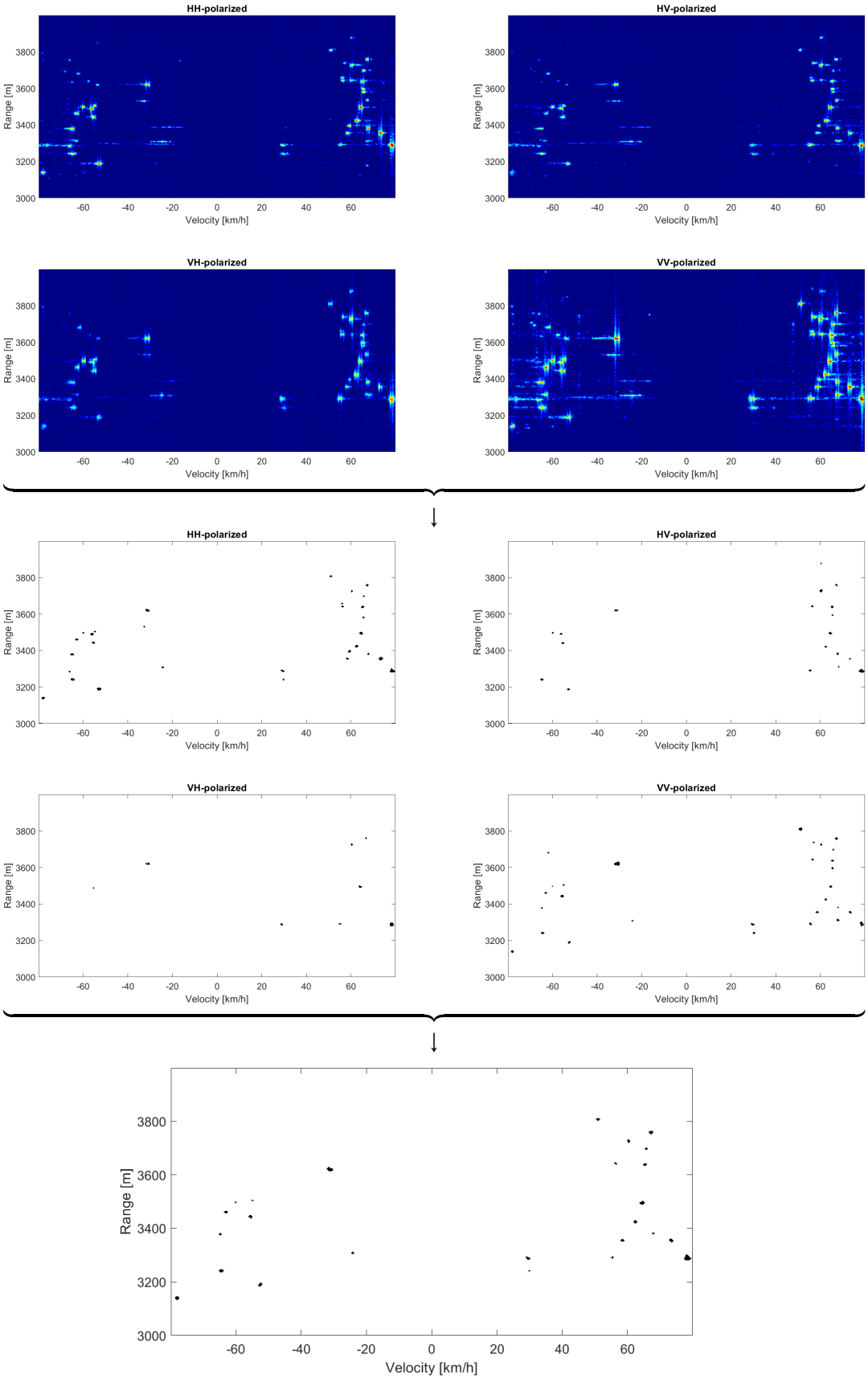

Figure 3.15: The process of detection decision fusion using logical operators and an OS-CFAR detector

3.3. Target clustering algorithm

Before applying a tracking algorithm to the final detection map, one last processing step needs to be performed. To simplify the tracking algorithm each target should be considered as a single detection point or a single cluster of detection points. Clustering is applied in order to output a single input per target for the tracking algorithm. Several clustering techniques for radar applications already exist. To select a certain clustering method, two assumptions have to be made. Firstly, the number of targets, and therefore the number of clusters, for each detection frame is unknown and is dynamic over time. Secondly, the shape of each cluster is unknown, although some physical constraints could be implemented. For example, the maximum length in the range direction of a vehicle is, including some margin, around 30 m. Clustering techniques can be categorized by partitioning and hierarchical algorithms: the first category of algorithms is based on clustering n detections in k clusters and the latter category creates a hierarchical decomposition of the data so that each subset of data contains a single target. The main difference between these two methods is the requirement to know a priori the number of targets k and the requirement to have a termination condition that defines a single cluster. Examples of some clustering techniques will be introduced and discussed.

k-Means clustering The best-known example of a partitioning clustering technique is the so-called *k-means clustering*. This method computes k detection points in the detection map of which the sum of the distance to each other is maximized. Subsequently, the remaining detection points will be assigned to the cluster that is the closest to one of the cluster center points. Since this method violates the first assumption (i.e., the total number of targets is required as input), it will not be analyzed further.

DBSCAN Another commonly used method is the *Density-Based Spatial Clustering of Applications with Noise* (DBSCAN), which forms clusters of arbitrary shape by finding high-density structures. This method clusters all points within an ϵ-neighborhood, where ϵ is the maximum distance between the detected cells. By assigning a minimum number of cells for each cluster, false detections due to noise spikes or interference are identified easily. Unlike k-means clustering, DBSCAN does not require prior knowledge of the number of targets, but it is needed to define the maximum distance ϵ, which is fixed for all targets in the frame. In the case of closely spaced targets, there is a risk that these targets will be merged into a single cluster, while in the case of a single target consisting of closely spaced detection clusters, it will be seen as two separate targets. To define ϵ, one could compute the distance of each detection point to its k-nearest neighbor and sort it in descending order. This so-called *sorted k-dist graph* can then be used to define the distances to detection points that are considered to be of the same cluster or to be noisy detections [68].

Flood-fill algorithm A more popular method of clustering used in image processing is the flood-fill algorithm. The clustering method based on the *flood-fill algorithm* simply searches through the detection map for unlabeled cells and labels each cell that is a connected component of another cell as the same cluster [69]. In a two-dimensional map, this connectivity can either be 4-way connected (i.e., along horizontal or vertical direction) or 8-way connected (i.e., along with horizontal, vertical, or diagonal direction). Since the detection map is a two-dimensional binary image, this relatively simple method can be applied.

Comparison In order to select the clustering algorithm, both the DBSCAN and the Flood-fill algorithm are implemented, utilizing the internal MATLAB functions `dbscan()` and `bwconncomp()`, respectively. Both clustering algorithms are applied to the detection map shown in Fig. 3.7b. Here

the input parameters for the DBSCAN method are based on the proposed method and realistic estimations, leading to $\epsilon = 2$ and the minimum number of detected cells for each cluster is 4. The results are presented in Fig. 3.16, where each cluster is indicated by a red rectangular box.

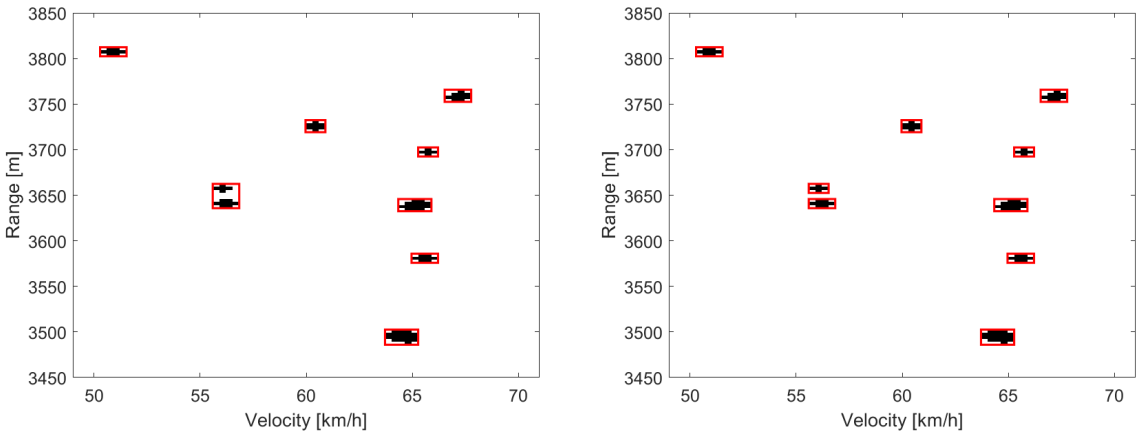

Figure 3.16: A zoomed-in version of the detection map (see Fig. 3.7b), with red rectangular boxed indicating the clusters defined by (a) the DBSCAN method and (b) the Flood-fill algorithm

As can be seen, both methods result in almost identical clusters. In this figure, the DBSCAN-method merges two separated detection clusters into a single cluster, whereas the Flood-fill algorithm produces two clusters. In many cases, these clusters are originating from a single target. Therefore, after finding a correct value for ϵ, the DBSCAN-method is more realistic and will be used for further processing.

3.4. Multi-target tracking in range-Doppler domain

So far the data processing steps for a single time frame have been discussed, but to create a complete feature database, each target needs to be tracked over time. Based on the detection map of each range-Doppler frame, a multi-target tracking problem will be proposed. Each multi-target tracking problem is different, dependent on the number of objects that are present, the sparsity of the objects, and the required performance of the tracking algorithm. Uncertainty of the observations or detections of the objects, and the prediction of the objects' paths make a multi-target tracking problem difficult.

In contrast with a single-target tracking problem, there are multiple measurement points and the challenge associated with this is to match each measurement point with the appropriate tracked object. Obviously, it is not desired to correct the prediction of one object using the measurement of another object. This would be relatively simple in a sparse situation with reliable measurements, but this is not the case when tracking many moving targets on a dense highway. This so-called data association problem is even more challenging, since most targets are represented by multiple range-Doppler cells, and therefore multiple clustered detections points. These targets are often known as *extended objects*.

Besides, the number of targets being tracked is not fixed. Targets can enter and can leave the radar observation range, causing new tracks to be created and existing tracks to be deleted. Track management needs to be incorporated into the tracking algorithm. This means that criteria for adding and removing tracks are needed, each target needs to have an identification attribute, and the way how to deal with false alarms and missed detections needs to be taken into account.

As can be seen, in order to handle all these uncertainties it is needed to decompose this problem into multiple parts. The basic elements of a Multiple Target Tracking (MTT) algorithm are illustrated in Fig. 3.17. Thus far, only the first block of this diagram is discussed. In this section, several methods and algorithms to fill in the remaining elements will be discussed.

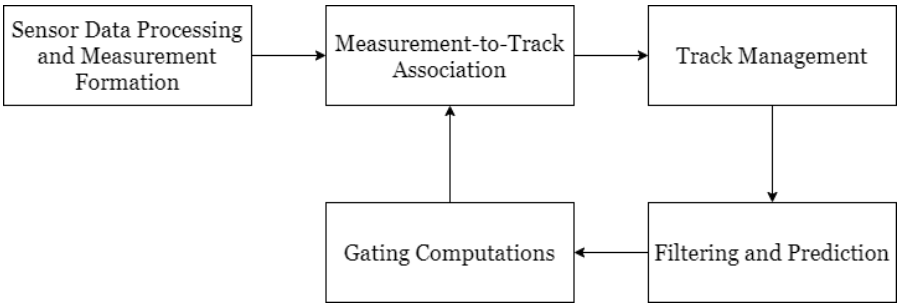

Figure 3.17: A diagram representing the basic elements of a conventional MTT-algorithm [51]

3.4.1. Filtering and prediction: Measurement model

For tracking purposes, it is assumed that each target is represented by a single measurement per cluster in the detection map, although it consists of multiple detected cells. This measurement is considered to be the centroid of its cluster and includes a range value R and a velocity value v, proportional to the Doppler frequency. Hence, for each target i at time frame k the measurement $\mathbf{z}^i[k]$, or for convenience, indicated by $\mathbf{z}^i_k$, is given by

$$\mathbf{z}^i_k = \begin{bmatrix} R^i_k \\ v^i_k \end{bmatrix} \tag{3.9}$$

The result of this measurement is an estimate of the exact coordinates of the target in the range-Doppler spectrum, but each measurement has its uncertainty due to noise and clutter. This uncertainty is described by the measurement covariance matrix $\mathbf{\Sigma}_n$. Since both the range and the velocity measurement is available, this matrix is given by

$$\mathbf{\Sigma}_n = \begin{bmatrix} \sigma^2_{n,R} & 0 \\ 0 & \sigma^2_{n,v} \end{bmatrix}, \tag{3.10}$$

where the measurement variances $\sigma^2_{n,R}$ and $\sigma^2_{n,v}$ are proportional to the range resolution and velocity resolution, respectively. Due to range migration during the integration time, the uncertainty of the range measurement is greater than the uncertainty of the velocity. Therefore, the variances are set to $5\Delta R$ and $1\Delta v$, as given by Eq. (2.9) and Eq. (2.11).

The estimation of the true coordinates of the target, also known as its *state*, can be improved by combining the measurements in a time series with some assumptions about the target's kinematic motion. The state of the i$^{\text{th}}$ target at the k$^{\text{th}}$ time frame $\mathbf{x}^i_k$, is described by its true range and true velocity but can be extended by more target properties, such as its acceleration or its size. Note that often not all state parameters can be measured. The state observation matrix $\mathbf{H}$ is used to select the state parameters that are observed, following that a noisy measurement can be described by

$$\mathbf{z}^i_k = \mathbf{H}\mathbf{x}^i_k + \mathbf{v}_n, \tag{3.11}$$

where $\mathbf{H}$ is a $N_{meas} \times N_{states}$-matrix and where $\mathbf{v}_n \sim \mathcal{N}(0, \mathbf{\Sigma}_n)$, containing zero-mean Gaussian measurement noise with variances given by $\mathbf{\Sigma}_n$.

3.4.2. Filtering and prediction: Kalman filter

In most tracking algorithms, the estimated state $\hat{\mathbf{x}}^i_{k|k}$ is updated by combining the measurement at time k and the predicted state $\hat{\mathbf{x}}^i_{k|k-1}$ based on the target's state at time $k-1$. The ratio of relying on the measurement and relying on the predicted state is known as the *tracking gain* [3]. A commonly-used method is the *Kalman filter*, which dynamically computes a tracking gain that minimizes the mean-square error (MSE) of the estimation at each step. The gain K is chosen automatically based on the target's trajectory and the measurement noise models, and this filter produces a state covariance matrix $\mathbf{Q}$ that provides a better measure of the estimation accuracy. The Kalman filter is achieved in two phases: the *prediction stage* and the *update stage*.

In the first stage the target's state $\hat{\mathbf{x}}_{k|k-1}$ (for convenience denoted without the target indicator i) will be predicted based on its previous state $\hat{\mathbf{x}}_{k-1|k-1}$ and the assumed target dynamics, described by the state transition model matrix $\mathbf{F}$. Besides, this stage computes the predicted state covariance matrix $\hat{\mathbf{Q}}_{k|k-1}$ based on its previous state covariance matrix $\hat{\mathbf{Q}}_{k-1|k-1}$ and the process noise covariance matrix $\mathbf{W}$. This can mathematically be described by

$$\begin{aligned} \hat{\mathbf{x}}_{k|k-1} &= \mathbf{F}\hat{\mathbf{x}}_{k-1|k-1}, \\ \hat{\mathbf{Q}}_{k|k-1} &= \mathbf{F}\hat{\mathbf{Q}}_{k-1|k-1}\mathbf{F}^T + \sigma_w^2\mathbf{W}, \end{aligned} \tag{3.12}$$

where σ_w^2 is the process noise variance. The state transition matrix $\mathbf{F}$ and the process noise covariance matrix $\mathbf{W}$ depend on the target's dynamic model, which will be introduced later. Subsequently, in the update stage, the Kalman filter computes the gain $\mathbf{K}_k$ based on the uncertainty of the predicted state, described by $\hat{\mathbf{Q}}_{k|k-1}$. Based on this gain, the target's current state $\hat{\mathbf{x}}_{k|k}$ and the target's current state covariance matrix $\hat{\mathbf{Q}}_{k|k}$ will be computed. The update equations of the Kalman filter are given by

$$\begin{aligned} \mathbf{K}_k &= \hat{\mathbf{Q}}_{k|k-1}\mathbf{H}^T\left(\mathbf{H}\hat{\mathbf{Q}}_{k|k-1}\mathbf{H}^T + \mathbf{\Sigma}_n\right)^{-1}, \\ \hat{\mathbf{x}}_{k|k} &= \hat{\mathbf{x}}_{k|k-1} + \mathbf{K}_k\left(\mathbf{z}_k - \mathbf{H}\hat{\mathbf{x}}_{k|k-1}\right), \\ \hat{\mathbf{Q}}_{k|k} &= \left(\mathbf{I} - \mathbf{K}_k\mathbf{H}\right)\hat{\mathbf{Q}}_{k|k-1}, \end{aligned} \tag{3.13}$$

such that, based on these equations, the state of each target will be predicted and updated in the next frame. In the first frame (i.e., $k = 1$), no predicted state and predicted covariance matrix are available. Therefore, the Kalman filter needs to be initialized with a pre-determined initial state $\mathbf{x}_0$ and covariance matrix $\mathbf{Q}_0$. The initialization values will be discussed later.

3.4.3. Filtering and prediction: State dynamics model

As has been mentioned before, the Kalman filter assumes that the state transition matrix $\mathbf{F}$, observation matrix $\mathbf{H}$ and process noise covariance matrix $\mathbf{W}$ have been selected properly. In our application, moving vehicles in a straight way will be tracked. Therefore, it can be assumed that the target's dynamic behavior is quite predictable and can thus be modeled quite well. Two target dynamics models will be introduced. Many more target dynamic models exist but are not discussed here, since they are not relevant to our application.

Target dynamics model: Constant Velocity (CV) In the first model it is assumed that the vehicle drives with a constant velocity, i.e., has zero acceleration, and is known as the CV-model. To describe this model mathematically, only two states are required: the range R and velocity v. Basic kinematic equations result into the following state equations:

$$\mathbf{x}_{k+1} = \begin{bmatrix} R_{k+1} \\ v_{k+1} \end{bmatrix} = \begin{bmatrix} R_k + v_k T \\ v_k \end{bmatrix}, \tag{3.14}$$

where T is the time between successive frames. From this, the state transition matrix $\mathbf{F}$ can easily be derived, and since both states are measured, the observation matrix $\mathbf{H}$ as well. Together with the process noise variance $\mathbf{W}$, the CV-model can be described by

$$\mathbf{F} = \begin{bmatrix} 1 & T \\ 0 & 1 \end{bmatrix}, \mathbf{H} = \begin{bmatrix} 1 & 0 \\ 0 & 1 \end{bmatrix}, \mathbf{W} = \begin{bmatrix} T^3/3 & T^2/2 \\ T^2/2 & T \end{bmatrix} \tag{3.15}$$

In case this model is used, the Kalman filter will be initialized by assigning the measurement of each target in the first frame $\mathbf{z}_0^i$ to the initial target state $\mathbf{x}_0^i$. Moreover, the initial covariance matrix $\mathbf{Q}_0^i$ will be set to the noise variance matrix $\mathbf{\Sigma}_n$.

Target dynamics model: Constant Acceleration (CA) Another target dynamics model is the CA-model. Where in the previous case it was assumed that the target's acceleration is zero, this model estimates the acceleration for each frame for each target by the Kalman filter equations. Therefore, the state representation needs to be extended with a 3$^{\text{rd}}$ parameter, the acceleration a. The basic kinematic equations will now result as follows:

$$\mathbf{x}_{k+1} = \begin{bmatrix} R_{k+1} \\ v_{k+1} \\ a_{k+1} \end{bmatrix} = \begin{bmatrix} R_k + v_k T + \frac{1}{2} a_k T^2 \\ v_k + a_k T \\ a_k \end{bmatrix}, \tag{3.16}$$

where T is again the time between each frame. Similar to before, the system dynamics of the CA-model can easily be derived, resulting in

$$\mathbf{F} = \begin{bmatrix} 1 & T & T^2/2 \\ 0 & 1 & T \\ 0 & 0 & 1 \end{bmatrix}, \mathbf{H} = \begin{bmatrix} 1 & 0 & 0 \\ 0 & 1 & 0 \end{bmatrix}, \mathbf{W} = \begin{bmatrix} T^4/4 & T^3/2 & T^2/2 \\ T^3/2 & T^2 & T \\ T^2 & T & 1 \end{bmatrix} \tag{3.17}$$

In case this model is used, initialization of the first two states will be similar as for the CV-model. The added state (i.e., the acceleration) will be initialized at $a = 0$ with variance $\sigma_{n,a}^2 = 1$ [51].

3.4.4. Gating computations

Now that the Kalman filter is introduced, it is possible to predict and update each target's state according to a certain dynamics model. In a single-target tracking problem, it is relatively easy to track the object with a single noisy measurement per time frame. However, in a multi-target tracking problem, multiple measurements and multiple tracks need to be investigated. The challenge to associate each measurement to a certain track is called the *data association problem*, as is illustrated in Fig. 3.18. Before this data association problem will be discussed, the problem size will be narrowed down.

Firstly, each target is represented by a single cluster with its centroid and its size as main properties. As mentioned before, the centroid of each cluster will be considered as a single measurement. Hence, only one measurement can be assigned to a single track. Secondly, so-called *gating* will be applied. Gating is a technique for eliminating measurement-to-track combinations that are unlikely in order to reduce the number of combinations that must be considered in the association process. Based on a certain distance between each new measurement and the predicted state of each target,

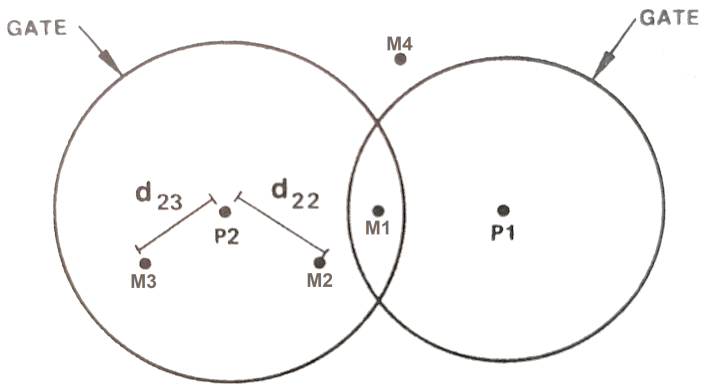

Figure 3.18: Illustration of an example of a data association problem with four measurements M_i, two predicted states P_j, and the (statistical) distance $d_{i,j}$. A spherical gate is applied so that M_4 is discarded and that M_1 could be associated with both predicted states. Moreover, the track of P_2 has multiple measurement candidates [51].

all measurement-track combinations that are outside a certain gate, and thus are unlikely, will be discarded.

Commonly-used gating approaches are the rectangular and spherical gates. Respectively, when a measurement is within a certain rectangular box $[d_R, d_v]$ or within a certain radius d_s around the predicted state of a target, it will be considered as a candidate measurement that can be assigned to the concerning track. A more advanced approach is to consider the statistical distance: the likelihood for a certain measurement to be associated with the track. Only measurements with a minimum likelihood that it could originate from the object corresponding to the track will be considered being within the gate, also known as the *correlation gate* or *hyperellipsoid gate*. A generalized distance measure based on the statistics is the so-called *Mahalanobis distance*, denoted by d_M. For measurement i and track j, these gating distances in the two-dimensional range-Doppler spectrum can mathematically be described as

$$\begin{aligned}
&\textbf{Rectangular gate:} && \begin{cases} \left| R_k^i - R_{k|k-1}^j \right| \leq d_R \\ \left| v_k^i - v_{k|k-1}^j \right| \leq d_v \end{cases} \\
&\textbf{Spherical gate:} && \left\| \mathbf{z}_k^i - \mathbf{H}\hat{\mathbf{x}}_{k|k-1}^j \right\|_2 \leq d_s \\
&\textbf{Hyperellipsoid gate:} && \left[\mathbf{z}_k^i - \mathbf{H}\hat{\mathbf{x}}_{k|k-1}^j \right]^T \mathbf{S}_{j,k}^{-1} \left[\mathbf{z}_k^i - \mathbf{H}\hat{\mathbf{x}}_{k|k-1}^j \right] \leq d_M
\end{aligned} \tag{3.18}$$

where $\|\cdot\|_2$ is the Euclidean norm and where $\mathbf{S}_{j,k}$ is the covariance matrix of track j at time frame k. This covariance matrix combines the predicted covariance of the target state $\hat{\mathbf{Q}}_{k|k-1}$ and the covariance of the measurement uncertainty $\mathbf{\Sigma}_n$, which is then given by

$$\mathbf{S}_{j,k} = \mathbf{H}\hat{\mathbf{Q}}_{k|k-1}^j \mathbf{H}^T + \mathbf{\Sigma}_n, \tag{3.19}$$

which is exactly the denominator of the Kalman gain calculation in Eq. (3.13). Although this latter approach is computationally more expensive, it is selected in order to achieve the most optimal tracking performance [51].

3.4.5. Measurement-to-track association: Method

The main challenge of multi-target tracking is the measurement-to-track association: which measurements should be assigned to which track. After the gating procedure, for each track, only a

certain number of measurements can potentially be associated with the concerning track. Several commonly-used algorithms for this association problem will be introduced. How to deal with missed detections, false alarms, tracks with no measurements within its gate, and measurements that are within no gate, will be discussed in Section 3.4.7.

Global Nearest Neighbor (GNN) To choose the most likely measurement for each track, the "cost" for each measurement within the gate with respect to the track should be computed. Since the hyperellipsoid gating method has been selected, the Mahalanobis distance will be used as the cost. A simple approach is to assign the measurement with the lowest cost to each track, independent of the other tracks. This approach is known as the *Nearest Neighbor* (NN) method. To prevent that one measurement is assigned to multiple tracks, each associated measurement will be removed from the list of potential candidates for the following unassigned tracks. However, this could result in wrongly matched pairs due to the sequence of processing. Instead, a cost matrix C containing the cost of all measurements within the gate to each track, denoted by $C_{i,j}$, can be used to find the optimal combination of measurement-to-track pairs that minimizes the total cost [3]. Given the constraints that each measurement can only be assigned once and that each track can only be associated with at most one measurement, this method can mathematically be described as

$$\begin{aligned} \min \quad & \sum_{i=1}^{N_{meas}} \sum_{j=1}^{N_{tracks}} C_{i,j} \cdot z_{i,j} \\ \text{s.t.} \quad & C_{i,j} \leq d_M \\ & \sum_{i=1}^{N_{tracks}} z_{i,j} = 1, \quad \forall j \\ & \sum_{j=1}^{N_{meas}} z_{i,j} = 1, \quad \forall i \end{aligned} \tag{3.20}$$

where d_M is the Mahalanobis distance for gating (see Section 3.4.4) and where $z_{i,j}$ is equal to 1 when measurement i is assigned to track j, and otherwise is equal to 0. This total cost minimization is known as the *Global Nearest Neighbor* (GNN) method [51].

Joint Probabilistic Data Association (JPDA) A more advanced algorithm is the *Probabilistic Data Association* (PDA), which is based on the combination of all potential measurements and the likelihood of each measurement that represent the target that needs to be tracked. Each track is updated with a weighted average of all measurements that are within its gate, where the weights depend on this likelihood. It can be seen as a weighted sum of all PDF that results in a single Gaussian distribution for the target state. This method can easily be extended to a multi-dimensional data association filter, by analyzing the multi-dimensional PDF of each measurement, which is known as the *Joint Probabilistic Data Association* (JPDA). The weights of the filter then not only depend on a single parameter, such as only range or Doppler/velocity, but on both range, Doppler, and even more state parameters (e.g., acceleration, target size). It can be extended even further, by adding polarization information into this framework [70].

Multiple Hypotheses Tracking (MHT) Instead of associating a measurement to each track at each time frame, Multiple Hypotheses Tracking (MHT) estimates the track based on a series of measurements at multiple time frames. This method is based on a set of data association hypotheses considering all measurement-to-track pairs with a certain probability. At each frame, this set of hypotheses is expanded with new hypotheses based on new measurements and potential measurement-to-

track pairs. All hypotheses are ranked based on the prior probability of the concerning hypothesis, the density of new targets, the density of false alarms, the probability of detection P_D, and the number of previously known targets. As can be imagined, this results in a problem with many hypotheses. A simple approach to simplify this problem is by pruning all unlikely hypotheses with a specific probability threshold, or by combining multiple similar hypotheses [51, 71].

Comparison For our application, the GNN approach has been selected, because of its simplicity and effectiveness. This algorithm is implemented using the MATLAB-functions `pdist2()` and `matchpairs()`, which are capable of computing the complete cost matrix using the Mahalanobis distance and match each track with a measurement that is within the gate of the target's predicted state. Moreover, it automatically creates an array of unassigned measurements and unassigned tracks.

3.4.6. Measurement-to-track association: MHT with Doppler ambiguity

Thus far it has been assumed that the measured range and velocity is the target's true state plus additional noise (see Section 3.4.1). However, as discussed in Section 2.1, due to aliasing in the Doppler spectrum during range-Doppler processing vehicles with a radial velocity higher than the maximum unambiguous velocity v_r^{max} may show a folded Doppler frequency, therefore a folded velocity. In Section 2.3 it has been shown that the maximum unambiguous velocity that can be handled by the PARSAX radar is ±79.8 km/h, resulting in a folding velocity v_f of 159.6 km/h. This means that the velocity measurement of a vehicle with a true radial velocity of, for example, 90 km/h is folded and will be represented in the Doppler spectrum at approximately −70 km/h. With real-world data of vehicles driving at a highway, this maximum unambiguous velocity is often exceeded, resulting in incorrect velocity measurements, and thus incorrect state predictions. The true unambiguous velocity v_k^U and the ambiguous velocity measurement v_k^A are related by

$$v_k^U = v_k^A + n_d v_f, \tag{3.21}$$

where n_d is the Doppler ambiguity order and can be any integer from the Doppler ambiguity order set $n_d \in [-n_d^{max}, \ldots, n_d^{max}]$. Assuming that the maximum true velocity of a vehicle on a highway $v_k^{U,max}$ is ±159.6 km/h, and given that $|v_k^{U,max}| \leq n_d^{max} v_f$, the velocity measurement can only be folded once, i.e., $n_d^{max} = 1$. Hence, n_d can be −1, 0 or +1, and thus the number of possible Doppler ambiguity orders N_d will be 3. This new assignment problem can be described as a three-dimensional data association problem with the following constraints:

$$\begin{aligned} \sum_{n=1}^{N_d} \sum_{i=1}^{N_{meas}} z_{i,j,n} &\leq 1, \quad \forall j \\ \sum_{n=1}^{N_d} \sum_{j=1}^{N_{tracks}} z_{i,j,n} &\leq 1, \quad \forall i \\ \sum_{n=1}^{N_d} z_{i,j,n} &= 1, \quad \forall i,j \end{aligned} \tag{3.22}$$

with

$$z_{i,j,n} = \begin{cases} 1, & \text{measurement } i \text{ associated with track } j \\ & \text{and Doppler ambiguity order } n_d(n) \\ 0, & \text{otherwise,} \end{cases} \tag{3.23}$$

where $n_d = [-1, 0, 1]$. These constraints entail that measurements can only be assigned once, that tracks can only be associated once and that only one Doppler ambiguity order can be assigned to a measurement-track pair.

To handle the uncertainty of the target's Doppler ambiguity order, a hypothesis-oriented MHT-based approach is introduced by Li et al. [72]. As discussed in the previous section, the main idea of MHT is to analyze a set of hypotheses for each frame and select the one with the highest probability. Whereas MHT is usually used to find the most likely measurement-to-track combinations [73], here it is modified to evaluate multiple hypotheses in order to find the most likely Doppler ambiguity order. Due to this modification, this algorithm is able to handle the Doppler ambiguity problem independent of the choice of the PRF, which proportionally affects v_f. An MTT-algorithm has been proposed that decomposes the three-dimensional measurement-to-track-to-Doppler ambiguity order problem into two two-dimensional data associations. This work solves the measurement-to-track association problem based on the original MHT and handles the Doppler ambiguity order uncertainty using an MHT-based Bayesian approach. For each measurement-to-track pair, sub-hypotheses are generated to find the value of the Doppler order with the highest probability. Although this method shows significant improvements in terms of tracking accuracy and false track rates compared to the original MHT, the total number of hypotheses will grow exponentially over time without appropriate gating and pruning [72].

In our algorithm, the consequences of this limitation are minimized by applying the computationally less expensive GNN-algorithm instead of the original MHT for the measurement-to-track association, while maintaining the MHT-based algorithm to handle the Doppler ambiguity. Instead of dealing with one large MHT assignment problem, this approach is based on many, relative small problems with only $N_d = 3$ possible hypotheses per track, given that $n_d^{max} = 1$ (i.e., $n_d \in [-1, 0, +1]$). This approach decreases the total number of hypotheses significantly and therefore improves the computational cost.

On top of that, given that each measurement is folded once at maximum, the number of hypotheses per track N_d can even be decreased from 3 to 2, by discarding $n_d = +1$ for targets with a measured positive velocity and $n_d = -1$ for targets with a measured negative velocity, resulting in:

$$\begin{cases} n_d \in [-1, 0], & v_k^A > 0 \\ n_d \in [0, +1], & v_k^A < 0 \end{cases} \tag{3.24}$$

Thus, for each existing track two hypothesis are formed: the null-hypothesis $\mathscr{H}_0$, meaning that the target's state is *not folded* (i.e., $n_d = 0$), and hypothesis $\mathscr{H}_1$, meaning that the target's state is *folded* (i.e., $n_d = -1$ or $n_d = +1$). To determine the probability of each sub-hypotheses, the statistical Mahalanobis distance between all measurements and all original predicted states $\hat{\mathbf{x}}_{k|k-1}^U$, and between all measurements and all ambiguous predicted states $\hat{\mathbf{x}}_{k|k-1}^A$ with folded velocity, is computed. To describe the state in the range-Doppler domain only the range prediction needs to be compensated for this incorrect velocity measurement. This means that the predicted state with ambiguous Doppler $\hat{\mathbf{x}}_{k|k-1}^A$ needs to be adjusted before updating the state with the new measurement, extending Eq. (3.12) as

$$\hat{\mathbf{x}}_{k|k-1}^U = \mathbf{F}\hat{\mathbf{x}}_{k-1|k-1}^A + \begin{bmatrix} n_d v_f T \\ \mathbf{0}_{N-1} \end{bmatrix}, \tag{3.25}$$

where T is again the time between each frame, $\mathbf{0}_{N-1}$ is a vector containing zeros such that the vector has the same length as the state vector and where n_d is -1 or $+1$, depending on the velocity measurement of $\hat{\mathbf{x}}_{k|k-1}^U$.

3.4.7. Track management

As introduced earlier in this section, another issue occurs when a measurement is a false alarm, target detection is missed, or when the number of measurements N_i is not equal to the number of existing tracks N_j. This could happen when targets enter or leave the radar's field-of-view, are unobservable due to occlusion or due to clutter. Therefore, *track management* is required. Two methods, the M/N logic test and the Sequential Probability Ratio Test (SPRT), are implemented and compared. Keep in mind that each track is updated and predicted according the equations given by Eq. (3.12) and (3.13) on page 41. Note that in case of a missed detection, a measurement $\mathbf{z}_k$ is not available. In that situation, the predicted state will fully rely on its prediction, following Eq. (3.26) given by

$$\hat{\mathbf{x}}_{k|k} = \begin{cases} \hat{\mathbf{x}}_{k|k-1} + \mathbf{K}_k\left(\mathbf{z}_k - \mathbf{H}\hat{\mathbf{x}}_{k|k-1}\right) & \mathbf{z_k}\text{available} \\ \hat{\mathbf{x}}_{k|k-1} & \mathbf{z_k}\text{not available} \end{cases} \tag{3.26}$$

M/N logic test The first method is a rule-based test for track confirmation and deletion: this rule simply checks whether M measurements are received and associated to a track within N frames. When a new track meets this requirement, the tentative track is confirmed. Similarly, if M times within N frames no measurement is assigned to a track, it will be deleted [73, 74]. Thus, each track can have four different states:

1. **Confirmed**: In at least M out of N frames *a measurement* has been assigned to a track, and hence it can be confirmed that the track exists.
2. **Deleted**: In at least M out of N frames *no measurement* has been assigned to a track, and hence it can be confirmed that the track does not exist anymore.
3. **Tentative to confirm**: Less than M but more than zero out of N frames *a measurement* has been assigned to a track, and hence it can *tentatively* be confirmed that the track exists.
4. **Tentative to delete**: Less than M but more than zero out of N frames *no measurement* has been assigned to a track, and hence it can *tentatively* be confirmed that the track does not exist anymore.

In case of a false alarm that is not associated with a certain track, a track with the state 'Tentative to confirm' will be initialized. The probability that a false alarm occurs in the next frame within the gate of the predicted state of the false alarm is so small, that it is likely that the track state will change to 'Tentative to delete', and subsequently to 'Deleted'. A similar sequence occurs for a missed detection, where the state of a confirmed track will be changed to 'Tentative to delete', subsequently to 'Tentative to confirm', and finally back to 'Confirmed'.

Furthermore, in the frequently occurring scenario that $N_i \neq N_j$, measurements could be unassigned, and/or tracks could be unassociated. Another scenario exists where $N_i = N_j$, but one or measurements are not within any gate, and thus one or more tracks have no measurement candidates to be associated with. In these scenarios, a new track will be initialized with the state 'Tentative to confirm' or the track's state will be changed to 'Tentative to delete'.

Sequential Probability Ratio Test This second method, also known as the Sequential Likelihood Ratio Test (SLRT), is based on using (log-)likelihood ratio test (LRT, see Eq. (3.1) on page 24) as a track score function. This track score is updated sequentially at successive scans with positive gain in case the track is associated with a measurement, and with negative gain in case that no

measurement is assigned to the track. This gain can be a function of the prediction error and its covariance matrix (i.e., Mahalanobis distance), the expected density of false alarms (often uniform distributed), the expected probability of detection $\hat{P}_D$ and/or the measured SNR.

At each scan, this track score is compared to an upper threshold in order to confirm the track, and to a lower threshold to delete the track. All positive and negative score functions in between these thresholds will give the track the state 'Tentative to confirm' or 'Tentative to delete', respectively. Often an upper limit to the track score is given, to detect the disappearance of a track more easily [51, 73]. The threshold values are determined by the desired probability of false alarms P_{FA} and probability of missed detections P_M [75]. The values of these parameters are often defined by tuning, a process to adjust the parameters to achieve the desired characteristics.

Comparison The main disadvantage of the SPRT-method is that it requires extensive tuning of a lot of parameters, such as the expected $\hat{P}_D$, the desired P_{FA} and P_M, in order to determine the upper and lower thresholds. Moreover, the upper limit of the track score needs to be determined by the user as well. Working with real-world data introduces the limitation to fully comparing the estimated tracks with the true tracks, besides the assumptions of realistic dynamics of a vehicle on a highway. Besides, the M/N logic test will introduce a cleaner separation between the state update (i.e., filtering and prediction) process and the track management, resulting in a more modular data processing chain. Therefore, the M/N logic test is selected for the implementation of the track management element of this tracking algorithm. For simplicity reasons, it is chosen to apply both $M = 2$ and $N = 2$, such that new tracks are initialized easily and disappeared tracks are deleted quickly, while still being able to handle false alarms and missed detections. Moreover, this approach has been extended so that already confirmed tracks are associated with available measurements before other existing tracks. In a very dense environment, this will result in longer maintaining tracks to be confirmed.

3.4.8. Simulation of multi-target tracking algorithm

A multi-target tracking algorithm that can be used to track vehicles in the range-Doppler domain has been proposed. To test our approaches, verify our assumptions, and validate the implementation of this algorithm, a simulation of the range-Doppler data is needed. Therefore, a set of binary detection maps for N_k time frames is synthesized, which will function as input of the tracking algorithm. In this simulation N_T targets are created of which its initial range R_0 and initial velocity v_0 are uniformly distributed over the range 3300 m to 3400 m and over the velocities 60 km/h to 100 km/h and −60 km/h to −100 km/h. Its acceleration is initialized following a normal distribution with zero mean and a standard deviation of 0.1. Each target's true state is updated according to a CA-model, and random white Gaussian noise is added to the target's centroid at each time frame. This will result in a noisy track of a point target in the range-velocity domain. In order to mimic real-world targets, each point target is dilated with a disk-shaped element. The synthesized tracks of $N_T = 20$ targets for $N_k = 30$ time frames (i.e., $T_{sim} \approx 15$ s) are presented in Fig. 3.19, showing the true trajectory and noisy measurements at each time frame of each target T_i, numbered and labeled in red.

The proposed clustering method and tracking algorithm have been implemented in MATLAB. As discussed in the previous sections, the DBSCAN is used for clustering and a multi-target tracking algorithm based on a classical Kalman filter following a CA-model and a statistical hyperellipsoid gating technique has been selected. The GNN-algorithm has been proposed to solve the measurement-to-track association problem, while an MHT-based approach is introduced to handle the Doppler ambiguity. This simulation will be used to analyze the improvements of the algorithm of this MHT with Doppler ambiguity. Approximately 50% of all targets have a folded velocity. The resulted esti-

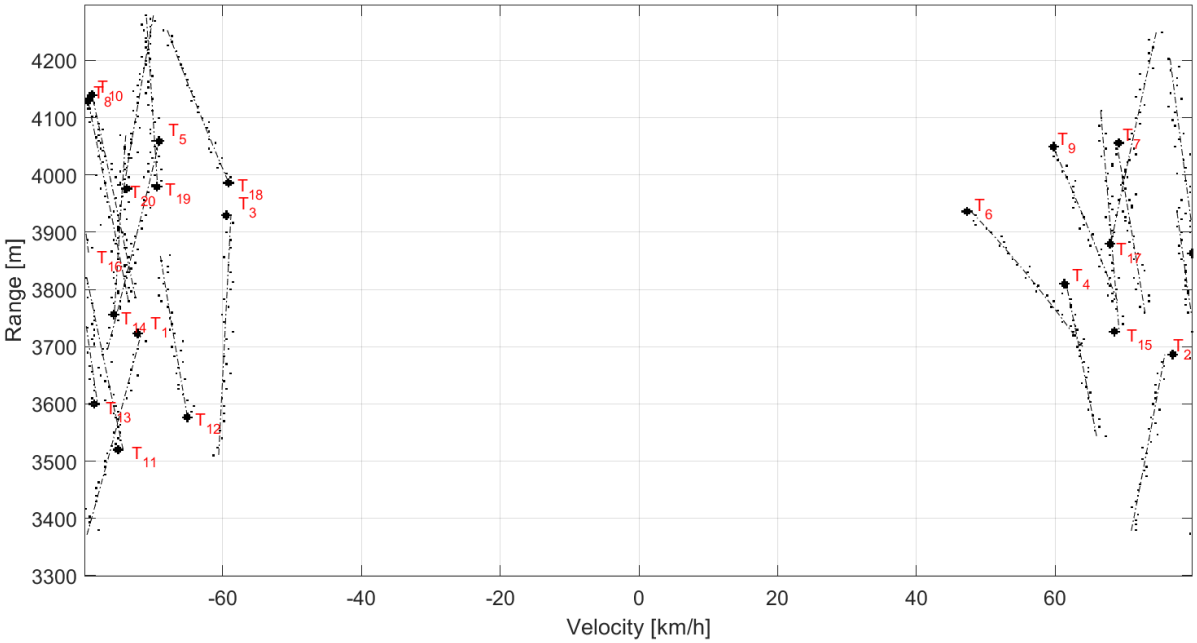

Figure 3.19: Synthesized trajectories and noisy measurements (indicated in black) in the range-velocity domain of $N_T = 20$ targets (each indicated in red) for $T_{sim} \approx 15\,\text{s}$

mated tracks of each target with and without MHT for Doppler ambiguity can be seen in Fig. 3.20a and Fig. 3.20b, respectively. As can be seen in the first simulation, the target's trajectories, indicated in red, show a significantly more accurate estimation of the true track compared to the simulation without handling the Doppler ambiguity. Even in a dense environment, the tracking algorithm is able to cope with closely spaced measurements and tracks crossing each other. In the case without handling the Doppler ambiguity, only tracks without folded velocity, and thus with correct velocity measurements, are estimated accurately. Other tracks suffer from incorrect state prediction and thus no or incorrect measurement association. Therefore, tracks will be deleted quickly by the track management algorithm, and new tracks will be initialized again. Hence the relative small and inaccurate tracks as for example can be seen at targets T_3, T_5 and T_{15}.

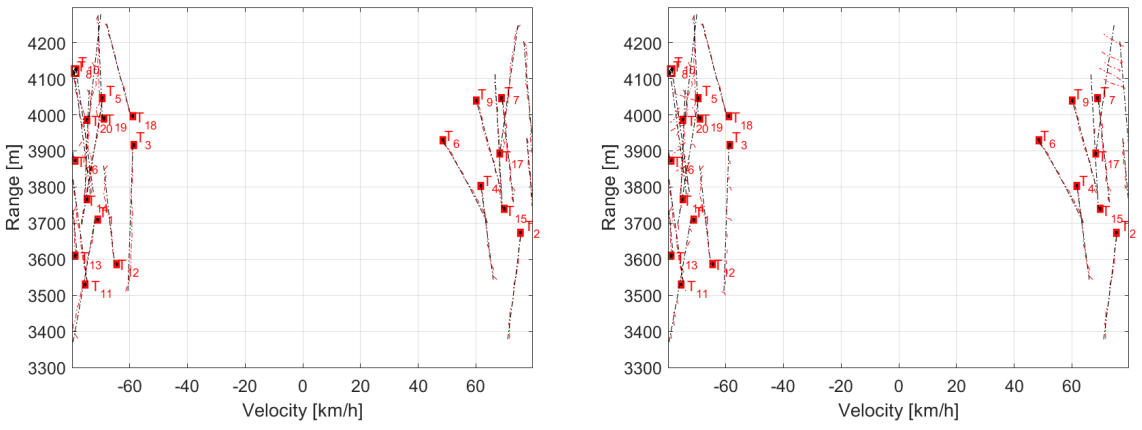

(a) (b)

Figure 3.20: Synthesized trajectories (indicated in black) and its corresponding estimation (indicated in red) as a result of the proposed multi-target tracking algorithm (a) *with* MHT-based approach and (b) *without* MHT-based approach to handle the Doppler ambiguity

To compare the tracking performance with and without MHT that handles the Doppler ambiguity, the state dynamics over time of the estimated track of target T_5 will be analyzed. Note that this target is initialized with an absolute velocity greater than the maximum unambiguous velocity v_r^{max}, and thus its velocity measurements are folded. In Fig. 3.21a the true range and the estimated range in both cases are plotted. It can be seen that the estimated range as a result of the tracking algorithm with MHT almost perfectly follows the true range, whereas the tracking without handling the Doppler ambiguity tends to estimate the target's range smaller than its previous range state. This makes perfect sense since it is assumed that the negative velocity measurement is correct, but is not in line with the target's true state. The same observation can be found by analyzing the Root Mean Square Error (RMSE) of the range estimation, as is shown in Fig. 3.22a. Moreover, Fig. 3.21b shows the velocity estimation in comparison with the target's true velocity, with its corresponding RMSE in Fig. 3.22b. Again, in the case with the MHT, the estimated velocity converges to the true velocity and shows a significant improvement compared to the algorithm without MHT.

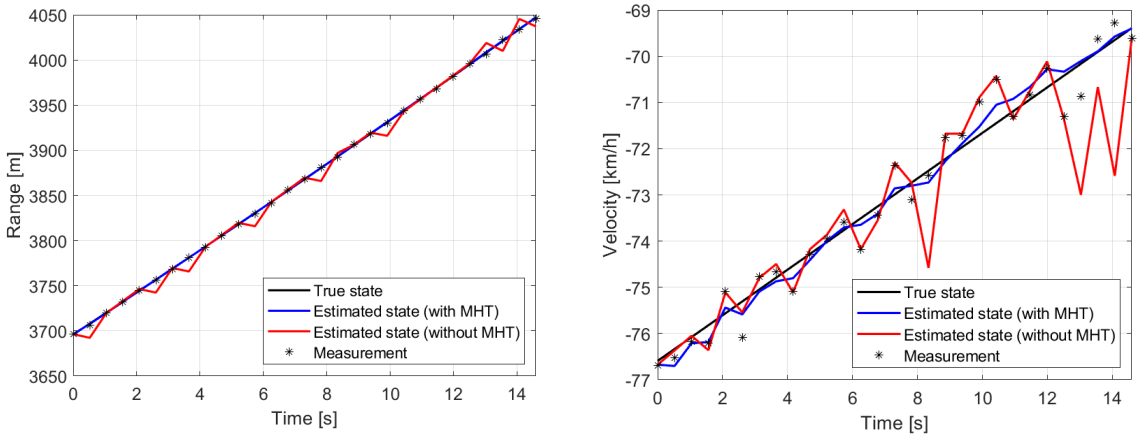

(a) (b)

Figure 3.21: The true and estimated states (with and without MHT for Doppler ambiguity) of target T_5 represented by its (a) range over time and (b) velocity over time

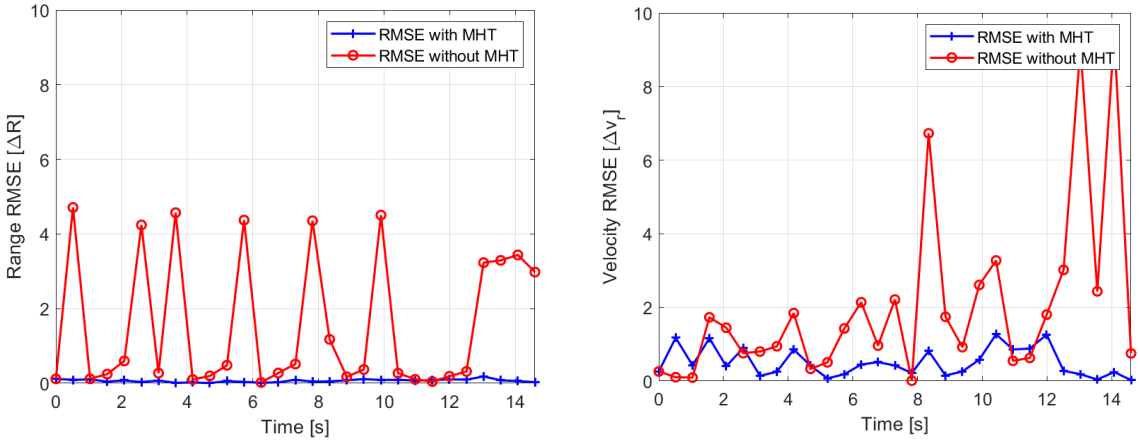

(a) (b)

Figure 3.22: The RMSE of the estimated states (expressed in terms of resolution ΔR and Δv_r) represented by (a) the range RMSE over time and (b) the velocity RMSE over time

3.5. Feature database creation

The goal of this thesis project is to identify target attributes and define sub-classes of automotive targets, which will be achieved by extracting polarization-based features from statistical analysis on radar data while tracking the targets. The latter has been discussed in previous sections. The final step of this method is to create a feature database that can be used for this statistical analysis.

During the tracking of each target, all relevant information will be collected, to be analyzed and exploited later in Chapter 4. For each target, its track, status, the frame number of initialization, the frame number of deletion, and the number of frames in existence will be saved. For each frame in which the target exists, its track information (i.e., estimated range, velocity, and acceleration) and the complex values of the S-matrix of both the cluster centroid bin and all bins within the cluster box will be collected. From these complex values, the amplitude and phase information for all polarization channels can be derived easily.

In Section 1.3 it has been presented that classification of automotive targets is often based on its RCS, which proportionally affects the reflected power of the target and thus the received amplitude. Although that the RCS is strongly dependent on the aspect angle of the radar, in this thesis we are interested in the effect of polarization on the RCS of the targets. Therefore, the amplitude $|S_{H,V}|$ (i.e., $A_{H,V}$) of each target's centroid of all four polarization channels will be considered as an important feature. Note that according to Eq. (2.5) in Section 2.1, the received power, and thus the measured amplitude, is proportional to the range ($P_r \sim R^{-4}$) of the target. Therefore, it would make sense to compensate for the measured amplitude of reflections from targets that are further away. However, applying this compensation to the raw data would also amplify the noise. Thus, only the measured amplitudes of the reflections from the targets will be compensated. Moreover, the target's centroid phase information $\phi_{H,V}$ of all four polarization channels will be collected as well.

Simple transformations applied to the amplitude and phase information can provide more insight into the data, and could potentially result in better features. The initial feature database only contains data in terms of amplitude and phase. Since we are more interested in the polarimetric signatures of the targets, the relative amplitude and phase could be more interesting to analyze. Therefore, the measured S-matrix from Eq. (2.18) can be rewritten as the relative PSM as

$$\mathbf{S} = \begin{bmatrix} |S_{HH}|e^{-j\phi_{HH}} & |S_{VH}|e^{-j\phi_{VH}} \\ |S_{HV}|e^{-j\phi_{HV}} & |S_{VV}|e^{-j\phi_{VV}} \end{bmatrix} = e^{-j\phi_{HH}} \begin{bmatrix} |S_{HH}| & |S_{VH}|e^{-j\phi_x} \\ |S_{HV}|e^{-j\phi_x} & |S_{VV}|e^{-j\phi_y} \end{bmatrix}, \tag{3.27}$$

where $\phi_x = \phi_{HV} - \phi_{HH}$, $\phi_y = \phi_{VV} - \phi_{HH}$ and $S_{HV} \approx S_{VH}$ due to the reciprocal monostatic case. Therefore, it holds that $A_{HV} \approx A_{VH}$ and $\phi_{HV} \approx \phi_{VH}$. Since the absolute phase does not provide any useful information, the complete scattering matrix can be described by only five quantities (i.e., three amplitude parameters and two phase parameters, relative to the HH-polarized phase). In short, the S-matrix can be described by

$$\begin{Bmatrix} S_{HH} \\ S_{HV} \\ S_{VV} \end{Bmatrix}, \quad \begin{Bmatrix} \phi_x \\ \phi_y \end{Bmatrix} \tag{3.28}$$

At last, besides analyzing features based on polarization, the target size and the target dynamics (i.e., mean velocity and acceleration) will also be considered as features. Obviously, a truck will cover more range bins than a small car, and thus this information can be used to distinguish subclasses of automotive vehicles as well. Moreover, the dynamics can provide more information about the target itself and its orientation with respect to the radar.

3.6. Conclusion

To create a feature database of the vehicles, one must be able to detect and track the targets. Therefore, a detection algorithm and a multi-target tracking (MTT) algorithm in the range-Doppler domain is proposed. To improve the performance of these algorithms, full polarimetric information is exploited by a polarimetric data fusion algorithm. Moreover, to simplify the tracking algorithm, clustering is applied so that each cluster represents a single target measurement. An overview of this signal- and data processing chain is presented in Fig. 3.23 (see Appendix C for enlarged version). The signal processing chain, covering the pre-processing, the HPF and the 2D-FFT, has already been presented in Chapter 2.

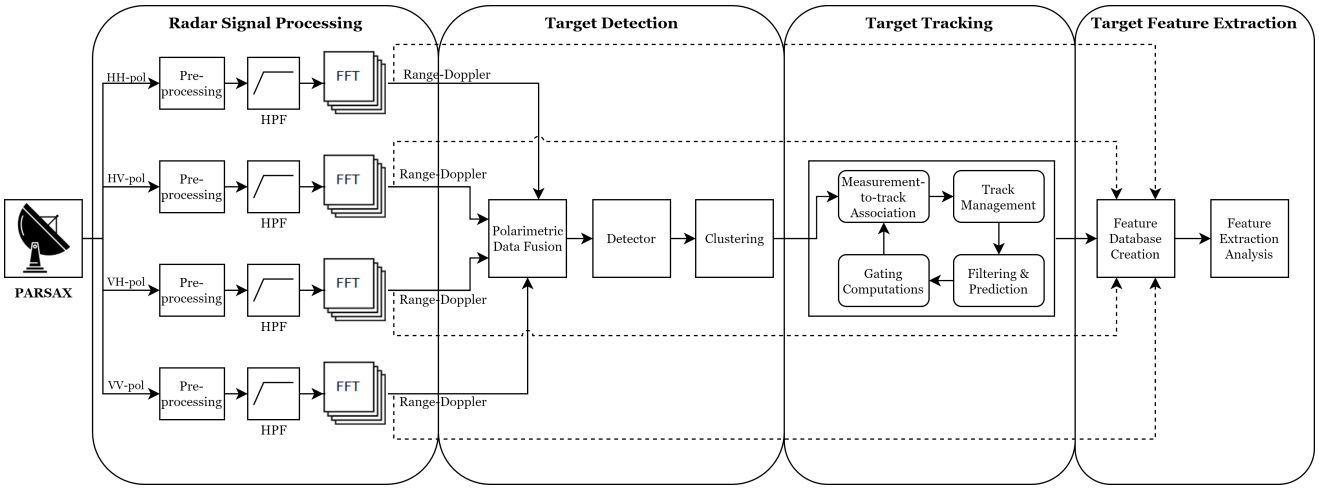

Figure 3.23: A complete overview of the proposed signal- and data processing chain

First, a few concepts of basic detection theory, including the Neyman-Pearson criterion, the LRT and the ROC-curve, are introduced. A non-adaptive detector, based on a fixed threshold and a fixed probability of false alarm P_{FA}, is compared with the CA-CFAR-detector, an adaptive detection method that is commonly used in radar applications, which locally estimates the noise level of each range-Doppler bin and compares it with the received power. Extensions of this detector, such as the OS-CFAR, the SOCA-CFAR and the GOCA-CFAR are introduced and compared among each other. Based on the detection performance, analyzed with real-world PARSAX pre-processed radar data, representing a highway with densely spaced targets, the OS-CFAR has been selected for further processing. Input parameters such as the P_{FA}, the number of training cells N_t, the number of guard cells N_g and the rank need to be determined by a tuning process, dependent on the characteristics of the data set. Imperfections and distortions (due to noise, clutter, and other limitations) of the resulted binary detection map are resolved by applying a morphological filter, exploiting the aliasing property of Doppler processing, and discarding detections with low velocity by an additional HPF.

Before detection is applied, to gain full advantage of the additional polarimetric information, polarimetric data fusion and detection decision fusion are explained and compared. Polarimetric data fusion has been selected due to its effectiveness. The PMSD (see Eq. (3.7)) has been proposed to apply on the four range-Doppler maps, corresponding to each element of the PSM.

Subsequently, a clustering algorithm is applied such that a group of detected cells represent a single target, which will simplify the tracking algorithm significantly. Three methods (k-means clustering, DBSCAN and the flood-fill algorithm) are implemented and compared among each other. Although the flood-fill algorithm and the DBSCAN method result almost in identical clusters, the latter one is more suitable for real-world data and, with a correct value for the ϵ-neighborhood, shows the most realistic clustering. Therefore, DBSCAN with $\epsilon = 2$ will be used for further processing.

The next step in the data processing chain is the tracking of multiple targets from frame to frame. The basic elements of this MTT-algorithm, as illustrated in Fig. 3.17 on page 40, are presented in the figure above as well. The centroid of each cluster is considered as a single measurement $\mathbf{z}_k^i$ at time frame k, containing a range R_k^i and velocity v_k^i measurement with noise variance $\sigma_{n,R}^2$ and $\sigma_{n,v}^2$, respectively. A classical Kalman filter is used to update and predict the state of each target, according to a state dynamics model that assumes constant acceleration. In order to associate each measurement to a certain track, a data association algorithm is required, which can be computationally expensive. However, to simplify this process, gating is applied to only consider the measurements that are within a pre-selected distance from the predicted state. A hyperellipsoid gate, which incorporates the statistical Mahalanobis distance d_M (see Eq. (3.18)), has been selected. Although its computational cost is higher than a regular rectangular or spherical gate, it shows a better tracking performance. Subsequently, from the most commonly used data association methods (i.e., the GNN, the JPDA and the MHT), the GNN-method has been selected to match each measurement to a certain track, based on minimizing the total statistical distance (see Eq. (3.20)). All unassigned measurements will initialize a new track, and all tracks that are not associated with a measurement will be deleted. To cope with Doppler ambiguity, resulting in incorrect velocity measurements, an MHT-based approach has been introduced. Assuming that the velocity can only be folded once, two hypotheses are considered for each track. The hypothesis with the highest probability will determine whether the track can consider the velocity measurement to be folded or not. At last, an M/N logic test with both $M = 2$ and $N = 2$ is preferred over SPRT-method to solve the track management problem. A simulation with synthetic binary detection maps shows that this MTT is able to track vehicles in a dense environment, even when Doppler ambiguity is present.

This methodology has been implemented and applied to real-world polarimetric radar data, generated by PARSAX pointed towards a dense highway between The Hague and Rotterdam (A13). The results of applying the detection method, the polarimetric fusion, and the clustering algorithm to this radar data has been presented and discussed. Subsequently, the proposed MTT algorithm has been executed. When visually inspecting Fig. 3.24, illustrating the track results after 20 time frames, the vehicles are being detected and tracked as expected.

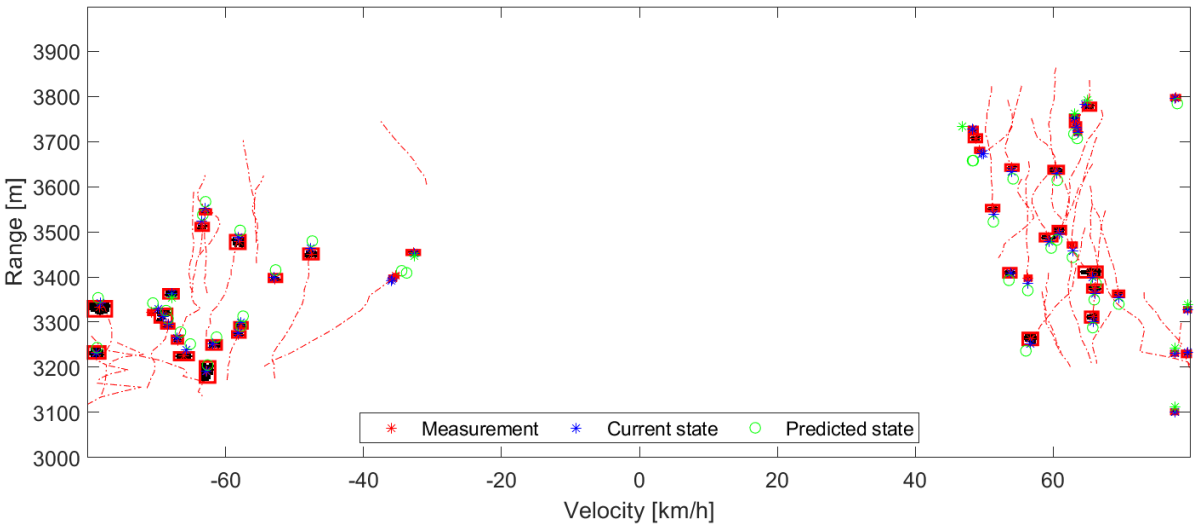

Figure 3.24: Estimated trajectories in range-velocity domain of vehicles on a highway after 20 time frames

Finally, while tracking each target, the amplitude and phase information of all four polarization range-Doppler maps, cluster information, target size, and target dynamics will be collected. This will form the basis of the target feature database.

4

Results of Feature Extraction

The goal of this thesis is to find target attributes and define sub-classes of automotive targets based on polarimetric radar data. These attributes, also known as features, need to be discriminative and non-redundant, meaning that the features can be used to distinguish different classes easily, while still adding information to the classifier. To extract features that describe the polarimetric signature of these classes, a statistical feature analysis will be performed. Therefore, the feature database, that has been created by collecting information of many automotive vehicles during tracking of these vehicles, will be examined. The methodology of target detection, target tracking, and creation of this feature database is explained in the previous chapter. In this chapter, feature extraction from this database will be discussed. First, an introduction to unsupervised machine learning will be presented. Subsequently, an initial analysis of the feature database will be performed. In order to extract more useful features for target classification, the feature database will be extended by more advanced polarization decomposition. At last, the results of the feature extraction will be given.

4.1. Introduction to unsupervised learning approaches

Unsupervised learning can be thought of as self-learning where the algorithm can find previously unknown patterns in a data set that does not have any sort of labels. These patterns can be used to discover attributes that can be useful for classification purposes. In comparison with supervised machine learning, where the system learns itself by guiding from a labeled data set, the output of unsupervised machine learning techniques has to be understood by the user and needs to be mapped with corresponding labels. Also, the output may not be what the user was expecting due to a data interpretation mismatch. Since the given data does not provide labels, only unsupervised machine learning techniques are relevant. In this case, without available labels, it is much harder to verify the correctness of the clusters, and hence it is not possible to check the results and measure the accuracy of the cluster.

Unsupervised machine learning can be divided into two categories: clustering and association. Clustering is based on finding patterns on unlabeled data by its features (e.g., shape, size, color, etc.), whereas association algorithms tend to find dependencies between data items. In this thesis, we will only focus on clustering, since the goal is to find objects that are similar in some way and dissimilar to other objects, such as other vehicle classes or clutter. This similarity is often expressed by a distance between two data sets in the feature space, such as the cosine distance for data vectors and Euclidean distance for data points. Commonly-used clustering techniques are, for example, k-means clustering and hierarchical clustering. In the first example, each data point belongs to a single cluster only, with a total of k clusters defined a priori. By adding the closest

data point to each cluster, chosen similarity distance cost function will be minimized. The latter approach, hierarchical clustering, is entirely different, where each data point starts a single cluster. Step-by-step closely spaced clusters are merged until a pre-defined minimum similarity distance is reached. This method is also known as agglomerative clustering [76]. Another clustering technique commonly used in radar applications is the DBSCAN, which forms clusters of points that are within a maximum pre-defined similarity distance from each other, as explained earlier in Section 3.3 [68].

The main disadvantage of these clustering techniques is that it does not provide any information about the classes that are related to the clusters. The physical interpretation of the clusters needs to be analyzed to define the attributes of the data points (i.e., the moving automotive vehicles) that can be used for classification. Besides, these clustering techniques are not computationally efficient when dealing with a large number of dimensions and/or large data sets. Hence, only two of three features can be interpreted per analysis. Also, the correct similarity distance needs to be selected, which is not always that straightforward [76].

Clustering is only the first step of the process of unsupervised classification purposes. In Fig. 4.1 the basic elements of this process are presented, showing that after clustering each data points (i.e., each target) needs to be labeled, such that useful features can be extracted from the data. Labeling can be performed such that each cluster represents class 1, class 2, class 3, etc., or by analyzing its physical interpretation, sub-classes could be defined in this stage already. In the latter case, human expertise is required for labeling. Subsequently, the selected features need to be analyzed by a classifier using labeled training data [77]. Examples of commonly-used classifiers are a k-NN classifier, a Convolutional Neural Network (CNN) [42], a Support Vector Machine (SVM) [78] and a random forest classifier. The classifier will fit its model parameters according to this feature set, after which the performance of the selected features and the classifier will be tested using testing data. Since labeled data is not available, this latter part will not be discussed any further [77].

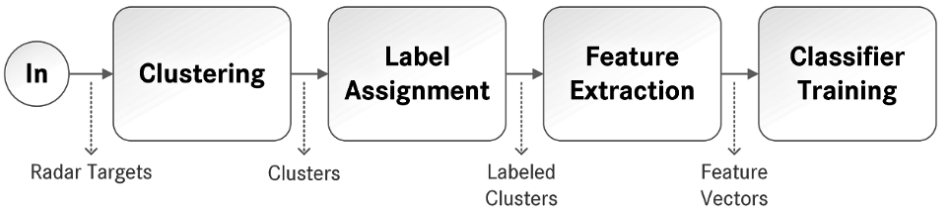

Figure 4.1: A diagram representing the basic elements of unsupervised learning in order to train a classifier [77]

Another important unsupervised learning task is dimensionality reduction, which decreases the size of the input data set by an algorithm to be able to analyze and visualize large data sets. This additional step is often required to reduce the complexity and improve the robustness of the classification process. Moreover, with fewer features, it is easier to interpret the data, allowing extraction of physical information and knowledge about the targets. Besides *feature selection*, where non-interesting features are discarded, *feature extraction* is used to find a new feature set to describe the complete data set. The most simple method for feature extraction is by finding well-defined clusters in an N-dimensional feature space. However, a more advanced and widely used unsupervised feature extraction method is the Principal Component Analysis (PCA), where the data points are projected along the direction of the increasing variance. The directions with the maximum variance are known as the principal components. Whereas PCA maximizes the variance of the data, while minimizing the information loss, Independent Component Analysis (ICA) aims to isolate independent data sources in order to keep the most important components. These two more advanced feature extraction methods will not be discussed any further in this thesis.

4.2. Analysis of target feature database

In Section 3.5 the creation of the initial target feature database is presented. This database mainly consists of amplitude and phase information of all bins representing a target with a minimum existence of 25 time frames, for all four polarization channels. The target amplitudes will be normalized by its measured range, according to Eq. (2.8) in Section 2.1 (see App. D.1). Moreover, this database includes information about the target size and the target dynamics. In this section, the collected data in the target feature database will be analyzed.

4.2.1. Analysis of amplitude information

Firstly, it needs to be confirmed whether the feature database makes sense. Therefore, some basic physical interpretations of the PSM can be exploited by plotting the target reflection amplitudes of each channel. From Section 2.2 it is known that HH-polarized signals should have a positive correlation to VV-polarized signals, and that in reciprocal monostatic case $S_{HV} = S_{VV}$. The latter is only completely valid in a noiseless system, which is not the case. To verify whether our data is in agreement with these physical phenomena, the maximum amplitude of the target box averaged over time of each channel is used as a feature, with $N_{targets}$ samples per feature. These features related to $|S_{HH}|$ and $|S_{VV}|$ are plotted against each other, similarly $|S_{HV}|$ and $|S_{VH}|$, in Fig. 4.2. Similar results have been found when using the average amplitude of the target's centroid as features.

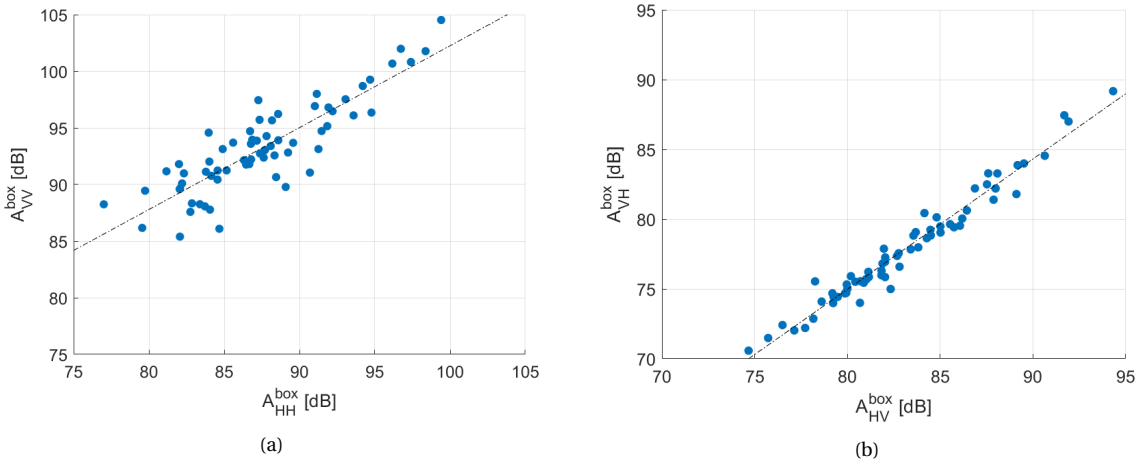

Figure 4.2: Feature spaces, where each data point represents a single target, with the maximum amplitude of the target box averaged over time of polarimetric channels (a) $|S_{HH}|$ vs. $|S_{VV}|$ and (b) $|S_{HV}|$ vs. $|S_{VH}|$

It can be seen that the amplitudes of the co-polarized channels are clearly related to each other and that the amplitudes of the cross-polarized channels are even more correlated to each other. Since the PARSAX radar is monostatic, it makes perfect sense that that $S_{HV} \approx S_{VH}$, with a small offset of approx. 5 dB. This offset is due to PARSAX not being fully calibrated before performing these measurements. Furthermore, the amplitudes of the co-polarized channels are in general higher than the cross-polarized channels, which is in line with the findings of Schipper et al. [32] (see Section 1.3). However, whereas Schipper et al. found that horizontally polarized reflections are greater than vertically polarized reflections of two-wheeled vehicles measured within a distance of 30 m, these figures show the opposite. The reflection amplitudes, representing all different vehicles that are present on a highway, from the VV-channel are larger than the amplitudes of the HH-channel.

Similar feature spaces can be plotted when combining features of co-polarized and cross-polarized channels among each other, such as $|S_{HH}|$ against $|S_{HV}|$ and $|S_{VV}|$ against $|S_{HV}|$. The resulted feature spaces can be found in Fig. 4.3. When analyzing these feature spaces, it can be seen that a

relation between the co-polarized channel and cross-polarized channel is present, but they are not significantly correlated.

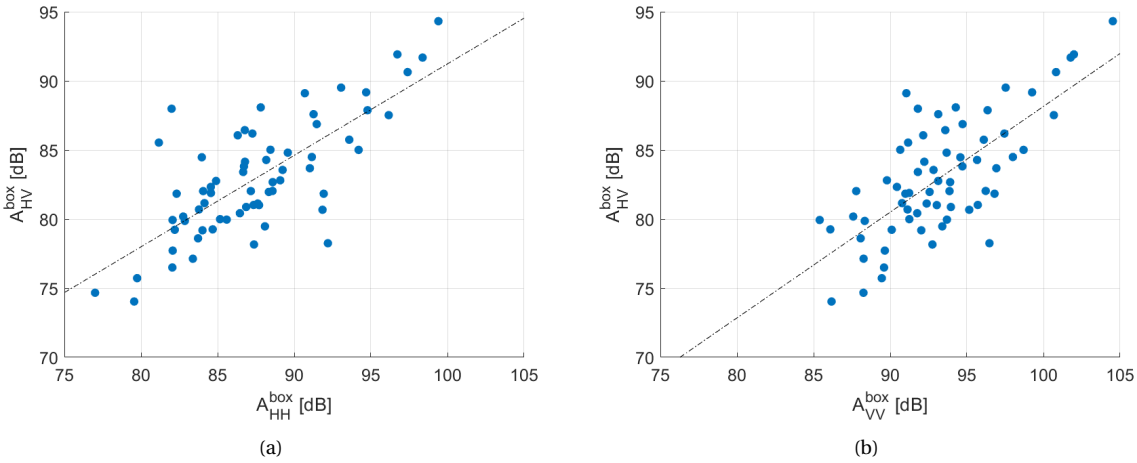

Figure 4.3: Feature spaces, where each data point represents a single target, with the maximum amplitude of the target box averaged over time of polarimetric channels (a) $|S_{HH}|$ vs. $|S_{HV}|$ and (b) $|S_{VV}|$ vs. $|S_{HV}|$

4.2.2. Analysis of correlation between polarization channels

As expected, a strong relationship between the polarization amplitudes has been seen, but no useful features can be extracted from this. However, there might be a correlation between the feature spaces among each other. For example, some targets may have a high correlation between co-polarized channels and cross-polarized channels, whereas other targets may have a high correlation between co-polarized channels, but a low correlation between cross-polarized channels.

In order to analyze targets with such characteristics, the maximum amplitude of the target box of all channels is used as a feature, so that the data points represent each measurement at all time frames of a single target. A few examples of these feature spaces can be seen in Fig. 4.4, 4.5 and 4.6. Since $S_{HV} \approx S_{VH}$, only the maximum amplitudes $|S_{HH}|$, $|S_{VV}|$ and $|S_{HV}|$ are plotted against each other. Again, similar results have been found when using the amplitude of the target's centroid instead of the maximum amplitude of the target box.

The correlation coefficient $\rho(x, y)$ between two polarization channels can physically be interpreted as the amplitude fluctuation of the channels relative to each other. A correlation coefficient close to 1 corresponds to a constant fluctuation difference, equivalent to a synchronous time-behavior of the amplitude of the channels, whereas a low correlation coefficient results in random relative amplitude fluctuation with respect to the polarization channels. This coefficient can be used to characterize the target scattering. For example, as can be seen, the feature spaces of Fig. 4.4 show that target 48 has a high correlation between both co-polarized and co-polarized against cross-polarized channels. On the contrary, target 8 tends to have only a strong correlation between co-polarized channels, while co-polarized against cross-polarized channels show a low correlation coefficient in Fig. 4.5. At last, target 33 can be characterized by having a low correlation coefficient for all three feature spaces, even a negative trend for $|S_{VV}|$ against $|S_{HV}|$. These findings are in line with previous work in [67]. As a result, three new features, in terms of these correlation coefficients, can be included in the feature database and can be visualized into new feature spaces, as is shown in Fig. 4.7. Here the correlation coefficient between the co- and cross-polarized channels are computed for each target and are plotted against each other. In these feature spaces, it can be seen that the correlation coefficients are almost uniformly distributed between 0 and 1, meaning that there is always a positive correlation between the channels, which makes total sense.

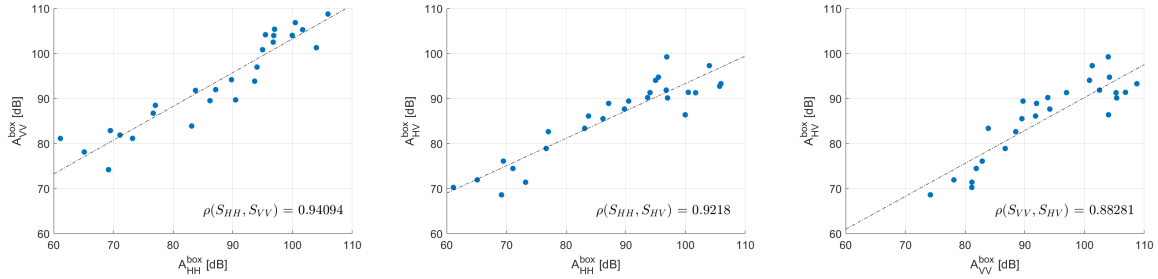

(a) $|S_{HH}|$ vs. $|S_{VV}|$ (b) $|S_{HH}|$ vs. $|S_{HV}|$ (c) $|S_{VV}|$ vs. $|S_{HV}|$

Figure 4.4: Feature spaces with the maximum amplitude of a single target that shows *high* correlation between all polarization channels

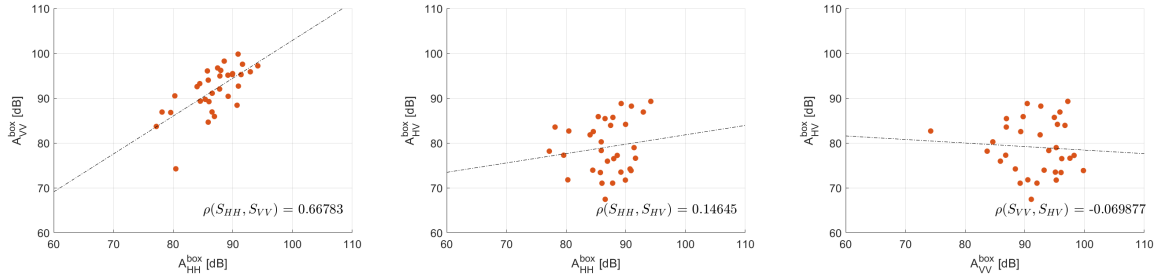

(a) $|S_{HH}|$ vs. $|S_{VV}|$ (b) $|S_{HH}|$ vs. $|S_{HV}|$ (c) $|S_{VV}|$ vs. $|S_{HV}|$

Figure 4.5: Feature spaces with the maximum amplitude of a single target that shows only *high* correlation between co-polarized channels, but *low* correlation between cross-polarized channels

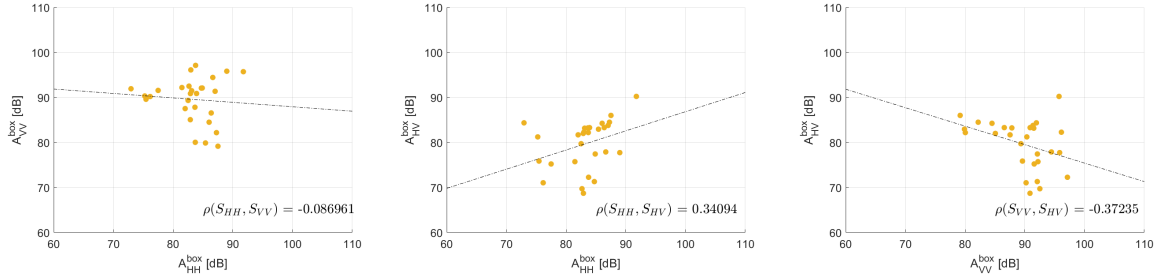

(a) $|S_{HH}|$ vs. $|S_{VV}|$ (b) $|S_{HH}|$ vs. $|S_{HV}|$ (c) $|S_{VV}|$ vs. $|S_{HV}|$

Figure 4.6: Feature spaces with the maximum amplitude of a single target that shows *low* correlation between all polarization channels

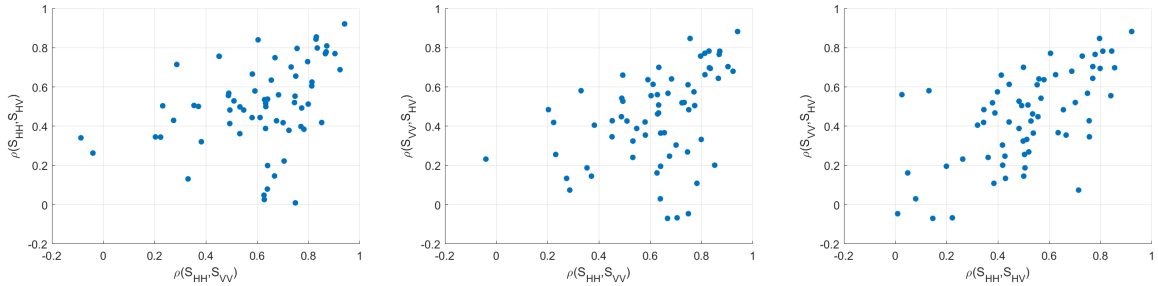

(a) $\rho(S_{HH}, S_{VV})$ vs. $\rho(S_{HH}, S_{HV})$ (b) $\rho(S_{HH}, S_{VV})$ vs. $\rho(S_{VV}, S_{HV})$ (c) $\rho(S_{HH}, S_{HV})$ vs. $\rho(S_{VV}, S_{HV})$

Figure 4.7: Feature spaces with the correlation coefficients between the maximum amplitudes of all polarization channels of all targets

4.2.3. Analysis of target length

As discussed in Section 3.5, besides amplitude and phase information, the target length has been saved as well. Here the target length is the number of range bins of the target box, multiplied by the actual range resolution ΔR. Due to range migration within the sweep time, the target length is larger than the actual size of the vehicle. Nevertheless, this 'stretching' is similar for each target. Therefore, it is still interesting to analyze the mean target length. This feature is plotted against the maximum amplitude of the target box, averaged over time, of the HH- and VV-channel, respectively, in Fig. 4.8. As can be expected, larger targets tend to have greater reflected amplitudes.

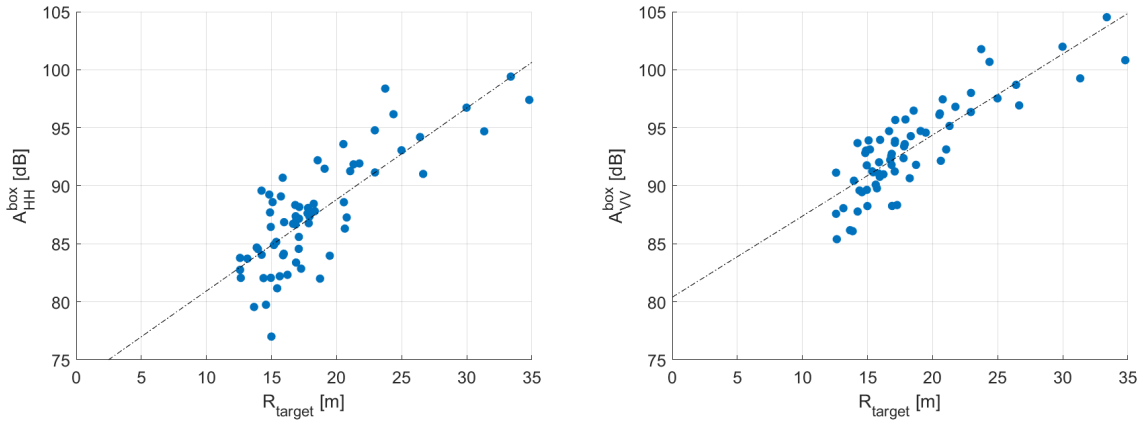

(a) (b)

Figure 4.8: Feature spaces, where each data point represents a single target, with the maximum amplitude of the target box averaged over time of polarimetric channels (a) S_{HH} and (b) S_{VV} against the target length

4.2.4. Analysis of target dynamics

The target dynamics are also included in the feature database, represented by the mean velocity and mean acceleration of each target. These target dynamics are plotted against the maximum amplitude of the target box averaged over time, as shown in Fig. 4.9. As can be seen, the target box amplitude is not affected by the sign of the velocity. Moreover, the mean acceleration is normally distributed around 0. Therefore, the target dynamics do not provide useful information yet. These target dynamics might be interesting features when analyzing with other features, which will be discussed in Section 4.4.

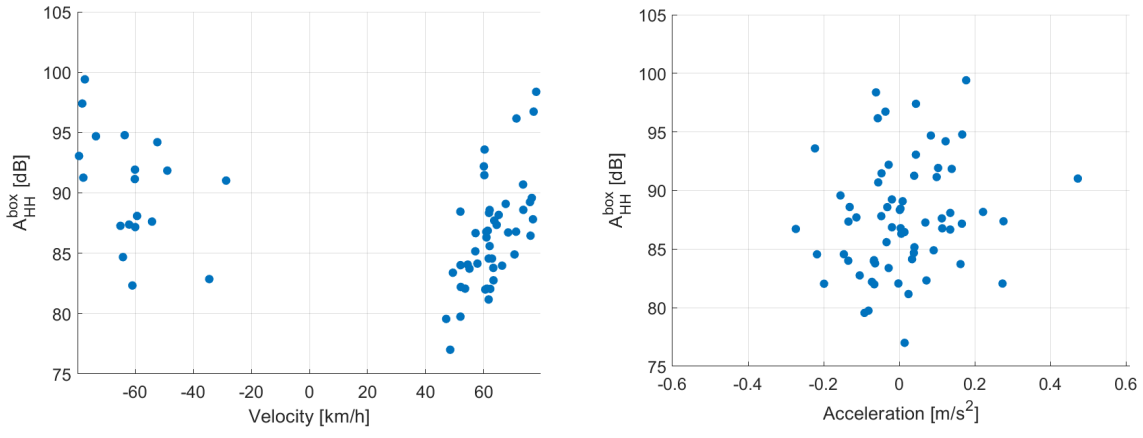

(a) (b)

Figure 4.9: Feature spaces, where each data point represents a single target, with the maximum amplitude of the target box averaged over time of polarimetric channel S_{HH} against (a) the mean velocity and (b) the mean acceleration

4.3. Feature database extension by polarimetric decomposition

In the previous section, the initial feature database has been analyzed. In order to find the physical meaning of the resulted feature spaces and to find more features that could be useful for target classification, the feature database will be extended by performing polarimetric decomposition techniques. These decomposition techniques can provide more information and better insight into the physical meaning of the scattering of the moving vehicles.

The four components of the PSM, described as the S-matrix in both Eq. (2.18) and Eq. (2.21) on page 16, can be decomposed for an easier physical interpretation [79]. These decomposition mechanisms provide new parameters that can contribute to a higher correlation with different classes of the vehicles, and therefore can improve the feature quality. A few examples of these polarimetric decomposition techniques are described below. Also, combinations of these parameters of these decomposition techniques, such as the Cameron decomposition and the polar decomposition, exist [8, 80], but are not discussed any further, since these are not feasible for our given data.

4.3.1. Huynen decomposition

The phenomenological Huynen decomposition describes the target scattering with nine 'Huynen parameters' related to geometrical and physical interpretation (e.g., orientation, position, shape, etc.). The key concept of this decomposition theorem is separating a single average target from the incoming data. To characterize the target scattering, the Pauli scattering vector $\vec{k}_P$ is introduced as

$$\vec{k}_P = \frac{1}{\sqrt{2}}\begin{bmatrix} S_{HH}+S_{VV} & S_{HH}+S_{VV} & S_{HV}+S_{VH} & j(S_{HV}-S_{VH}) \end{bmatrix}^T, \tag{4.1}$$

where $[\cdot]^T$ denotes a transpose operation. In the monostatic back-scattering case, the reciprocity rule applies (i.e., $S_{HV} = S_{VH}$), and therefore the last parameter will be 0. From this three-dimensional vector, the so-called statistic coherence matrix **T** is constructed based on the statistical average of all the scattering information, defined by

$$\mathbf{T} = \langle \vec{k}_P \cdot \vec{k}_P^H \rangle = \begin{bmatrix} 2A_0 & C-jD & H+jG \\ C+jD & B_0+B & E+jF \\ H-jG & E-jF & B_0-B \end{bmatrix}, \tag{4.2}$$

where $[\cdot]^H$ denotes the conjugate transpose operation. Important to note is that the three target structure generators are on the diagonal: $2A_0$, B_0+B and B_0-B, representing target symmetry, target irregularity, and target non-symmetry, respectively [16, 79]. Other properties of this coherence matrix and relationships between these Huynen parameters and decomposition can be found in [8], but will not be discussed any further.

4.3.2. H/A/α decomposition

A typical and useful method for effective feature extraction is the eigenvalue decomposition. Besides that the eigenvalue decomposition of the coherence matrix **T** can be used to identify the target scattering mechanism, the eigenvalues and eigenvectors can also be used to describe the scattering polarimetric entropy H, anisotropy A and α angle. Here the polarimetric entropy H is a roll-invariant quantitative measure of randomness in the scattering mechanisms and the anisotropy A, directly related to the Degree of Polarization (DoP), is used to characterize the scattering phenomenon. Moreover, the alpha angle ($0° \leq \alpha \leq 90°$) represents the surface scattering characteristics from isotropic surface scattering to dipole scattering to dielectric dihedral scattering [23, 42]. These parameters can be very useful to characterize the scattering properties and to extract features for

classification [8, 81]. To compute these parameters, the coherence matrix **T** is decomposed as

$$\mathbf{T} = \mathbf{U}\Lambda\mathbf{U}^H = \mathbf{U}\begin{bmatrix}\lambda_1 & 0 & 0\\ 0 & \lambda_2 & 0\\ 0 & 0 & \lambda_3\end{bmatrix}\mathbf{U}^H, \tag{4.3}$$

where **U** is an unitary matrix containing three orthogonal eigenvectors $\mathbf{u}_i$ and Λ is a 3×3 diagonal matrix with non-negative real eigenvalues ($\lambda_1 \geq \lambda_2 \geq \lambda_3 \geq 0$). If all eigenvalues λ_i are zero, except for λ_1, then the coherency matrix **T** represents a single scattering matrix, corresponding to a pure correlated and completely polarized scattering mechanism. On the other hand, if all eigenvalues are identical, then **T** corresponds to a completely unpolarized, random scattering process [8]. To define the polarimetric entropy H and alpha angla α, the pseudo-probabilities P_i needs to be obtained from the eigenvalues λ_i ($i = 1,2,3$) as follows:

$$P_i = \frac{\lambda_i}{\sum_{j=1}^{3}\lambda_j} \tag{4.4}$$

The $H/A/\alpha$-decomposition is then defined by

$$H = -\sum_{i=1}^{3} P_i \log_3(P_i), \qquad A = \frac{\lambda_2-\lambda_3}{\lambda_2+\lambda_3}, \qquad \alpha = \sum_{i=1}^{3} P_i \cos^{-1}(|u_{i,1}|), \tag{4.5}$$

where $u_{i,1}$ is first element on the eigenvector $\mathbf{u}_i$ [23]. These equations show that the polarimetric entropy is $H = 0$ for a completely deterministic and $H = 1$ for a completely random scattering mechanism. A completely deterministic scattering mechanism, meaning that the scattering wave is completely polarized, results in a degree of polarization of 1. Besides, in this case, it is possible to perfectly decompose the PSM into canonical scattering parts. Correspondingly, completely random scattering (i.e., $H = 1$) leads to a degree of polarization of 0. In the latter case, the process is completely depolarizing and polarimetric information is useless for classification [42].

As mentioned before, these parameters are often used to characterize the scattering behavior, and therefore can be used as features to classify the targets. Since the anisotropy A only becomes an important and useful parameter to describe the scattering process when the entropy H is very high, classification is often performed in the two-dimensional H/α-plane. Here the α angle is used to determine the underlying scattering behavior, such that the H/α-plane can approximately be separated into 9 classes of basic scattering mechanisms, as presented in Fig. 4.10. This figure illustrates a simple schematic overview to classify and describe the scattering mechanism based on typical values of the entropy H and α angle [8, 23].

This $H/A/\alpha$-decomposition has been applied to the four range-Doppler maps, corresponding to the four elements of the PSM. The distribution of the values of H and α of these data sets are shown in Fig. 4.11. As can be seen, all bins in the range-Doppler frame have an entropy close to 0, with α ranging from 20° to 90°. Equivalently, the degree of polarization approaches 1, meaning that the received waves are completely polarized and deterministic. Using a fully polarimetric radar, this is exactly as expected. To get meaningful values for H and α, averaging is required, as already defined by Eq. (4.2). Therefore, instead of using the instant values of the PSM, a statistical average of the scattering information is used to define the coherence matrix **T**.

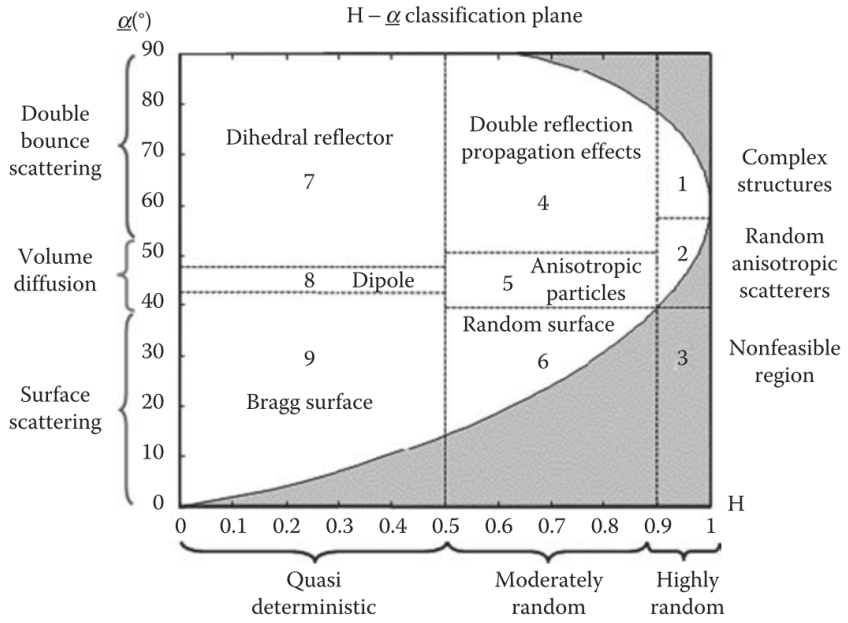

Figure 4.10: Simple classification scheme of the two-dimensional H/α-plane [8]

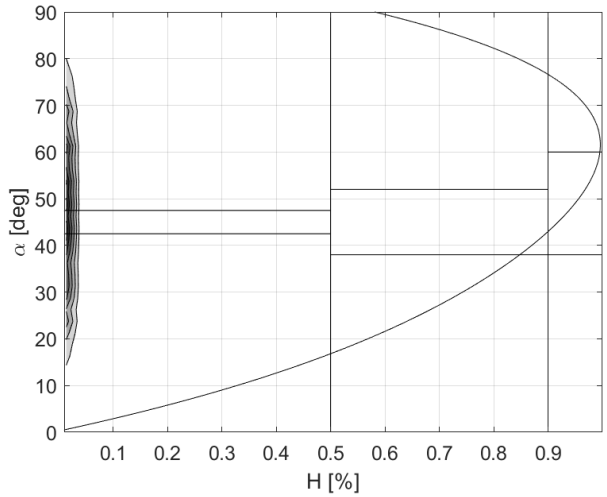

Figure 4.11: Data distribution of a range-Doppler frame in the two-dimensional H/α-plane

At first, the scattering information related to the targets, expressed by the PSM of the target's centroid for each time frame, has been collected and averaged over time, before the $H/A/\alpha$-decomposition has been applied. The resulted distribution in the H/α-plane is shown in Fig. 4.12a. As can be seen, the entropy is distributed in the region $0.3 \leq \overline{H}_{time} \leq 0.8$ and around $\overline{\alpha}_{time} \approx 45°$. According to the classification schematic in Fig. 4.10, this is correlated to volume diffusion and quasi-deterministic/moderately random entropy, corresponding to dipole and anisotropic particle scattering. Since only the centroid is taken into account, this is probably related to the scattering of the main body of a vehicle.

Secondly, averaging of the scattering information over space in the range-Doppler domain has been applied. For each target at each time frame, the average coherence matrix $\mathbf{T}$ of the target's box has been used to compute the entropy H and α angle. In Fig. 4.12b the resulted distribution in the H/α-plane is presented, showing a high concentration in the region at $\overline{H}_{space} \leq 0.3$ and $30° \leq \overline{\alpha}_{space} \leq 70°$. This corresponds to quasi-deterministic entropy with all kinds of scattering mechanisms. Since

the target's box in the range-Doppler domain covers reflections from all parts of the vehicle (i.e., the main body, the wheels, car mirrors, etc.), there is an obvious explanation for this scattering behavior in H/α-plane.

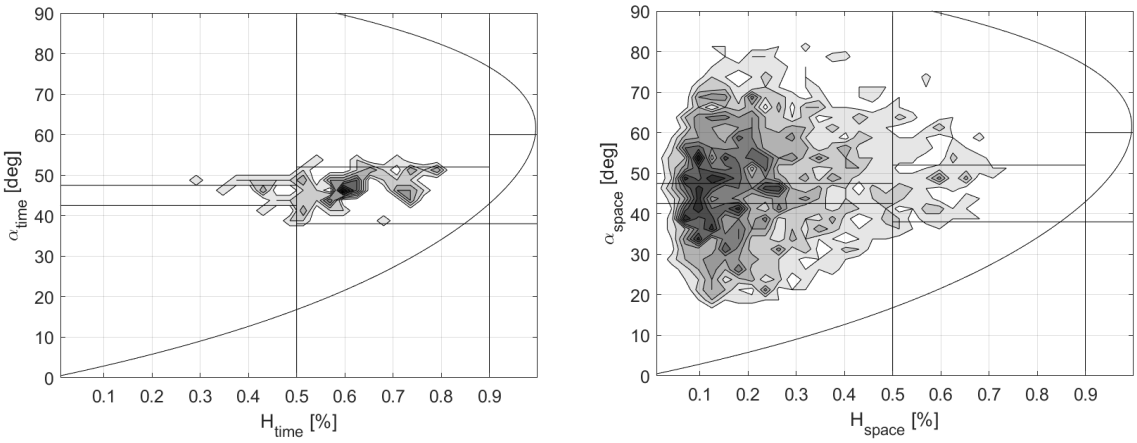

(a) (b)

Figure 4.12: Data distribution of the received signals corresponding to the targets in the two-dimensional H/α-plane, resulted from (a) the target's centroid averaged over time and (b) the target's box amplitude averaged over space

Unfortunately, from these figures, it is not possible to distinguish several classes of targets. All data points are clustered close to each other, meaning that the scattering of all moving vehicles at the highway behave similarly in the H/α-plane. However, these H/α data points can be used as features in combination with other target features for further analysis.

4.3.3. Pauli decomposition

Whereas the $H/A/\alpha$-decomposition requires averaging in either space or time to gain more insight into the physical meaning of the scattering, the Pauli decomposition is a commonly-used coherent decomposition technique. Here coherency refers to a direct decomposition of the PSM into a coherent sum of basis matrices, each weighted by coefficients. The polarimetric Pauli decomposition describes the target scattering matrix with four parameters related to the physical scattering process, based on the properties of the PSM when undergoing a change of the wave polarization base (i.e., a reflection) [8]. This decomposition is based on the coherent sum of the Pauli matrices, a set of four complex unitary and Hermitian matrices, each weighted by the complex coefficients a, b, c, and d. The squared absolute value of these parameters describe a part of the total RCS and are respectively related to a canonical scattering process with an odd number (single) of reflections (scattering from a plane surface), an even number (double) of reflections (diplane scattering), cross-polar scattering (diplane scattering with a relative orientation of 45°) and at last, the total sum of all anti-symmetric components of the PSM, respectively [42]. The S-matrix can be decomposed as

$$\mathbf{S} = \frac{a}{\sqrt{2}}\begin{bmatrix}1 & 0\\ 0 & 1\end{bmatrix} + \frac{b}{\sqrt{2}}\begin{bmatrix}0 & 1\\ 1 & 0\end{bmatrix} + \frac{c}{\sqrt{2}}\begin{bmatrix}0 & -j\\ j & 0\end{bmatrix} + \frac{d}{\sqrt{2}}\begin{bmatrix}1 & 0\\ 0 & -1\end{bmatrix}, \tag{4.6}$$

where the coefficients are as follows:

$$a = \frac{S_{HH}+S_{VV}}{\sqrt{2}},\ b = \frac{S_{HH}-S_{VV}}{\sqrt{2}},\ c = \frac{S_{HV}+S_{VH}}{\sqrt{2}},\ d = j\frac{S_{HV}-S_{VH}}{\sqrt{2}} \tag{4.7}$$

In a monostatic case, the latter component is theoretically zero because of the reciprocity theorem

(i.e., $S_{HV} \approx S_{VH}$), and thus can be omitted ($d = 0$) [8]. Therefore, the three remaining parameters can be visualized as three range-Doppler maps, as can be seen in Fig. 4.13.

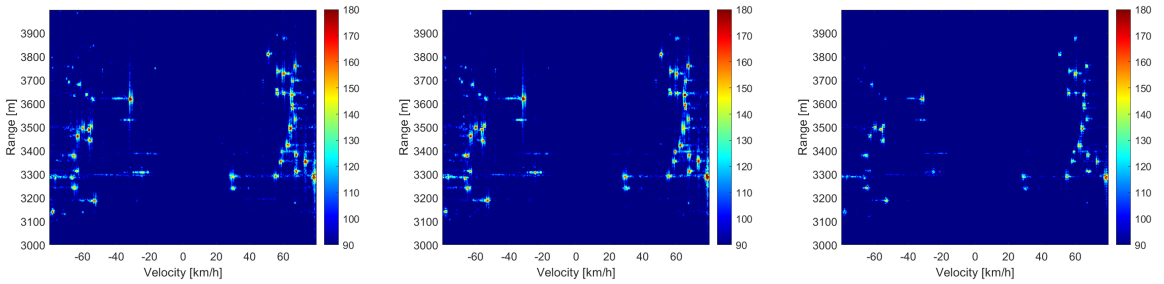

(a) Component $|a|^2$ (b) Component $|b|^2$ (c) Component $|c|^2$

Figure 4.13: A range-Doppler map of moving vehicles on a highway represented by the three Pauli coefficients

These three coefficients are often assigned as a color-coded format (e.g., red-green-blue or cyan-magenta-yellow) to visualize the polarimetric data in a single image. This contains much more information than an image of a single polarimetric element and can be used to clearly distinguish a polarimetric signature of a certain object [42, 82]. This resulted RGB-image is shown in Fig. 4.14.

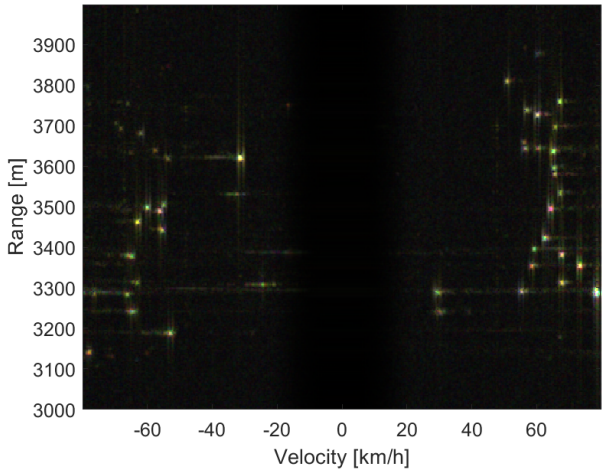

Figure 4.14: An RGB color-coded Pauli decomposed range-Doppler map of moving vehicles on a highway (red: $|a|^2$; green: $|b|^2$; blue: $|c|^2$)

As can be seen, the targets are visible as either red or green clusters or mixed as yellow clusters. The red and green colors represent scattering from a plane surface (odd number of reflections) and a diplane structure (even number of reflections), respectively. These coefficients will be analyzed as potential features that can be used for the classification of moving vehicles.

4.3.4. Krogager decomposition

The Krogager decomposition describes the target scattering as by sphere, diplane, and helix scattering with corresponding weight factors k_S, k_D, and k_H. This directly represents the relation to directly measurable quantities and thus to a physical interpretation [54], similar as can be seen in the Pauli decomposition. The S-matrix is decomposed as follows:

$$\mathbf{S} = k_S \mathbf{S}_{sphere} + e^{j\phi} k_D \mathbf{S}_{diplane}(\theta) + e^{j\phi} k_H \mathbf{S}_{helix}(\theta), \tag{4.8}$$

where ϕ is the absolute phase and θ is again the target orientation angle. Note that the scattering matrices of the three terms differ when applied to linear polarized or circular polarized electromagnetic waves. In the case of linear polarization [54], the Krogager coefficients are given by

$$\begin{aligned} k_S &= \left| \frac{S_{HH} + S_{VV}}{2} \right|, \\ k_D &= \min \left\{ \left| \frac{S_{VV} - S_{HH}}{2} + jS_{HV} \right|, \left| \frac{S_{HH} - S_{VV}}{2} + jS_{HV} \right| \right\}, \\ k_H &= \text{abs} \left\{ \left| \frac{S_{VV} - S_{HH}}{2} + jS_{HV} \right| - \left| \frac{S_{HH} - S_{VV}}{2} + jS_{HV} \right| \right\}, \end{aligned} \tag{4.9}$$

and in case of circular basis with RHC (denoted by R) and LHC (denoted by L) polarization [83]

$$\begin{aligned} k_S &= |S_{RL}|, \\ k_D &= \min \{|S_{LL}|, |S_{RR}|\}, \\ k_H &= \text{abs} \{|S_{LL}| - |S_{RR}|\} \end{aligned} \tag{4.10}$$

These three coefficients are plotted in the range-Doppler spectrum, as can be seen in Fig. 4.15.

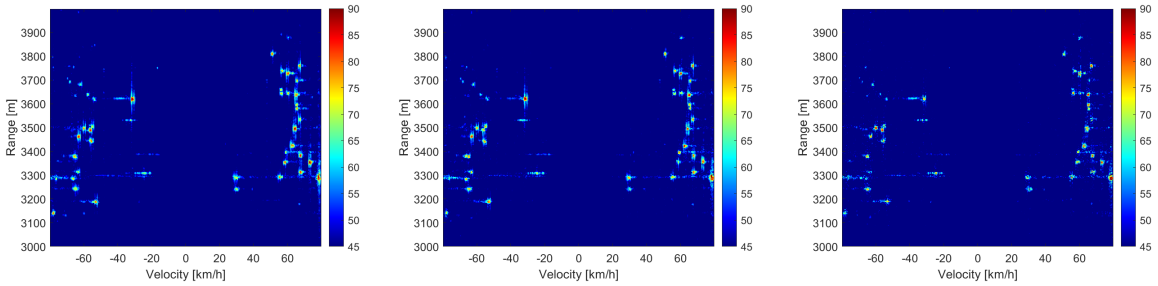

(a) Component k_S (b) Component k_D (c) Component k_H

Figure 4.15: A range-Doppler map of moving vehicles on a highway represented by the three Krogager coefficients

A similar approach as described before can be applied to combine the three weight factors into a color-coded format, to visualize the full S-matrix into a single image (see Fig. 4.16) [8].

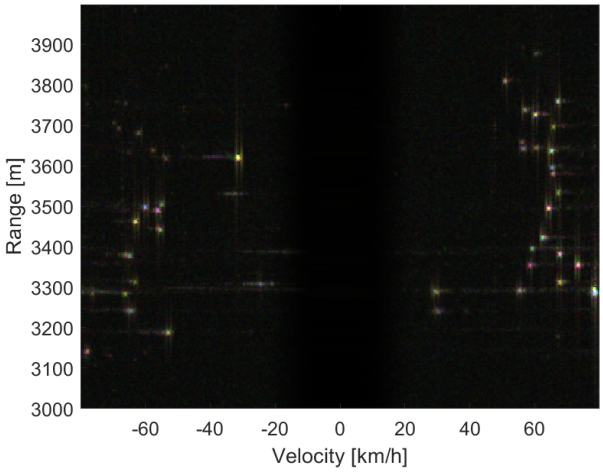

Figure 4.16: An RGB color-coded Krogager decomposed range-Doppler map of moving vehicles on a highway (red: k_S; green: k_D; blue: k_H)

Similar as in Fig. 4.14, most targets are visualized as a red or green cluster, describing dominant sphere scattering and diplane scattering, respectively. Besides, some targets tend to be represented as a blue cluster, meaning dominant helix scattering. Again, these coefficients can be analyzed as potential features for classification.

4.4. Target feature extraction

After analysis of the initial feature database and extending this database with more features utilizing polarimetric decomposition techniques, feature extraction takes place. To find features that can be used to classify moving automotive vehicles, a combination of features needs to be found that are useful to distinguish these classes (i.e., clusters) from each other. The final feature database consists of 25 features, including the amplitude information, target length, target dynamics, correlation coefficients, and polarimetric decomposition coefficients, such as the Pauli coefficients, Krogager coefficients and the $H/A/\alpha$ values, both averaged over time and space. The phase information has been discarded as it does not provide useful information due to the poor calibration of the radar.

4.4.1. Normalization and standardization

Before analysis of these feature pairs and feature extraction can take place, the data in the target feature database needs to be transformed first. This data set includes many types of variables with different units and different value ranges, which can lead to biased results. In order to mitigate this problem, feature re-scaling needs to be applied: either feature normalization or feature standardization is a simple way to ensure that each feature is equally important. Feature normalization re-scales each feature vector to a common range between 0 and 1, whereas feature standardization transforms the feature vector in such a way that the standardized feature vector has a mean of 0 and a standard deviation of 1. For any given feature vector $\mathbf{x}$, the normalized vector $\mathbf{x}_{norm}$ is given by

$$\mathbf{x}_{norm} = \frac{\mathbf{x} - \min\{\mathbf{x}\}}{\max\{\mathbf{x}\} - \min\{\mathbf{x}\}}, \tag{4.11}$$

and the standardized feature vector $\mathbf{x}_{std}$ is computed by

$$\mathbf{x}_{std} = \frac{\mathbf{x} - \mu}{\sigma}, \tag{4.12}$$

where μ and σ are the mean value and standard deviation of $\mathbf{x}$, respectively. For clustering algorithms and clustering analysis methods that use distance measurements, the features need to be unitless, and thus standardization will be applied to the features that are not unitless before further analysis [84].

4.4.2. Clustering tendency

To determine whether the clustering analysis on a certain feature space is feasible and may lead to useful clusters, a manner of cluster evaluation is required. Although that a clustering algorithm can always return clusters for any data set, first it needs to be checked whether the feature space is meaningful and not misleading, which is only the case when there is a non-random structure in the given data set. This is known as clustering tendency: if a feature space does not contain clustering tendency, the resulting clusters may be irrelevant at all. Assessing the clustering tendency is often done by statistical tests. For example, the *Hopkins statistic*, which tests the spatial randomness of a variable by measuring the probability that a given data set D, consisting of N data points, is generated by a uniform data distribution U [85]. The Hopkins statistic H_S is given by

$$H_S = \frac{\sum_{i=1}^{N} y_i}{\sum_{i=1}^{N} x_i + \sum_{i=1}^{N} y_i}, \tag{4.13}$$

where x_i is the distance from each data point $\mathbf{p}_i$ to its nearest neighbor $\mathbf{p}_j$ in D and where y_i is the distance from each point $\mathbf{q}_i$ from U to the nearest data point $\mathbf{q}_j$ from D. Here U is a uniformly data distribution with equal mean and variance statistics as D. This can be described as follows:

$$\begin{cases} x_i = \min\{dist(\mathbf{p}_i, \mathbf{p}_j)\}, & \mathbf{p}_i, \mathbf{p}_j \in D \\ y_i = \min\{dist(\mathbf{q}_i, \mathbf{q}_j)\}, & \mathbf{q}_i \in U, \mathbf{q}_j \in D \end{cases} \tag{4.14}$$

This statistic value H_S can be interpreted by comparing the random distribution of D with the uniform distribution of U. If D were uniformly distributed, it holds that $\sum_{i=1}^{N} x_i \approx \sum_{i=1}^{N} y_i$, and thus $H_S \approx 0.5$. Logically, if clusters are present in D, the Hopkins statistic H_S will increase towards 1, whereas H_S is closer to 0, the data set does not have clustering tendency [84]. However, this statistic is only an indication of clustering tendency. In case of high correlation, the data set is far from uniformly distributed, hence a high value for H_S, but the feature space will not contain any meaningful clusters.

The Hopkins statistic can be computed for each possible feature pair that can be formed from the feature database, consisting of 25 features, results in a 25-by-25 matrix of values for H_S. This matrix, averaged over 50 runs, is visualized in Fig. 4.17. From this matrix, a few remarks can be made. First, the feature pairs on the diagonal represent feature spaces of two equal features. Hence, there is perfect correlation (i.e., $\rho(x,x) = 1$) and therefore the value for H_S is logically close to 1 as well. Secondly, features that are paired with the mean velocity show a high cluster tendency as well. This is obvious, since the mean velocity is either positive or negative, resulting in already two clusters (see Fig. 4.9a). Thirdly, other combinations of features show a high H_S. Often this is due to high correlation again, because of a direct physical relationship with each other. For example, it holds that $S_{HV} \approx S_{VH}$ and that the Pauli and Krogager coefficients are closely related to each other. With these remarks, it can be concluded that further analysis of the feature database is required to find well-defined clusters in feature spaces that are useful for classification.

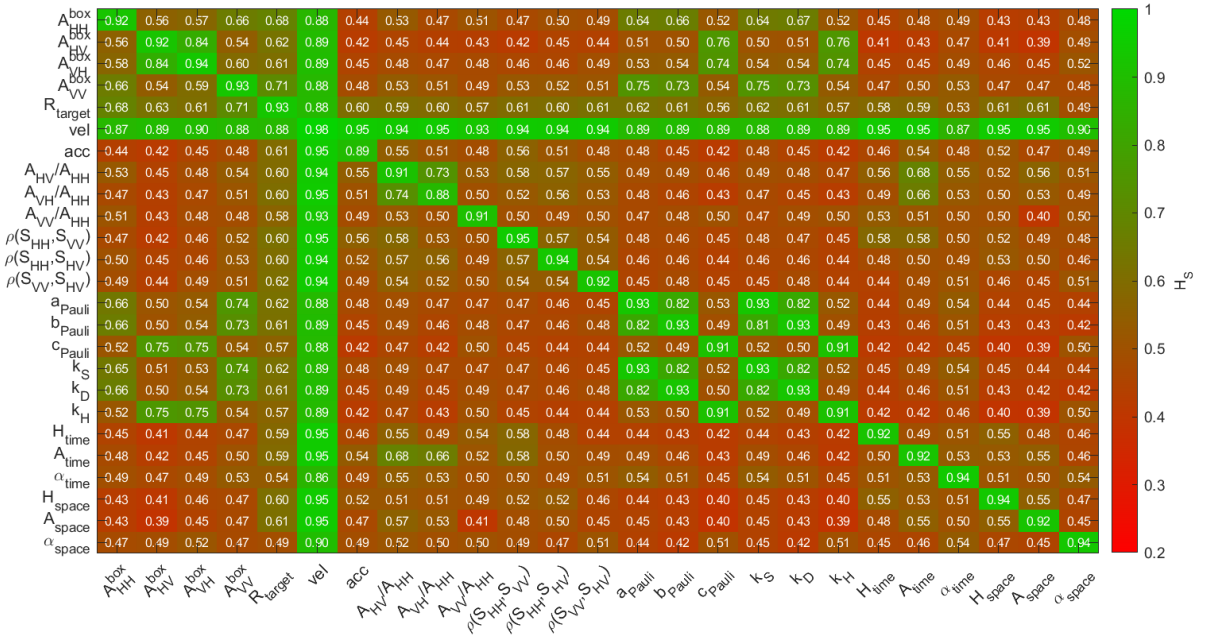

Figure 4.17: Hopkins Statistic matrix indicating H_S for all possible feature pairs

4.4.3. Clustering quality

From the Hopkins statistics matrix, it has been concluded that no feature pair can directly result in useful clusters. Nevertheless, there might be some feature pairs that can have a physical interpretation that may be meaningful and thus useful for classification. For example, as mentioned in Section 4.2.2, the correlation coefficients between the maximum amplitudes of the polarization channels can be used to describe the target's scattering behavior. It has been shown how three different targets behave differently in terms of these correlation coefficients, which are used to form the feature spaces in Fig. 4.18a, 4.18b and 4.18c. Although that the value for H_S of these feature spaces is respectively 0.58, 0.52 and 0.52, these feature spaces can still be exploited by clustering the data points and supporting these clusters with a physical interpretation. Therefore, the k-means clustering method with three clusters (defined a priori) has been applied to these feature spaces, of which the results are presented in Fig. 4.18. From these clustered feature spaces, three classes are defined, corresponding to the targets related to Fig. 4.4, 4.5 and 4.6, which can be described as follows:

Class 1: Targets with high correlation between co-polarized channels (high $\rho(S_{HH}, S_{VV})$) and high correlation between co- and cross-polarized channels (high $\rho(S_{HH}, S_{HV})$ and $\rho(S_{VV}, S_{HV})$)

Class 2: Targets with high correlation between co-polarized channels (high $\rho(S_{HH}, S_{VV})$) and low correlation between co- and cross-polarized channels (low $\rho(S_{HH}, S_{HV})$ and $\rho(S_{VV}, S_{HV})$)

Class 3: Targets with low correlation between co-polarized channels (low $\rho(S_{HH}, S_{VV})$) and low correlation between co- and cross-polarized channels (low $\rho(S_{HH}, S_{HV})$ and $\rho(S_{VV}, S_{HV})$)

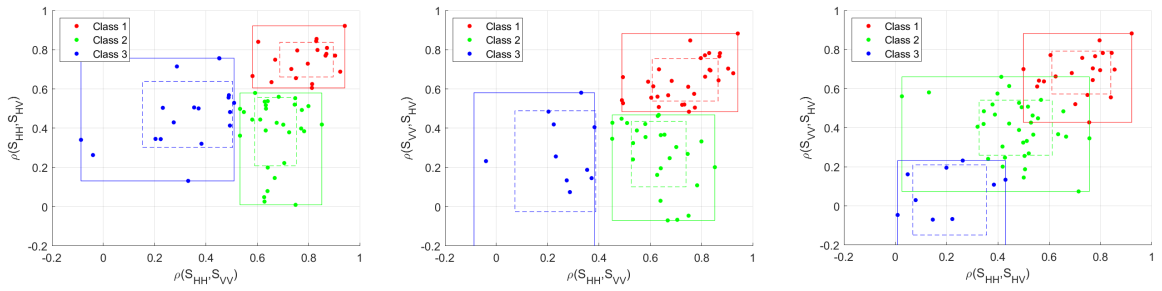

(a) $\rho(S_{HH}, S_{VV})$ vs. $\rho(S_{HH}, S_{HV})$ (b) $\rho(S_{HH}, S_{VV})$ vs. $\rho(S_{VV}, S_{HV})$ (c) $\rho(S_{HH}, S_{HV})$ vs. $\rho(S_{VV}, S_{HV})$

Figure 4.18: Feature spaces with the correlation coefficients between the maximum amplitudes of all polarization channels of all targets, clustered in three classes by k-means method. Here the dashed and solid rectangles indicate the standard deviation and the min-max bounds, respectively, to visualize the cluster separability.

Then, to measure the clustering quality and to compare clusterization of other feature spaces or generated by other input parameters or methods, a quantitative parameter is required. In general, methods to evaluate the quality of the clusterization can be categorized into two groups: extrinsic and intrinsic, corresponding to supervised and unsupervised methods. Whereas extrinsic measure methods assume that the ground truth is available, intrinsic methods examine the clusters based on their separability [84]. Since our target feature database is unlabeled, only intrinsic methods can be utilized. Some examples of intrinsic cluster evaluation methods are:

- **Silhouette coefficient**: this coefficient is composed of two scores for each data point. The first score a_i is the average distance from the data point to all other data points in the cluster to which the data point belongs, whereas the second score b_i is the average distance from the

data point to all data points in the nearest other clusters. Then, together they will form the silhouette coefficient s_i for each data point as follows:

$$s_i = \frac{b_i - a_i}{\max\{a_i, b_i\}}, \tag{4.15}$$

where $-1 \leq s_i \leq 1$. Where the value of a represent the compactness of the cluster, b corresponds to the separability of the cluster with respect to the other clusters. For analysis, the mean of the silhouette coefficient of all data points in each cluster, denoted as s, will be used. It is preferable to have clusters with values for s close to 1, meaning that the cluster is compact and far away from other clusters [84].

- **Calinski-Harabasz index**: This index, also known as the Variance Ratio Criterion, evaluates the data set based on the average sum of the distances from all data points of a certain cluster to the cluster center, and the sum of the distances between all cluster centers. The index is the ratio of these two sums, corresponding to the within-cluster dispersion and the inter-cluster dispersion, and increases when clusters are more dense and well separated from each other [86].

- **Davies-Bouldin index**: This index relates to the similarity between each cluster by comparing the average distance between the cluster centers with the size of the clusters. Here the size of the cluster is defined as the average distance from each point within a certain cluster to its center. Here, the smaller the index value, the better the clustering performance [87].

- **Kullback–Leibler divergence**: A less commonly used measure is the Kullback-Leibler divergence, which is based on the distribution of the data points by incorporating the spatial statistics of the given data set. This allows evaluation clusters in very complex data sets with higher dimensions [88].

Note that we analyzed a database with not too many observed targets (only 66), which means that precise estimation of the data distribution and the use of two-dimensional histograms of feature pairs is not reasonable. Therefore, these cluster evaluation methods only provide an indication of the cluster quality. Moreover, the Kullback-Leibler divergence is based on the data distribution of very complex data sets and thus is not useful for our cluster analysis. Nevertheless, the clusterization from Fig. 4.18 can be assessed by utilizing the other three evaluation measures. The resulted coefficients/indices, averaged over 50 runs, can be found in Table 4.1.

Table 4.1: Metrics to evaluate the clustering quality of the correlation-based feature spaces (see Fig. 4.18)

	Silhouette	**Calinski-Harabasz**	**Davies-Bouldin**
$\boldsymbol{\rho}(\mathbf{S_{HH}}, \mathbf{S_{VV}})$ **vs** $\boldsymbol{\rho}(\mathbf{S_{HH}}, \mathbf{S_{HV}})$	0.53	47.70	0.92
$\boldsymbol{\rho}(\mathbf{S_{HH}}, \mathbf{S_{VV}})$ **vs** $\boldsymbol{\rho}(\mathbf{S_{VV}}, \mathbf{S_{HV}})$	0.52	49.27	0.97
$\boldsymbol{\rho}(\mathbf{S_{HH}}, \mathbf{S_{HV}})$ **vs** $\boldsymbol{\rho}(\mathbf{S_{VV}}, \mathbf{S_{HV}})$	0.55	64.21	0.85

As can be seen, the clustering quality of these three feature pairs is quite similar and all three do not have a high quality. This is indicated by the Silhouette coefficient being close to 0.5, a low value for the Calinski-Harabasz index, and a Davies-Bouldin index close to 1. This table only covers three feature pairs: a 25-by-25 matrix, similar as in Fig. 4.17, for these three quantitative measures, can indicate the clustering quality of all possible feature pairs. The evaluation metrics, averaged over 50 runs, after clustering by k-means with 3 clusters has been visualized in Fig. 4.19, 4.20 and 4.21.

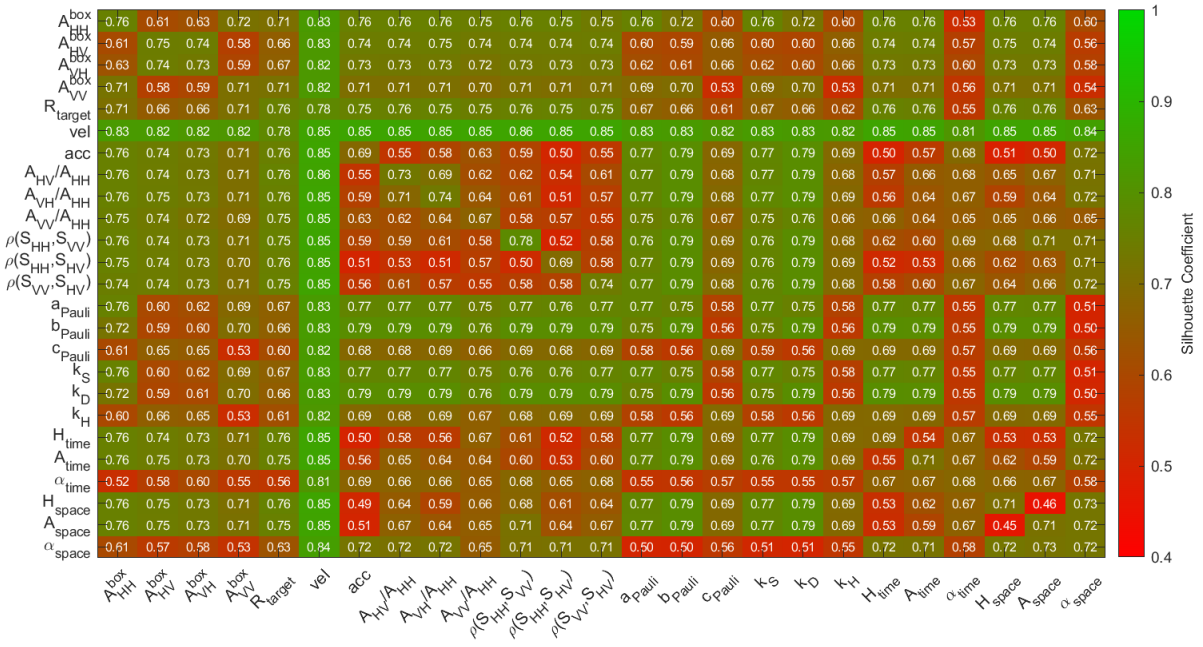

Figure 4.19: Silhouette coefficient matrix, indicating the resulted coefficient values for all possible feature pairs when clustering by k-means method with three classes

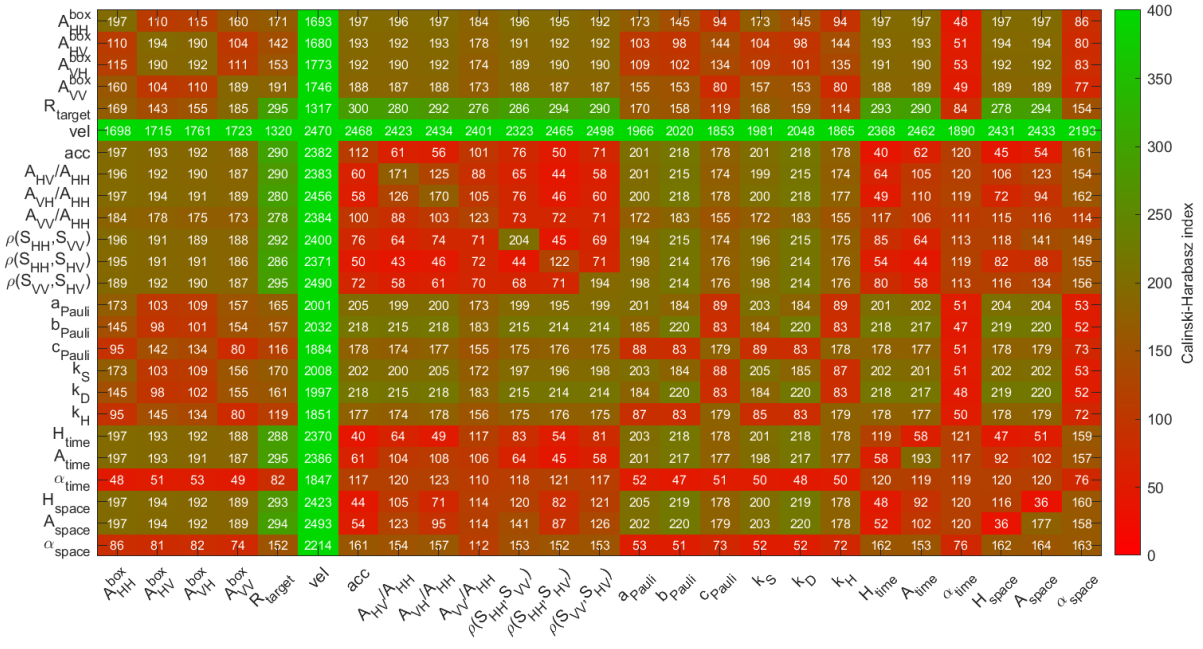

Figure 4.20: Calinski-Harabasz index matrix, indicating the resulted index values for all possible feature pairs when clustering by k-means method with three classes

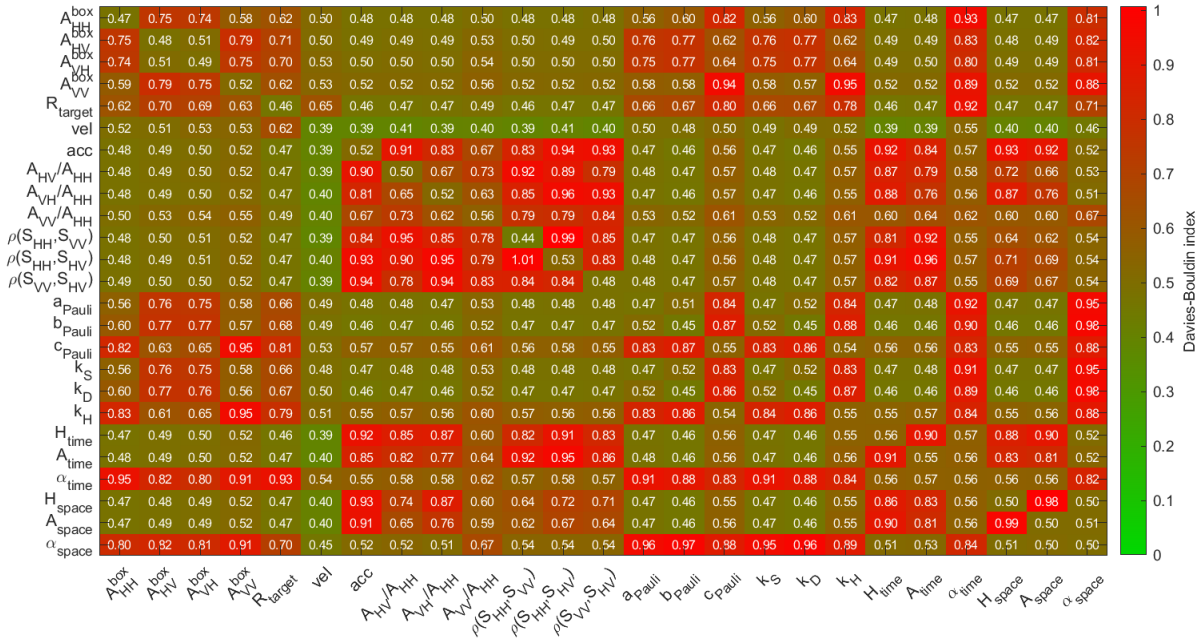

Figure 4.21: Davies-Bouldin index matrix, indicating the resulted index values for all possible feature pairs when clustering by k-means method with three classes

Preferably, the clusterization shows a Silhouette coefficient as close as possible to 1, a Calinski-Harabasz index as high as possible, and a Davies-Bouldin index as low as possible. These three figures show similar characteristics as the Hopkins statistic matrix (see Fig. 4.17). Since clustering has been applied to each feature pair individually, this makes total sense. The evaluation metrics of many feature pairs show good scores, but the resulted clusters do not provide new insights that can be useful for the classification of moving automotive vehicles.

4.4.4. Preliminary classification

The cluster tendency and cluster quality evaluation methods have shown that blind target classification using any feature pair does not provide new insights into the polarimetric signatures of moving automotive vehicles. However, many feature pairs are very strongly correlated, especially all features related to the measured polarimetric channels (e.g., maximum amplitudes, Pauli and Krogager coefficients). In general, this can be expected for most observed targets that are strongly polarized from the scattering physics and the derivations from the decompositions techniques. Nevertheless, combining feature pairs may result in clusters that are supported by features as well. Therefore, preliminary classification, based on the clusters of two pre-defined features, could lead to new interesting findings. A few examples of feature pairs that can be used for preliminary classification are discussed below.

Amplitude-based features From the analysis on the maximum amplitude of the target box of all polarization channels in Section 4.2.1, it has been shown that there is often a high correlation between the polarization channels. Obviously, amplitude-based features could be useful for classification. From a physical perspective, it makes total sense that automotive vehicles with a large surface, such as a truck, have a larger reflected amplitude than vehicles with smaller reflection surface, such as small cars or motorbikes, and all different sized vehicles in between, such as station wagons and vans, showing smaller amplitudes. This can be visualized by the data points in the feature space of $|S_{HH}|$ against $|S_{VV}|$ (see Fig. 4.2a) and $|S_{HH}|$ against the mean target length, by applying k-means

clustering. The resulted clusters, corresponding to three classes (i.e., large vehicles, medium-sized vehicles, small vehicles), can be seen in Fig. 4.22a and 4.22b.

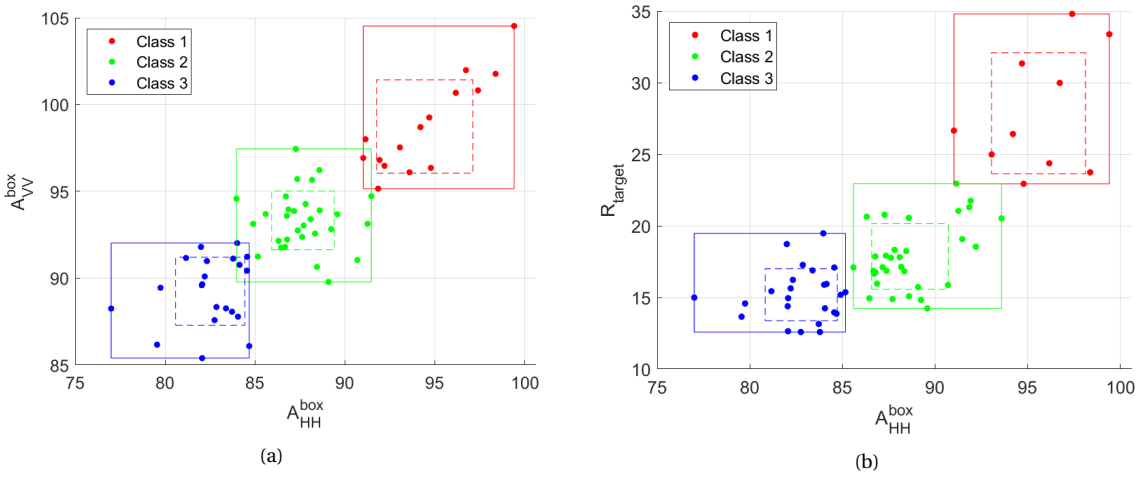

Figure 4.22: Feature spaces with the maximum amplitude of the target box averaged over time of polarimetric channels (a) $|S_{HH}|$ vs. $|S_{VV}|$ and (b) $|S_{HH}|$ vs. mean target length R_{target}, clustered in three classes by k-means method. Here the dashed and solid rectangles indicate the standard deviation and the min-max bounds, respectively, to visualize the cluster separability.

These clusters result in a Silhouette coefficient of 0.74 and 0.70, respectively, which verifies the assumption that these features are reasonable features for classification purposes. In order to find more correlations with other feature pairs, the resulting clusters will be used for preliminary classification. Then, the feature spaces of other feature pairs can be analyzed with labeled feature vectors. The quality of the resulting clusters can be assessed again by the evaluation metrics that have been used before. Instead of defining the labels by a k-means method for each feature pair, the labels are pre-determined by the clusters that have been formed by the aforementioned maximum amplitude

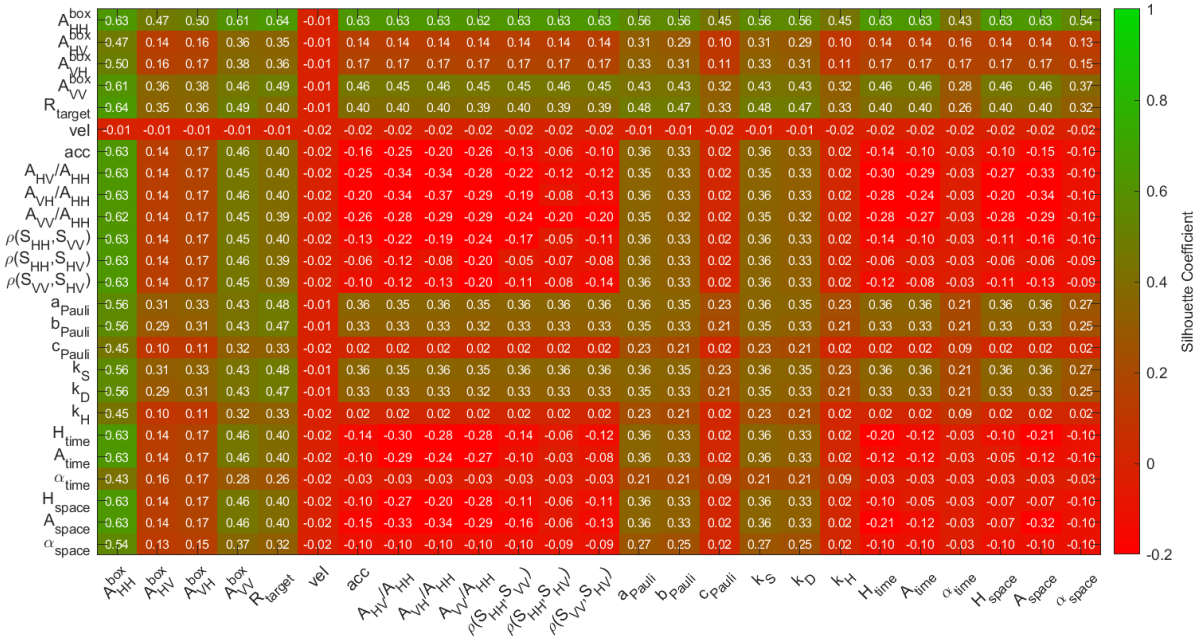

Figure 4.23: Silhouette coefficient matrix, indicating the resulted coefficient values for all possible feature pairs when labeling the data based on the maximum amplitudes $|S_{HH}|$ and $|S_{VV}|$ of the target box (see Fig. 4.2a)

and average target length. The Silhouette coefficient matrix can be found in Fig. 4.23 (see Appendix D.2 for the corresponding Calinski-Harabasz and Davies-Bouldin index matrix). Almost identical results have been found when using the feature space of $|S_{HH}|$ and the average target length R_{target} are used for preliminary classification.

As can be seen, many feature pairs can create clusters with this pre-labeled data set, that are not completely intermingled with each other. However, of all feature pairs that are indicated by green color, the highest achieved Silhouette coefficient is only 0.55. Besides, the feature pairs that do have relative good scores, are often directly related to the maximum amplitude $|S_{HH}|$ or $|S_{VV}|$, such as the Pauli coefficients a and b, and the Krogager coefficients k_S and k_D. Therefore, these feature pairs do not provide additional information that can be useful for classification purposes. Nevertheless, using the maximum amplitude and the mean target length as features for direct classification still makes sense and can be used to characterize the target.

Correlation-based feature pairs The clusters in Fig. 4.18a, based on the correlation coefficients between the polarized channels (i.e., $\rho(S_{HH}, S_{VV})$ and $\rho(S_{HH}, S_{HV})$), make physically clear sense and could therefore be used for classification already. However, the cluster quality, based on the Silhouette coefficient, is not that reasonable. A similar approach as the preliminary classification with amplitude-based features can be applied to these feature spaces, that visualize the classes described in Section 4.4.3. The matrix containing the values of the Silhouette coefficient of the labeled feature pairs is presented in Fig. 4.24 (see Appendix D.3 for the corresponding Calinski-Harabasz and Davies-Bouldin index matrix).

As can be seen, the silhouette coefficients are in general quite low, meaning that the resulting clusters are not compact and separable at all. However, some feature pairs show a relatively good score, such as the entropy H and anisotropy A, both averaged over time and space, with the correlation coefficients that are used for preliminary labeling. This relation can be seen in the feature spaces in Fig. 4.25a and 4.25b. Again, note that the labels are originating from the preliminary labeling and not from direct clustering by the k-means method. When analyzing the range of distribution of the

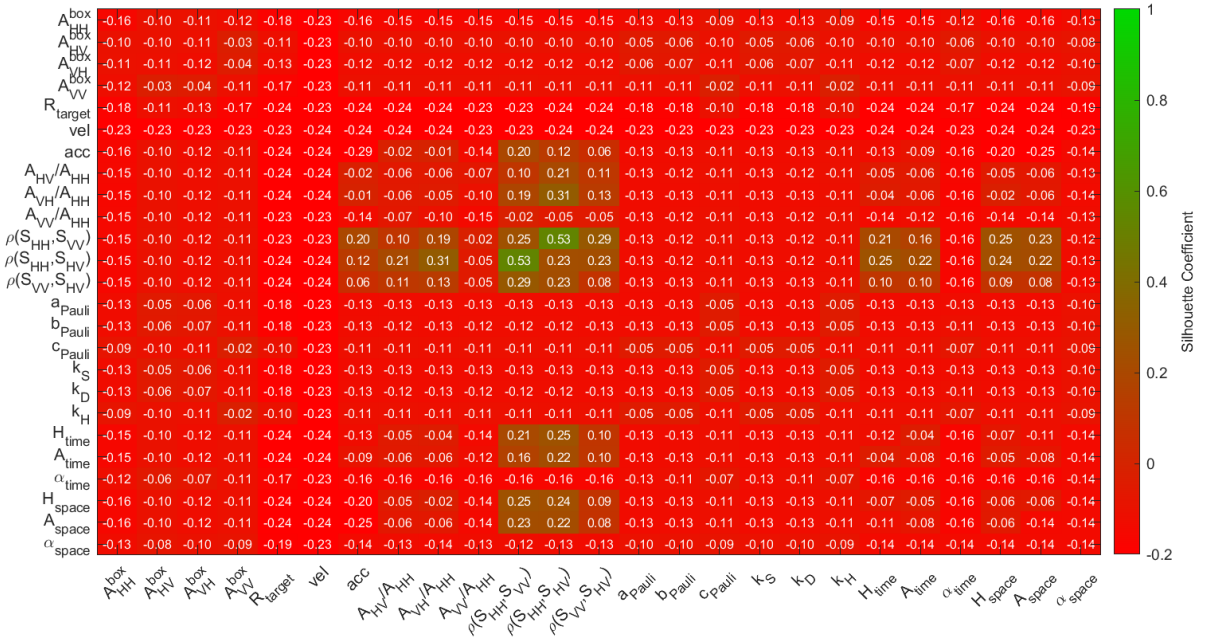

Figure 4.24: Silhouette coefficient matrix, indicating the resulted coefficient values for all possible feature pairs when labeling the data based on the clusters originating from $\rho(S_{HH}, S_{VV})$ vs. $\rho(S_{HH}, S_{HV})$ (see Fig. 4.18a)

entropy H, it can be seen that class 1 and class 2, representing targets with high correlation between the co-polarized channels, show similar values, whereas class 3 represents targets with low correlation between all polarization channels, tends to have increased values for H. This makes total sense, since higher entropy means more randomness in the target's scattering behavior, as discussed in Section 4.3.2. Besides, as the low Silhouette coefficient already suggested, the cluster quality of not sufficient due to the bad cluster separability. Hence, despite the fact of the physical clear sense of clusterization of targets with correlation-based features, the classification is supported by cluster separability using other analyzed features. The interpretation of such target classification using correlation-based features still has to be discovered.

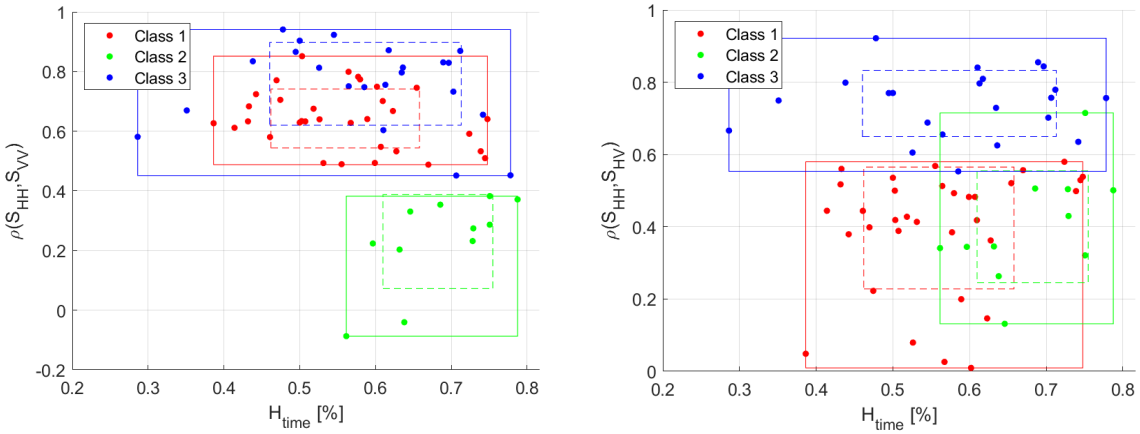

Figure 4.25: Feature spaces with the entropy H (averaged over time) and the correlation coefficients (a) $\rho(S_{HH}, S_{VV})$ and (b) $\rho(S_{HH}, S_{HV})$, which are used for preliminary classification of the targets, that are labeled in here according to its assigned class. Here the dashed and solid rectangles indicate the standard deviation and the min-max bounds, respectively, to visualize the cluster separability.

Entropy-based features In Section 4.3.2 the $H/A/\alpha$-decomposition has been discussed and the target scattering behavior has been analyzed in the two-dimensional H/α-plane. In Fig. 4.12 the data distribution of the entropy H and the α angle of the received signals, both averaged over time and space, has been presented. These two parameters are often used for the classification of the target's scattering mechanism, according to the classification scheme in Fig. 4.10. Therefore, the entropy H and the α angle can be used as entropy-based features. These features are plotted against each other, both returned from averaging over time and over space, in Fig. 4.26a and 4.26b, respectively. Here the mean of $\overline{H}_{space}$ and $\overline{\alpha}_{space}$ has been used as a feature, such that each target can be characterized by a single data point.

The clustering quality of these two feature spaces is 0.53 and 0.51, respectively, meaning that the cluster compactness and separability are not sufficient for classification. Nevertheless, a similar analysis with preliminary classification, based on the clusters of $\overline{H}_{time}$ against $\overline{\alpha}_{time}$, has been conducted. The resulted Silhouette coefficient matrix can be seen in 4.27 (see Appendix D.4 for the corresponding Calinski-Harabasz and Davies-Bouldin index matrix). As expected, all feature pairs show a low Silhouette coefficient. Similar results are found when using $\overline{H}_{space}$ and $\overline{\alpha}_{space}$ as feature pair for preliminary classification. Therefore, these features do not provide any helpful insights for classification purposes.

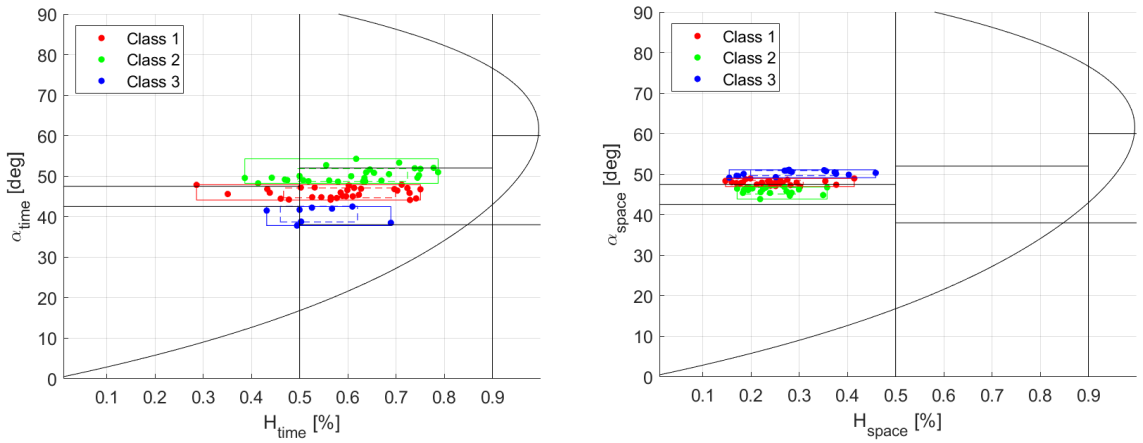

Figure 4.26: Feature spaces in the two-dimensional H/α-plane with the entropy H and α angle (a) when averaged over time and (b) when averaged over space, clustered in three classes by k-means method. Here the dashed and solid rectangles indicate the standard deviation and the min-max bounds, respectively, to visualize the cluster separability.

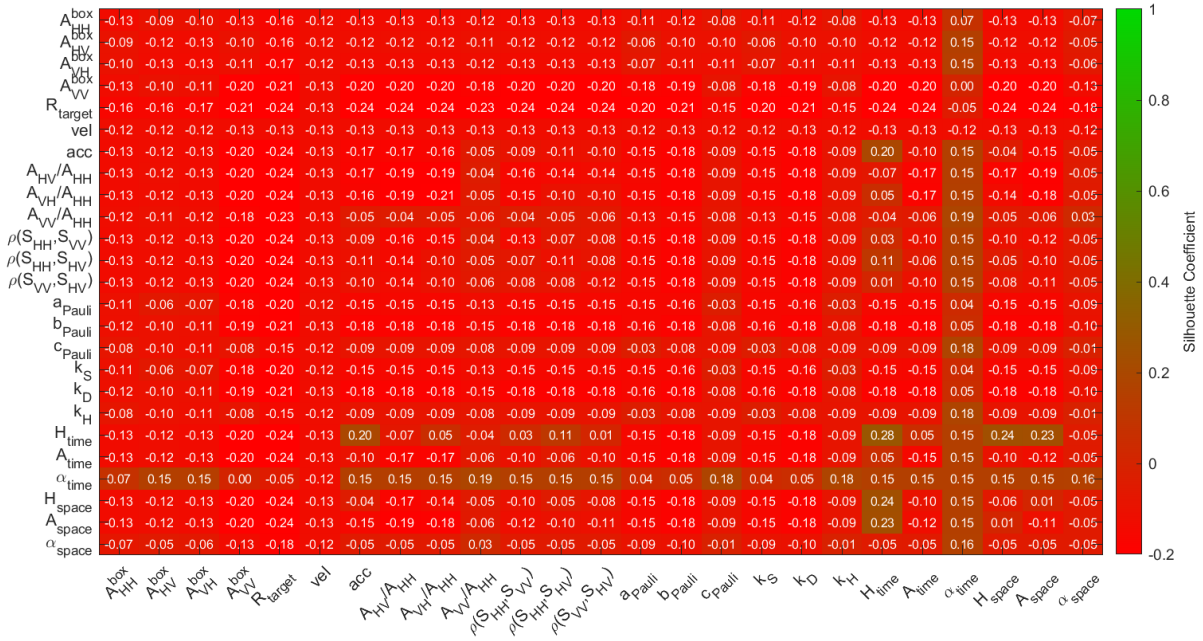

Figure 4.27: Silhouette coefficient matrix, indicating the resulted coefficient values for all possible feature pairs when labeling the data based on the clusters originating from the H/α-plane (averaged over time) feature space (see Fig. 4.26a)

4.4.5. Preliminary conclusion of target feature extraction

A target feature database, consisting of many features (25) but only a few observed targets (66), has been analyzed based on its clustering tendency and clustering quality. Using the analyzed data set of polarimetric features, we did not find reliable clusters in the created feature database of observed moving automotive targets. Polarimetric features provide well-defined reliable statistical relations between physically related features (amplitude-based, correlation-based, and entropy-based features). However, at this stage of the research, we did not find well-defined feature pairs for the classification of moving automotive targets, except the polarimetric correlation coefficients, which, unfortunately, were not supported by the other features. For such cluster definition, we can recommend using more massive data sets and analyzing the features utilizing a labeled feature database.

4.5. Resulted clutter features

Although that the goal of this thesis is to identify target attributes that can contribute to the classification of moving automotive vehicles, it has been concluded that we did not find well-defined features in our data set that can be used to distinguish sub-classes of automotive targets from each other. However, the target feature database can be extended by adding polarimetric data of static clutter.

In Section 2.3.4 it has been explained that static clutter has been filtered out for further analysis. In this section, the unfiltered data will be used for feature extraction, such that the polarimetric features of the targets can be compared to the polarimetric features of static clutter. Therefore, a separate clutter feature database is created, consisting of all polarimetric data (as described in Section 3.5) of the static clutter. Here, the static clutter is defined as all bins in the range-Doppler spectrum within ±1 km/h, separated in rectangular boxes of approximately 33 m (i.e., 10 range bins).

Then, the target feature database (66 samples) and the clutter feature database (30 samples) will be combined into one feature database. Since the clutter's length and dynamics are not interesting to analyze, these features are discarded, resulting in a 96-by-22 labeled feature matrix. The labels correspond to either 'Target' or 'Clutter'. This feature database can be analyzed in a similar way as described in Section 4.4.3. The Silhouette coefficient for each feature pair has been computed, where the clusters are defined by the labels of the data points, as is shown in Fig. 4.28 (see Appendix D.5 for the corresponding Calinski-Harabasz and Davies-Bouldin index matrix). From these figures, it can be seen that the most promising feature pairs are formed by the entropy-based features, resulting from the $H/A/\alpha$-decomposition.

Figure 4.28: Silhouette coefficient matrix, indicating the resulted coefficient values for all possible feature pairs when labeling the data based on target and static clutter information

The feature pair $\overline{H}_{space}$ against $\overline{A}_{space}$ shows high scores, meaning that the cluster quality is relatively good. Again, note that these metrics are only an indication of the clustering quality and can be distorted if, for example, a few outliers are present. Nevertheless, it might be interesting to analyze the data distribution of the entropy H and the α angle of the reflections from the static clutter. These results, both when averaging over time and space, can be seen in Fig. 4.29. When comparing these two-dimensional H/α-planes with those that correspond to the reflections of the targets (see

Fig. 4.12 on page 64), it can be seen that the data distribution of H and α when averaging over time is similar. However, the data distribution when averaging over space shows that the scattering of targets is completely different than the scattering of static clutter. The entropy $\overline{H}_{space}$ of targets is centered around 0.2, whereas the entropy $\overline{H}_{space}$ of clutter is in general higher. Since the entropy represents the randomness of the scattering, it can be concluded that the reflections of targets are more polarized than those of clutter, which makes total sense.

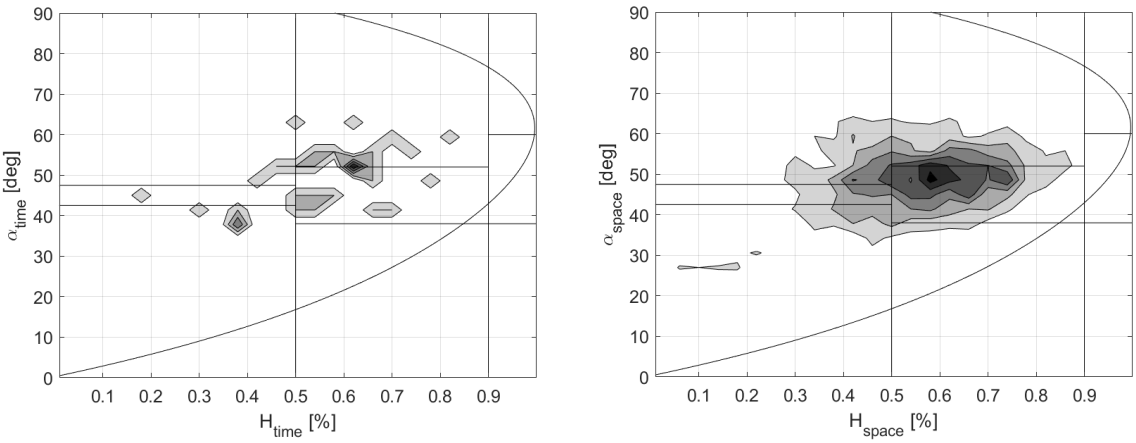

(a) (b)

Figure 4.29: Data distribution of the received signals corresponding to static clutter in the two-dimensional H/α-plane, resulted from (a) the clutter's maximum amplitude over time and (b) the clutter's box amplitude averaged over space

For a better comparison, the feature spaces of $\overline{H}_{time}$ against $\overline{\alpha}_{time}$ and $\overline{H}_{space}$ against $\overline{\alpha}_{space}$ are shown in Fig. 4.30a and 4.30b, respectively. In the latter feature space, the mean value for $\overline{H}_{space}$ and $\overline{\alpha}_{space}$ over time has been used, such that each data point represents a single target or clutter box. These feature spaces confirm that the data distribution in the two-dimensional H/α-plane, when averaging over time, is similar for target and clutter scattering, whereas when averaging over space, the scattering of targets and clutter can be distinguished easily from each other. Therefore, it can be concluded that the feature pair $\overline{H}_{space}$ and $\overline{\alpha}_{space}$ can be very useful for the classification of moving automotive vehicles with respect to static clutter. These features even allow instant classification, as time averaging is not required to derive these parameters.

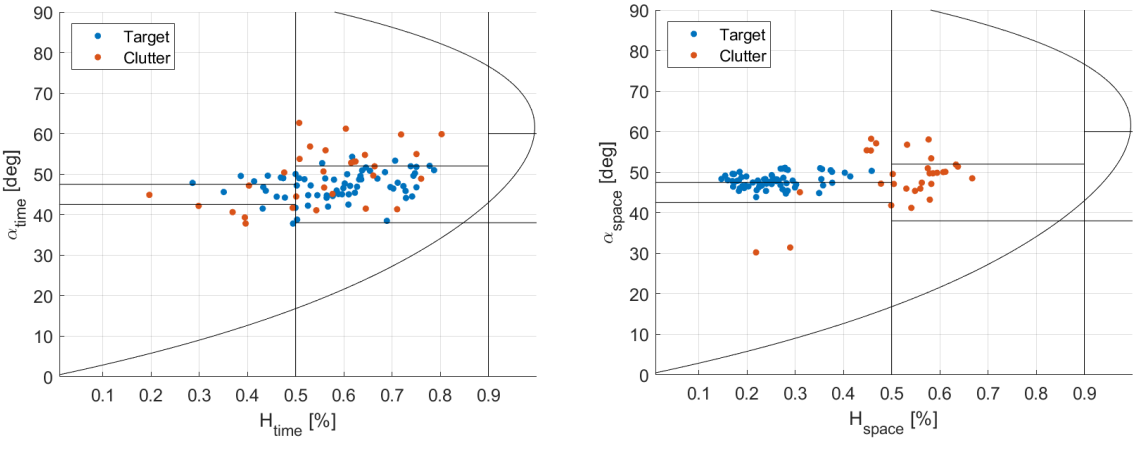

(a) (b)

Figure 4.30: Feature space with the mean entropy H against (a) the mean α angle and (b) the mean anisotropy A of target scattering and static clutter scattering

Besides the feature spaces originating from the H/α-plane, the Silhouette matrix in Fig. 4.28 indicates high scores for other feature pairs as well. For example, the anisotropy A and the correlation coefficient $\rho(S_{HH}, S_{HV})$ in combination with the entropy $\overline{H}_{space}$ show promising clustering quality as well. The labeled data set has been visualized in these features spaces, as can be seen in Fig. 4.31. Again, the clusters corresponding to the target scattering are well separated from the clusters corresponding to the clutter scattering. Different from Fig. 4.30b and 4.31a, where the cluster separation is mainly caused by the data distribution of $\overline{\alpha}_{space}$, this feature in combination with $\rho(S_{HH}, S_{HV})$ even show segregation in direction of the the correlation coefficient. Clutter scattering tends to have both a higher entropy value and a lower correlation coefficient between $|S_{HH}|$ and $|S_{HV}|$, which again verifies that the target scattering is more polarized than clutter scattering.

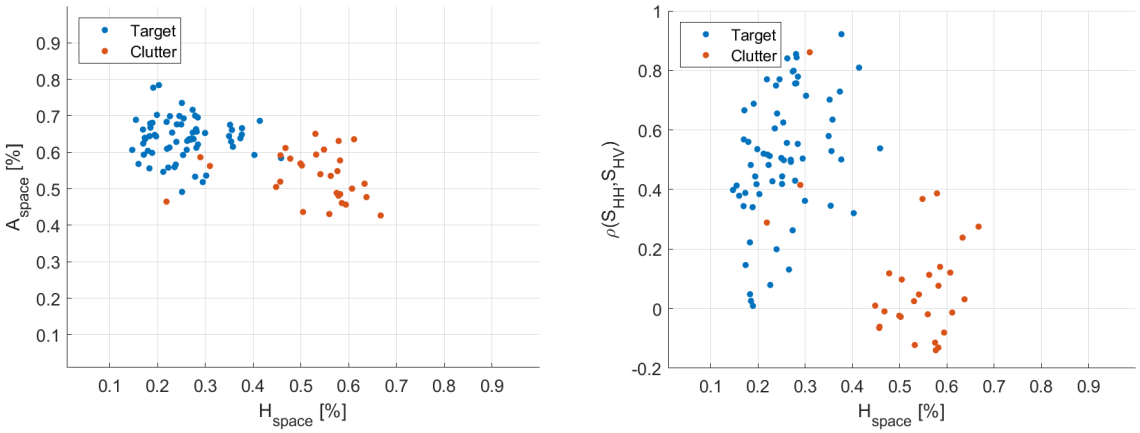

(a) (b)

Figure 4.31: Feature space with the mean entropy $\overline{H}_{space}$ against (a) the mean anisotropy $\overline{A}_{space}$ and (b) the correlation coefficient $\rho(S_{HH}, S_{HV})$ of target scattering and static clutter scattering

These feature spaces created with other similar data sets (recorded directly after the original data set used so far) show very similar results (see Appendix D.6). From this it can be concluded that the features $\overline{H}_{space}$, $\overline{A}_{space}$ and $\rho(S_{HH}, S_{HV})$ show compact and well-separated clusters that can be very useful for classification. It can be concluded that with these features, even without velocity information, a classifier should be able to accurately distinguish moving vehicles from static clutter.

4.6. Conclusion

In this chapter the feature database, as a result of the feature database creation while tracking multiple automotive targets on a highway, has been analyzed to extract polarimetric features for classification purposes. Ideally, these extracted features function as target attributes and can fully describe the polarimetric signature of sub-classes of moving automotive targets. To find useful features, an introduction to unsupervised learning approaches is given, where the key concept is self-learning of previously unknown patterns based on an unlabeled data set. Besides association methods, clustering techniques (e.g., k-means clustering, hierarchical clustering, DBSCAN, etc.) are the most important unsupervised learning tools to achieve the main goal. After clustering, a physical interpretation of the clusters is required to define the classes, label the data, and train a classifier.

Therefore, an analysis of the feature database has been performed. Before any conclusions can be drawn from this analysis, it has been validated that the feature database is in line with the theory behind polarized scattering. It has been shown that the target's maximum amplitude of co-polarized and cross-polarized channels are strongly correlated with each other. Here the latter verifies that $S_{HV} \approx S_{VH}$ (with a small offset due to non-calibrated system), as PARSAX is a monostatic radar.

Furthermore, the target's maximum amplitude between co-polarized and cross-polarized channels ($|S_{HH}|$ against $|S_{HV}|$ and $|S_{VV}|$ against $|S_{HV}|$) is correlated but less significant than the co- and cross-polarized channels among each other. The correlation coefficient $\rho(x, y)$ among all polarization channels has been exploited for each target, resulting in interesting feature spaces with clear physical meaning.

To gain a better insight into the physical meaning of these feature spaces, the target feature database is extended by several polarimetric decomposition techniques. The decomposition methods provide new parameters that can contribute to a higher correlation with different classes, and therefore improve the feature quality. Based on the coherence matrix, which covers the statistical average of all scattering information, the Huynen target generators and the $H/A/\alpha$ parameters are derived. The $H/A/\alpha$-decomposition is a useful method for effective feature extraction and is commonly used for the physical interpretation of the scattering mechanism. The entropy H and α angle are often visualized in the two-dimensional H/α-plane, which directly presents the type of scattering according to a simple classification scheme. The data distribution of the received signals corresponding to the targets has been presented in this H/α-plane. Moreover, the Pauli decomposition and Krogager decomposition have been explained and applied to the range-Doppler data. The three Pauli and Krogager coefficients have been visualized in a color-coded RGB image, providing new features to extend the feature database.

The collected target feature database, consisting of 25 features, has been analyzed. The clustering tendency has been assessed by the Hopkins statistic of each possible feature pair, indicating whether a feature space is meaningful and not misleading. If a feature space does not contain clustering tendency, the resulting clusters may be irrelevant at all. Although that many of these feature spaces show high clustering tendency, they do not directly provide new insights into the polarimetric signatures of the automotive targets, since these high values are due to a clear physical relation with each other (high correlation) or due to the sign of the target's velocity. Nevertheless, it has been found, by k-means clustering, that the targets can be separated in three sub-classes based on the correlation coefficients between co-polarized channels ($\rho(S_{HH}, S_{VV})$) and between co-and cross-polarized channels ($\rho(S_{HH}, S_{HV})$ and $\rho(S_{VV}, S_{HV})$). The clustering quality has been assessed by several cluster evaluation metrics, such as the Silhouette coefficient, the Calinski-Harabasz index, and the Davies-Bouldin index. The quantitative measures are used to create several 25-by-25 matrices that provide a clear overview of the clustering quality of all possible feature pairs. The clustering tendency and clustering quality evaluation metrics have shown that blind classification using any feature pair does not provide new insights that are useful for the classification of moving automotive vehicles. Nevertheless, further analysis has been conducted by means of preliminary classification based on amplitude-based, correlation-based, and entropy-based features, but did not lead to new insights as well.

From this feature extraction analysis, using a target feature database consisting of 25 features and only 66 targets, it has been found that polarimetric features of the observed targets provide well-defined reliable statistical relations between physically related features. However, we did not find reliable clusters that are useful to describe the polarimetric signatures of moving automotive vehicles, except the polarimetric correlation coefficients, which, unfortunately, despite their physical clear sense, were not supported by the other analyzed features.

In spite of this, the polarimetric features of moving vehicles have been compared with those of static clutter. Based on the clustering quality measures, computed with a labeled feature matrix which is composed by the target and clutter feature database, it has been found that the features originating from the $H/A/\alpha$-decomposition show high potential for classification of targets with respect to static clutter. The data distribution of the received signals corresponding to both targets and clutter has been compared with each other in the two-dimensional H/α-plane. From this, it can be seen

that the features $\overline{H}_{space}$, $\overline{A}_{space}$ and $\rho(S_{HH}, S_{HV})$ show compact and well-separated clusters corresponding to target features and clutter features. Therefore, it can be concluded that with these features, even without velocity information, a classifier should be able to accurately distinguish moving vehicles from static clutter.

5

Conclusion and Future Work

The goal of this thesis was to identify polarimetric target features that can contribute to the classification and definition of sub-classes of automotive targets driving on a highway from small compact cars to large trucks, based on a feature database extracted from real observations of a polarimetric-Doppler radar (PARSAX). Motivated by the potential of the exploitation of polarimetric-Doppler signatures for automotive target classification, the development of a dedicated polarimetric radar signal and data processing chain was performed, a polarimetric feature database with 66 targets was created, and the resulted target feature database was investigated. This chapter presents the major conclusions for the performed research and provides recommendations for future work.

Development of a polarimetric feature database In order to create a polarimetric feature database, all moving vehicles that can be observed by the radar, need to be detected and tracked over time, which is most straightforwardly performed in the range-Doppler domain. As a result of this thesis, a dedicated signal and data processing chain to process the real-world data, originating from the fully polarimetric-Doppler surveillance radar PARSAX, developed by the TU Delft, has been developed. This process is composed of the following four stages:

1. **Radar Signal Processing**: The sampled IF radar signals are pre-processed and a HPF is applied to remove static clutter. After that, a two-dimensional FFT has been performed over fast and slow time to provide the range-Doppler map for each of four polarimetric channels.

2. **Target Detection**: Before target detection takes place, to gain full advantage of the additional polarimetric information, polarimetric data fusion is applied. All four range-Doppler spectra, corresponding to the four elements of the PSM, are integrated into a single range-Doppler map per time frame. To detect the targets in the range-Doppler domain, the OS-CFAR detector is selected over the non-adaptive detector and other CFAR detector variants. Imperfections and distortions (due to noise, clutter, and other limitations) of the resulted binary detection map are resolved by applying a morphological filter, exploiting the aliasing property of Doppler processing, and discarding detections with low velocity by an additional HPF. Subsequently, the DBSCAN clustering algorithm is applied such that a group of detected cells represent a single target, which will simplify the tracking algorithm significantly.

3. **Target Tracking**: In order to track multiple targets from frame to frame, a basic MTT-algorithm is developed. A classical Kalman filter is used to update and predict the state of each target, according to a constant acceleration state dynamics model. To associate each measurement to

a certain track, the GNN-method, based on minimizing the total statistical distance, has been selected. Beforehand, to simplify the data association problem, a hyperellipsoid gate, which incorporates the statistical Mahalanobis distance, is applied. To cope with Doppler ambiguity, an MHT-based solution has been proposed. The hypothesis with the highest probability will determine whether the track can consider the velocity measurement to be folded or not. At last, an M/N logic test is selected over SPRT-method to solve the track management problem, such that all unassigned measurements will initialize a new track, and all tracks that are not associated with a measurement, will be deleted.

4. **Target Feature Database Creation**: While tracking all moving targets, the amplitude and phase information of all four polarization range-Doppler maps, cluster information, target size, and target dynamics is collected. This polarimetric information forms the basis of the target feature database.

Polarimetric target feature analysis The signal and data processing chain described above has been applied to real-world polarimetric radar data, representing the scattering of a dense highway between The Hague and Rotterdam (A13). As a result, a database with polarimetric features of 66 targets have been created for the first time from PARSAX data. To find features that describe the polarimetric signature of automotive vehicles and thus can be useful for the classification of these targets, a feature extraction analysis was performed, utilizing unsupervised machine learning techniques. Before any conclusions can be drawn from this analysis, it has been validated that the feature database is in line with the theory behind polarized scattering, based on the feature spaces of amplitude information, the correlation between the polarization channels, the target length, and the target dynamics. To gain a better insight into the physical meaning of these feature spaces, the target feature database has been extended by new polarimetric features, by using several polarimetric decomposition techniques. Besides computing the Pauli and Krogager coefficients for each target as new features, the entropy H, anisotropy A, and α angle are derived from the $H/A/\alpha$-decomposition technique.

The cluster tendency of all possible feature spaces from the target feature database, consisting of 25 features, was estimated by the Hopkins statistic. Although that many of these feature spaces show a high clustering tendency, they do not directly provide new insights into the polarimetric signatures of automotive vehicles. Nevertheless, it has been found, by k-means clustering, that the targets can be separated into three sub-classes based on the correlation coefficients between the maximum amplitude of all polarization channels. The quality of the found clusters has been assessed by the Silhouette coefficient, the Calinski-Harabasz index, and the Davies-Bouldin index, resulting in 25-by-25 matrices that provide a clear overview of the clustering quality of all possible feature pairs. These evaluation metrics have shown that blind classification using any feature pair does not provide new insights that are useful for the classification of automotive vehicles. Further analysis by means of preliminary classification based on amplitude-based, correlation-based, and entropy-based features, did not lead to new insights as well.

Given this analysis, it was concluded that polarimetric features of the observed targets provide well-defined reliable statistical relations between physically related features. However, reliable clusters that are useful to describe the polarimetric signatures of moving automotive vehicles are not found, except the polarimetric correlation coefficients, which, unfortunately, despite their physical clear sense, were not supported by the other analyzed features. Nevertheless, instead of aiming for finding target attributes to define sub-classes of automotive vehicles, the polarimetric features of moving targets have been compared with those of static clutter. It has been found that the entropy-based features (originating from the $H/A/\alpha$-decomposition) form compact and well-separated clusters corresponding to target features and clutter features.

Therefore, from these novel findings it was concluded that with these features, a classifier should be able to accurately distinguish moving vehicles from static clutter. Even without velocity information, these moving vehicles can easily be classified from static clutter by means of the found entropy-based features. These findings indicate that additional polarimetric information can be used to improve the detection and recognition of automotive vehicles in polarimetric radar data. This is a new achievement in the field of automotive vehicles classification and may be used a main result for a scientific publication (probably published as conference proceeding).

Recommendations for future research So far, the main achievements of this thesis have been outlined, but several recommendations for future research could be addressed. First, whereas our target feature database included polarimetric information of only 66 targets, I recommend using more massive data sets and analyzing the features utilizing labeled data sets to find useful clusterization and well-defined sub-classes. More polarimetric radar data sets, with different angles aspects of the vehicles with respect to the radar, could improve the quality of the clusterization of the features. Besides, using a well-calibrated radar allows the use of phase-based features as well, which might help find useful feature pairs.

Regarding target classification and clustering of polarimetric features, more advanced clustering analysis is proposed for future research. This could be beneficial for finding feature pairs with higher cluster quality. For example, instead of partitioning the data into three clusters by the k-means method, using other clustering techniques or varying the pre-defined number of clusters may provide more insight into the feature database. Also, a similar features extraction process with other objects (e.g., wind mills, drones, birds, etc.) could be performed and included to improve the classification performance.

Furthermore, more research on the found correlation-based features must be conducted to get more insight into the interpretation of the classes as a result of the clusterization. Moreover, as the entropy-based features clearly discriminate the scattering behavior of moving targets from static clutter, I recommend evaluating the classification performance by using these feature pairs as input for any classifier and comparing the resulted predictions with a labeled data set.

Additionally, for each block in the signal- and data processing chain a certain method or algorithm has been selected for further processing, which was often the most simple, yet effective option. Obviously, more advanced techniques could be implemented to improve the detection and tracking performance, resulting in a more reliable target feature database. Examples are:

- The data association could be improved by implementing the JPDA- or MHT-algorithm. With these techniques, more information than only the kinematics, such as target size, can be taken into account to match all measurements to the tracks, also known as feature-aided tracking [9]. Besides, the MHT-based approach to solve the Doppler ambiguity could be integrated more easily, similar as in [72].

- The range where a track is initialized could be included in the computation of the probability of whether the velocity measurement of that track is folded or not. It is more likely that a track with a positive velocity measurement is initialized at a small range from the radar, as it is moving away from the radar. Similarly, it is expected that a new track initialized far away from the radar is moving towards the radar and thus has a negative velocity measurement.

- In this data processing chain, the detection is completely separated from the tracking processing. Instead, these functions can be combined in a well-designed track-before-detect algorithm, which may improve the tracking performance [71]. On top of that, whereas tracking is currently based on a classical Kalman filter with only a single measurement per target per

time frame is used as input, this Kalman filter could be extended such that four detection maps, corresponding to the for elements of the PSM, are used as input. Thus, instead of a single Kalman filter, the results of multiple filters are combined. This is also known as track-to-track fusion [63].

This research has shown that polarimetric features of moving automotive vehicles, extracted while tracking the targets in a multi-target environment in the range-Doppler domain, can be used to distinguish the vehicles from static clutter. More research has to be conducted to find polarimetric features that can contribute to the classification and definition of sub-classes of automotive targets driving on a highway.

Bibliography

[1] R. Dragon, "Cars on road during daytime," 2020. [Online]. Available: https://unsplash.com/photos/3ZTs5h228Vk

[2] R. Hussain and S. Zeadally, "Autonomous cars - Research results, issues, and future challenges," *IEEE Communications Surveys and Tutorials*, vol. 21, no. 2, pp. 1275–1313, 4 2019.

[3] M. A. Richards, *Fundamentals of radar signal processing*, 2nd ed. McGraw-Hill Education, 2013.

[4] W. Wiesbeck and L. Sit, "Radar 2020 - The future of radar systems," in *International Radar Conference 2014*. Lille, France: IEEE, 3 2014, pp. 1–6.

[5] M. Adams, E. Jose, and B.-N. Vo, *Robotic navigation and mapping with radar*, 1st ed. Boston: Artech House, 2012.

[6] M. A. Saville, J. A. Jackson, and D. F. Fuller, "Rethinking vehicle classification with wide-angle polarimetric SAR," *IEEE Aerospace and Electronic Systems Magazine*, vol. 29, no. 1, pp. 41–49, 1 2014.

[7] O. A. Krasnov and L. P. Ligthart, "Radar polarimetry using sounding signals with dual orthogonality - PARSAX approach," in *European Microwave Week (EuMW) - 7th European Radar Conference (EuRAD) 2010*. Paris, France: IEEE, 2010, pp. 121–124.

[8] J. S. Lee and E. Pottier, *Polarimetric radar imaging - from basics to applications*, 1st ed. Boca Raton, FL, USA: CRC Press LLC, 2009.

[9] D. H. Nguyen, J. H. Kay, B. J. Orchard, and R. H. Whiting, "Feature-aided tracking of moving ground vehicles," *Algorithms for Synthetic Aperture Radar Imagery IX*, vol. 4727, pp. 234–245, 8 2002.

[10] J. R. Copeland, "Radar target classification by polarization properties," *Proceedings of the IRE*, vol. 48, no. 7, pp. 1290–1296, 7 1960.

[11] F. Kuhl and R. Covelli, "Object identification by multiple observations of the scattering matrix," *Proceedings of the IEEE*, vol. 53, no. 8, pp. 1110–1115, 8 1965.

[12] O. Lowenschuss, "Scattering natrix application," *Proceedings of the IEEE*, vol. 53, no. 8, pp. 988–992, 8 1965.

[13] R. Tsu, "The theory and application of the scattering matrix for electromagnetic waves," Ohio State University, Tech. Rep. 2, 8 1960.

[14] I. D. Olin and F. D. Queen, "Dynamic measurement of radar cross sections," *Proceedings of the IEEE*, vol. 53, no. 8, pp. 954–961, 8 1965.

[15] J. R. Huynen, "Measurement of the target scattering matrix," *Proceedings of the IEEE*, vol. 53, no. 8, pp. 936–946, 8 1965.

[16] ——, "Phenomenological theory of radar targets," Ph.D. dissertation, Delft University of Technology, 1970.

[17] W. M. Boerner, M. El-Arini, C. Chan, S. Saatchi, W. Ip, P. Mastoris, and B. Foo, "Polarization utilization in radar target reconstruction," University of Illinois at Chicago Circle, Chicago, Tech. Rep., 1981.

[18] W. M. Boerner and A. Manson, "Interpretation of high-resolution polarimetric radar target down-range signatures using Kennaugh's and Huynen's target characteristic operator theories," in *Inverse Methods in Electromagnetic Imaging*. Hingham, MA, USA: D. Reidel Publishing Company, 1985, ch. 2, pp. 695–720.

[19] W. M. Boerner, W. L. Yan, A. Q. Xi, and Y. Yamaguchi, "On the basic principles of radar polarimetry: The target characteristic polarization state theory of Kennaugh, Huynen's polarization fork concept, and its extension to the partially polarized case," *Proceedings of the IEEE*, vol. 79, no. 10, pp. 1538–1550, 1991.

[20] D. Giuli, "Polarization diversity in radars," *Proceedings of the IEEE*, vol. 74, no. 2, pp. 245–269, 2 1986.

[21] L. Pierce, F. T. Ulaby, K. Sarabandi, and M. C. Dobson, "Knowledge-Based Classification of Polarimetric SAR Images," *IEEE Transactions on Geoscience and Remote Sensing*, vol. 32, no. 5, pp. 1081–1086, 9 1994.

[22] K. S. Chen, W. P. Huang, D. H. Tsay, and F. Amar, "Classification of multifrequency polarimetric SAR imagery using a dynamic learning neural network," *IEEE Transactions on Geoscience and Remote Sensing*, vol. 34, no. 3, pp. 814–820, 5 1996.

[23] S. R. Cloude and E. Pottier, "An entropy based classification scheme for land applications of polarimetric SAR," *IEEE Transactions on Geoscience and Remote Sensing*, vol. 35, no. 1, pp. 68–78, 1 1997.

[24] A. Bennett and A. Currie, "The stability of polarimetric features for target classification from SAR imagery," in *RADAR 2002*, vol. 490. Edinburgh, UK: IET, 10 2002, pp. 395–399.

[25] J. Burns, D. Herrick, and M. Ricoy, "Wideband ISAR signatures of ground vehicles at UHF frequencies," in *IEEE Antennas and Propagation Society International Symposium 1992 (Digest)*. Chicago, IL, USA: IEEE, 6 1992, pp. 1136–1140.

[26] N. Kees and J. Detlefsen, "Road surface classification by using a polarimetric coherent radar module at millimeter waves," in *IEEE MTT-S International Microwave Symposium Digest 1994*. San Diego, CA, USA: IEEE, 5 1994, pp. 1675–1678.

[27] R. Finkele, A. Schreck, and G. Wanielik, "Polarimetric road condition classification and data visualisation," in *International Geoscience and Remote Sensing Symposium (IGARSS) 1995*. Firenze, Italy: IEEE, 7 1995, pp. 1786–1788.

[28] R. Finkele, "Detection of ice layers on road surfaces using a polarimetric millimetre wave sensor at 76 GHz," *Electronics Letters*, vol. 33, no. 13, pp. 1153–1154, 6 1997.

[29] K. Sarabandi and E. S. Li, "Polarimetric characterization of debris and faults in the highway environment at millimeter-wave frequencies," *IEEE Transactions on Antennas and Propagation*, vol. 48, no. 11, pp. 1756–1768, 11 2000.

[30] R. Schneider, "Modellierung der Wellenausbreitung für ein bildgebendes Kfz-Radar," Ph.D. dissertation, Universität Fridericiana Karlsruhe, 1998.

[31] G. Wanielik, N. Appenrodt, H. Neef, R. Schneider, and J. Wenger, "Polarimetric millimeter wave imaging radar and traffic scene interpretation," *IEE Colloquium on Automotive Radar and Navigation Techniques*, no. 230, 2 1998.

[32] T. Schipper, J. Fortuny-Guasch, D. Tarchi, L. Reichardt, and T. Zwick, "RCS measurement results for automotive related objects at 23-27 GHz," in *5th European Conference on Antennas and Propagation (EUCAP) 2011*. Rome, Italy: IEEE, 5 2011, pp. 683–686.

[33] K. Geary, J. S. Colburn, A. Bekaryan, S. Zeng, and B. Litkouhi, "Characterization of automotive radar targets from 22 to 29 GHz," in *IEEE Radar Conference 2012*. Atlanta, GA, USA: IEEE, 5 2012, pp. 79–84.

[34] K. Geary, J. S. Colburn, A. Bekaryan, S. Zeng, B. Litkouhi, and M. Murad, "Automotive radar target characterization from 22 to 29 GHz and 76 to 81 GHz," in *IEEE Radar Conference 2013*. Ottawa, Canada: IEEE, 5 2013.

[35] S. Trummer, G. F. Hamberger, U. Siart, and T. F. Eibert, "A polarimetric 76–79 GHz radar-frontend for target classification in automotive use," in *European Microwave Week (EuMW) - 13th European Radar Conference (EuRAD) 2016*. London, UK: IEEE, 10 2016, pp. 346–349.

[36] S. Trummer, G. F. Hamberger, R. Koerber, U. Siart, and T. F. Eibert, "Performance analysis of 79 GHz polarimetric radar sensors for autonomous driving," in *European Microwave Week (EuMW) - 14th European Radar Conference (EuRAD) 2017*. Nuremberg, Germany: IEEE, 10 2017, pp. 41–44.

[37] ——, "Autonomous driving features based on 79 GHz polarimetric radar data," in *European Microwave Week (EuMW) - 15th European Radar Conference (EuRAD) 2018*. Madrid, Spain: IEEE, 9 2018, pp. 18–21.

[38] A. A. Alaqeel, A. A. Ibrahim, A. Y. Nashashibi, K. Sarabandi, and H. N. Shaman, "The phenomenology of radar backscattering response of vehicles at 222 GHz," in *IEEE International Geoscience and Remote Sensing Symposium (IGARSS) 2017*, vol. 2017-July. Fort Worth, TX, USA: IEEE, 7 2017, pp. 350–352.

[39] A. A. Alaqeel, A. A. Ibrahim, A. Y. Nashashibi, H. N. Shaman, and K. Sarabandi, "A phenomenological study of radar backscatter response of vehicles for the next generation automotive radars," in *IEEE International Geoscience and Remote Sensing Symposium (IGARSS) 2018*. Valencia, Spain: IEEE, 7 2018, pp. 4063–4065.

[40] ——, "Experimental characterization of multi-polarization radar backscatter response of vehicles at J-Band," *IEEE Transactions on Intelligent Transportation Systems*, vol. 20, no. 9, pp. 3337–3350, 11 2019.

[41] T. Visentin, J. Hasch, and T. Zwick, "Polarimetric RCS measurements of selected two-wheeled vehicles for automotive radar," in *European Microwave Week (EuMW) - 14th European Radar Conference (EuRAD) 2017*. Nuremberg, Germany: IEEE, 10 2017, pp. 53–56.

[42] T. Visentin, "Polarimetric radar for automotive applications," Ph.D. dissertation, Karlsruher Institut für Technologie, 2018.

[43] K. E. Dungan, C. Austin, J. Nehrbass, and L. C. Potter, "Civilian vehicle radar data domes," *Proceedings of SPIE - The International Society for Optical Engineering*, vol. 7699, 4 2010.

[44] J. F. Tilly, F. Weishaupt, O. Schumann, J. Klappstein, J. Dickmann, and G. Wanielik, "Polarimetric signatures of a passenger car," in *Kleinheubach Conference (KHB) 2019*. Miltenberg, Germany: IEEE, 9 2019, pp. 6–9.

[45] J. F. Tilly, F. Weishaupt, O. Schumann, J. Dickmann, and G. Wanielik, "Road user classification with polarimetric radars," in *European Microwave Week (EuMW) - 17th European Radar Conference (EuRAD) 2020*. Utrecht, the Netherlands: IEEE, 1 2021, pp. 112–115.

[46] T. Visentin, J. Hasch, and T. Zwick, "Analysis of multipath and DOA detection using a fully polarimetric automotive radar," in *European Microwave Week (EuMW) - 14th European Radar Conference (EuRAD) 2017*. Nuremberg, Germany: IEEE, 10 2017, pp. 45–48.

[47] H. Iqbal, F. Bogelsack, and C. Waldschmidt, "Polarimetric RCS analysis of traffic objects," in *European Microwave Week (EuMW) - 14th European Radar Conference (EuRAD) 2017*. Nuremberg, Germany: IEEE, 10 2017, pp. 49–52.

[48] F. Weishaupt, K. Werber, J. F. Tilly, J. Dickmann, and D. Heberling, "Polarimetric radar for automotive self-localization," in *20th International Radar Symposium (IRS) 2019*. Ulm, Germany: IEEE, 6 2019.

[49] B. R. Mahafza and A. Z. Elsherbeni, *MATLAB Simulations for radar systems design*. Chapman & Hall/CRC CRC Press LLC, 2004.

[50] S. Kingsley and S. Quegan, *Understanding radar systems*. SciTech Publishing, Inc., 1999.

[51] S. S. Blackman and R. Popoli, *Desing and analysis of modern track systems*. Norwood, MA, USA: Artech House, 1999.

[52] M. Jankiraman, "FMCW Waveform," in *FMCW Radar Design*. Norwood, MA, USA: Artech House, 2018, ch. 2, pp. 19–56.

[53] E. M. Kennaugh, "Polarization properties of radar reflection," Ph.D. dissertation, The Ohio State University, Columbus, OH, USA, 1952.

[54] E. Krogager, "New decomposition of the radar target scattering matrix," *Electronics Letters*, vol. 26, no. 18, pp. 1525–1527, 8 1990.

[55] O. A. Krasnov, L. P. Ligthart, Z. Li, G. P. Babur, Z. Wang, and F. van der Zwan, "PARSAX: High-resolution Doppler-polarimetric FMCW radar with dual-orthogonal signals," in *4th Microwave and Radar Week - 18th International Conference on Microwaves, Radar and Wireless Communications 2010*. Vilnius, Lithuania: IEEE, 2010.

[56] F. Belfiori, O. A. Krasnov, and A. Yarovoy, "Polarimetric channels exploitation for improved target detection: Preliminary experiments with the PARSAX radar system," in *15th International Radar Symposium (IRS) 2014*. Gdansk, Poland: IEEE, 2014, pp. 1–4.

[57] O. A. Krasnov, L. P. Ligthart, Z. Li, P. Lys, and F. van der Zwan, "The PARSAX - full polarimetric FMCW radar with dual-orthogonal signals," in *European Microwave Week (EuMW) - 5th European Radar Conference (EuRAD) 2008*. Amsterdam, the Netherlands: IEEE, 2008, pp. 84–87.

[58] G. P. Babur, O. A. Krasnov, and L. P. Ligthart, "Quasi-simultaneous measurements of scattering matrix elements in polarimetric radar with continuous waveforms providing high-level isolation in radar channels," in *European Microwave Week (EuMW) - 6th European Radar Conference (EuRAD) 2009*. Rome, Italy: IEEE, 10 2009.

[59] G. P. Babur, O. A. Krasnov, A. Yarovoy, and P. Aubry, "Nearly orthogonal waveforms for MIMO FMCW Radar," *IEEE Transactions on Aerospace and Electronic Systems*, vol. 49, no. 3, pp. 1426–1437, 7 2013.

[60] C. K. Alexander and M. N. O. Sadiku, *Fundamentals of electric circuits*, 5th ed. Singapore: McGraw-Hill, 2013.

[61] H. Rohling, "Radar CFAR thresholding in clutter and multiple target situations," *IEEE Transactions on Aerospace and Electronic Systems*, vol. AES-19, no. 4, pp. 608–621, 7 1983.

[62] P. Soille, *Morphological image analysis - principles and applications*, 2nd ed. Springer-Verlag Berlin Heidelberg, 2004.

[63] H. Mitchell, *Multi-Sensor Data Fusion*, 1st ed. Berlin, Heidelberg: Springer Berlin Heidelberg, 2007.

[64] L. M. Novak, M. B. Seciitin, and M. J. Cardullo, "Studies of target detection algorithms that use polarimetric radar data," *IEEE Transactions on Aerospace and Electronic Systems*, vol. 25, no. 2, pp. 150–165, 3 1989.

[65] R. Chaney, M. Burl, and L. M. Novak, "On the performance of polarimetric target detection algorithms," in *IEEE International Conference on Radar 1990*. Arlington, VA, USA: IEEE, 5 1990.

[66] C. Fei, T. Liu, G. A. Lampropoulos, and V. Anastassopoulos, "Markov chain CFAR detection for polarimetric data using data fusion," in *16th International Conference on Digital Signal Processing*. Santorini, Greece: IEEE, 7 2009.

[67] S. Nagesh, "Robust feature extraction algorithm for analysis of radar targets using multi-object tracking on range-velocity space," Delft University of Technology, Delft, Tech. Rep., 2019.

[68] M. Ester, H.-P. Kriegel, J. Sander, and X. Xu, "A density-based algorithm for discovering clusters in large spatial databases with noise," in *2nd International Conference on Knowledge Discovery and Data Mining*. Portland, OR, USA: AAAI Press, 8 1996, pp. 226–231.

[69] L. Zhang, Z. Li, W. Liu, W. Qu, and Y. Wu, "An efficient density-based clustering for multi-dimensional database," in *4th International Conference on Information, Cybernetics and Computational Social Systems (ICCSS) 2017*. Dalian, China: IEEE, 7 2017, pp. 361–366.

[70] M. Xia, W. Yi, S. Li, G. Cui, L. Kong, and Y. Huang, "A polarization information aided probabilistic data association for target tracking in polarimetric radar system," in *IEEE Radar Conference 2015*. Arlington, VA, USA: IEEE, 6 2015, pp. 1182–1187.

[71] S. S. Blackman, "Multiple hypothesis tracking for multiple target tracking," *IEEE Aerospace and Electronic Systems Magazine*, vol. 19, no. 1, pp. 5–18, 1 2004.

[72] K. Li, B. Habtemariam, R. Tharmarasa, M. Pelletier, and T. Kirubarjan, "Multitarget tracking with Doppler ambiguity," *IEEE Transactions on Aerospace and Electronic Systems*, vol. 49, no. 4, pp. 2640–2656, 10 2013.

[73] S. S. Blackman, *Multiple target tracking with radar application*. Norwood, MA, USA: Artech House, 1986.

[74] W. R. Blanding, P. K. Willett, Y. Bar-Shalom, and S. P. Coraluppi, "Multisensor track management for targets with fluctuating SNR," *IEEE Transactions on Aerospace and Electronic Systems*, vol. 45, no. 4, pp. 1275–1292, 10 2009.

[75] A. Wald, "Sequential Tests of Statistical Hypotheses," *The Annals of Mathematical Statistics*, vol. 16, no. 2, pp. 117–186, 6 1945.

[76] E. Alpaydın, *Introduction to Machine Learning*, 2nd ed., T. Dietterich, Ed. London, UK: Massachusetts Institute of Technology, 2010.

[77] N. Scheiner, N. Appenrodt, J. Dickmann, and B. Sick, "Radar-based feature design and multiclass classification for road user recognition," in *IEEE Intelligent Vehicles Symposium (IV) 2018*. Changshu, China: IEEE, 6 2018, pp. 779–786.

[78] A. G. Arguello and D. Berges, "Radar classification for traffic intersection surveillance based on micro-Doppler signatures," in *European Microwave Week (EuMW) - 15th European Radar Conference (EuRAD) 2018*. Madrid, Spain: IEEE, 9 2018, pp. 186–189.

[79] S. R. Cloude and E. Pettier, "A review of target decomposition theorems in radar polarimetry," *IEEE Transactions on Geoscience and Remote Sensing*, vol. 34, no. 2, pp. 498–518, 3 1996.

[80] Y. Li and Y. Q. Jin, "Imaging and structural feature decomposition of a complex target using multi-aspect polarimetric scattering," *Science China Information Sciences*, vol. 59, no. 8, 8 2016.

[81] T. Long, L. Zhang, Y. Li, and Y. Wang, "Geometrical structure classification of target HRRP scattering centers based on dual polarimetric H/α features," *IEEE Access*, vol. 7, pp. 141 679–141 688, 10 2019.

[82] S. Demirci, O. Kirik, and C. Ozdemir, "Interpretation and analysis of target scattering from fully-polarized ISAR images using Pauli decomposition scheme for target recognition," *IEEE Access*, vol. 8, pp. 155 926–155 938, 8 2020.

[83] J.-S. Lee, W. M. Boerner, D. Schuler, T. Ainsworth, I. Hajnsek, K. Papathanassiou, and E. Lüneburg, "A review of polarimetric SAR algorithms and their applications," *Journal of Photogrammetry and Remote Sensing*, vol. 9, no. 3, pp. 31–80, 2004.

[84] J. Han, M. Kamber, and J. Pei, "Cluster Analysis: Basic Concepts and Methods," in *Data Mining: Concepts and Techniques*, 3rd ed. Burlington, MA, USA: Morgan Kaufmann, 2012, ch. 10, pp. 443–495.

[85] R. G. Lawson and P. C. Jurs, "New index for clustering tendency and its application to chemical problems," *Journal of Chemical Information and Computer Sciences*, vol. 30, no. 1, pp. 36–41, 2 1990.

[86] T. Calinski and J. Harabasz, "A dendrite method for cluster analysis," *Communications in Statistics - Theory and Methods*, vol. 3, no. 1, pp. 1–27, 1974.

[87] D. L. Davies and D. W. Bouldin, "A Cluster Separation Measure," *IEEE Transactions on Pattern Analysis and Machine Intelligence*, vol. PAMI-1, no. 2, pp. 224–227, 4 1979.

[88] A. D. M. Martins, A. D. Neto, J. D. De Melo, and J. A. F. Costa, "Clustering using neural networks and Kullback-Leibler divergency," in *IEEE International Joint Conference on Neural Networks 2004*. Budapest, Hungary: IEEE, 7 2004, pp. 2813–2817.

A

PARSAX System and Signal Processing

A.1. PARSAX Block Diagram

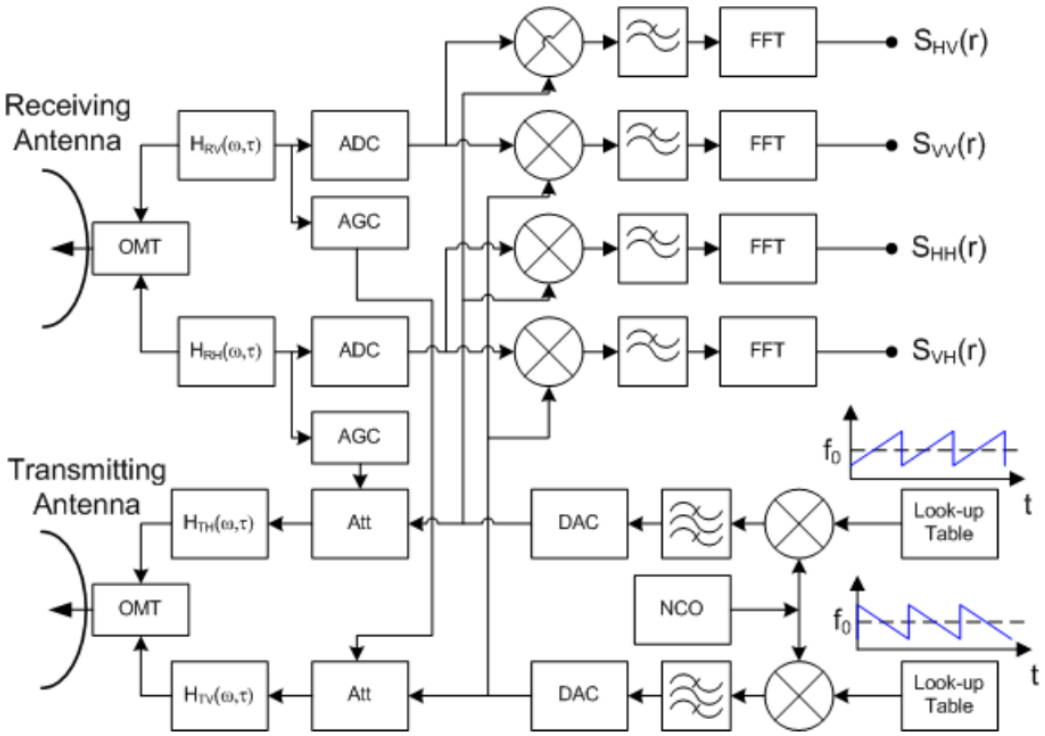

Figure A.1: Block diagram of the fully polarimetric PARSAX radar [55]

A.2. Range-time plots of raw data

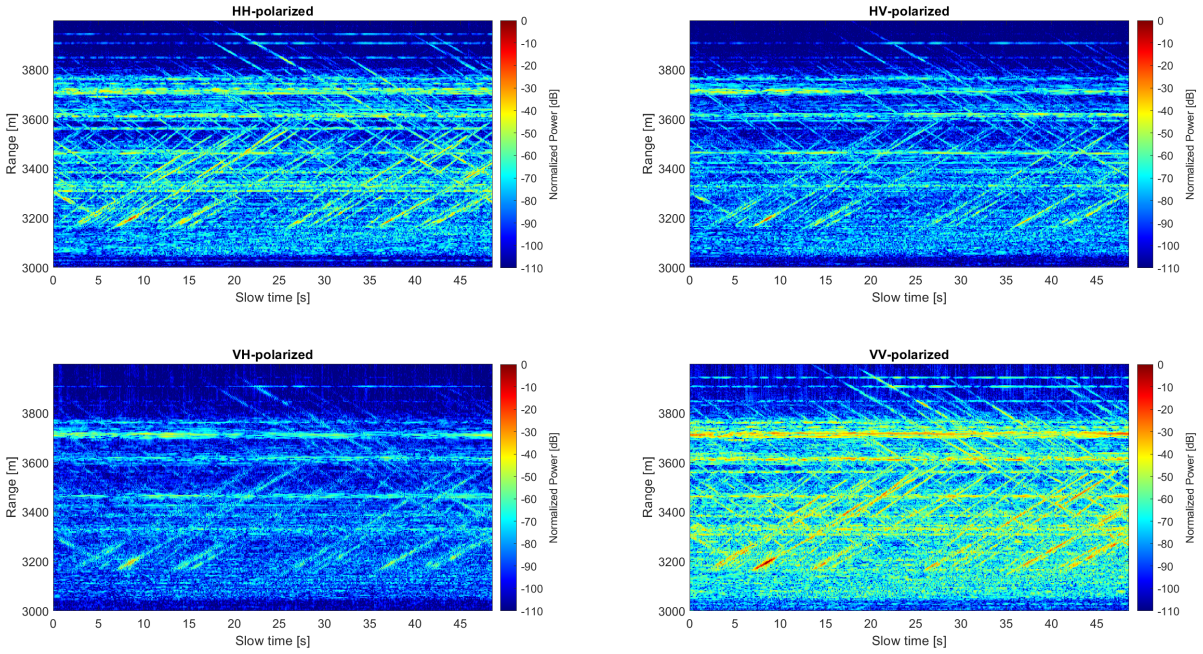

Figure A.2: Range-time plots of raw data

A.3. Range-Doppler plots of raw data

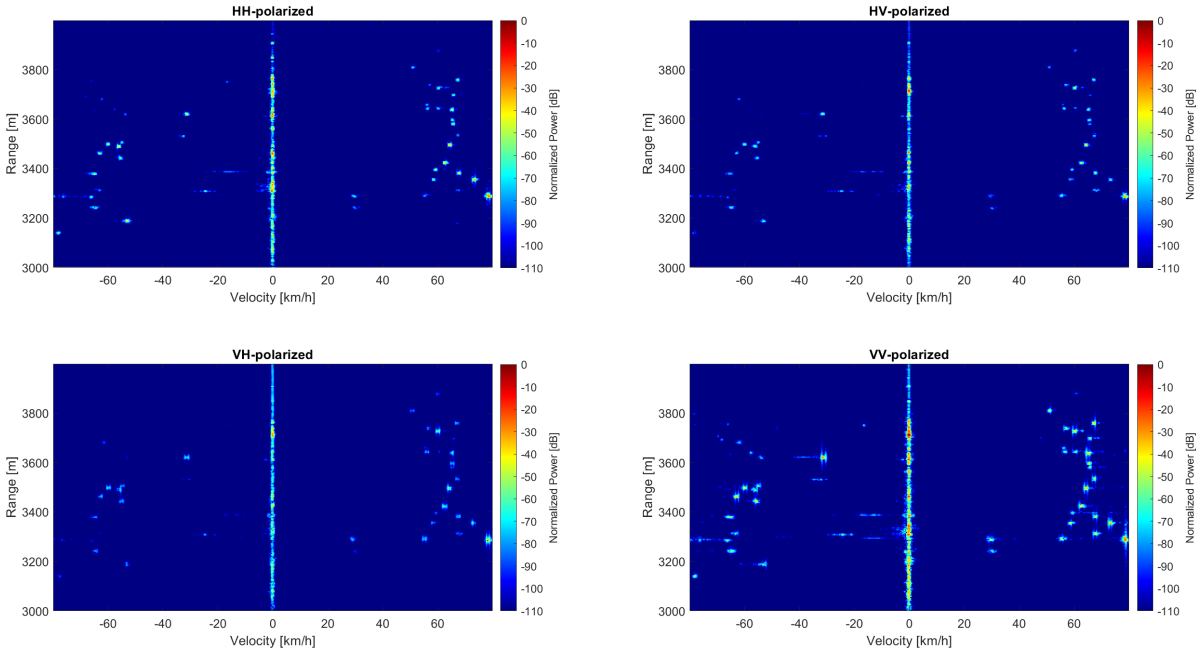

Figure A.3: Range-Doppler plots of raw data

A.4. Range-time plots of filtered data

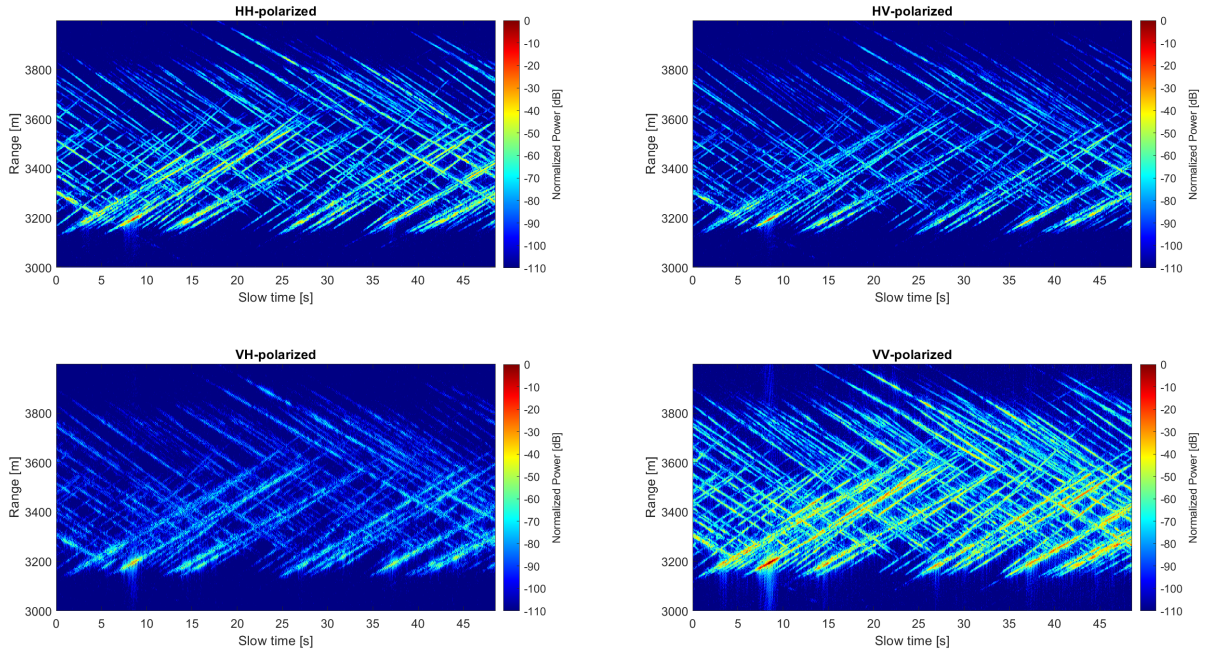

Figure A.4: Range-time plots of filtered data

A.5. Range-Doppler plots of filtered data

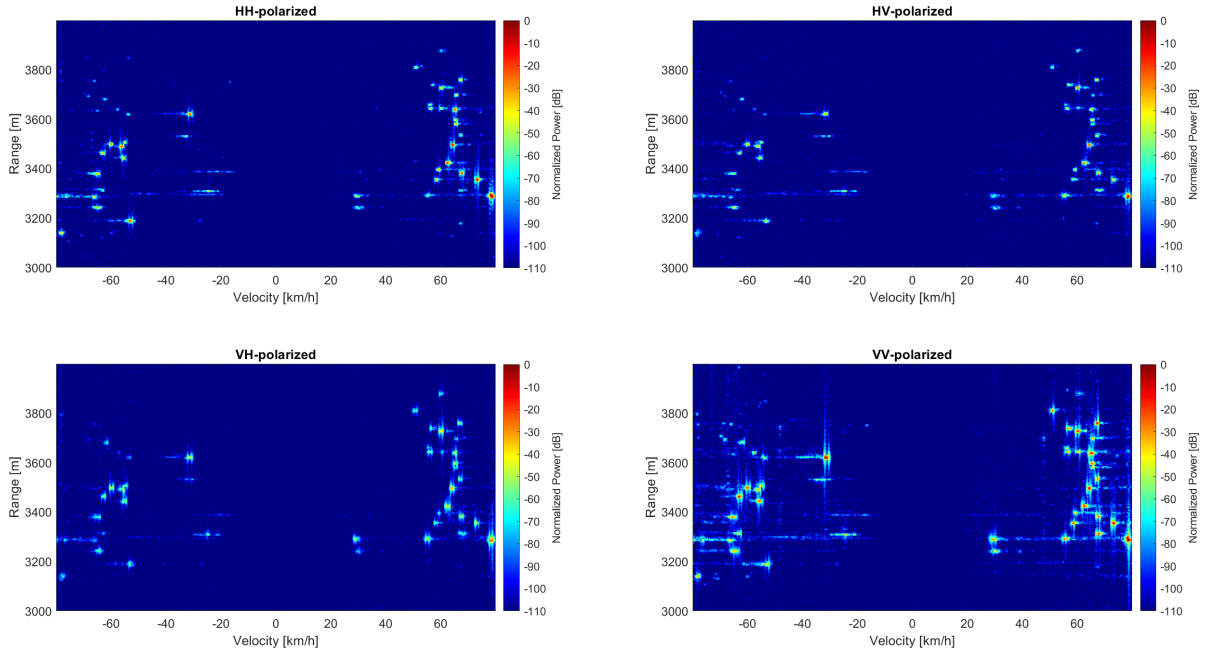

Figure A.5: Range-Doppler plots of filtered data

A.6. Noise statistics

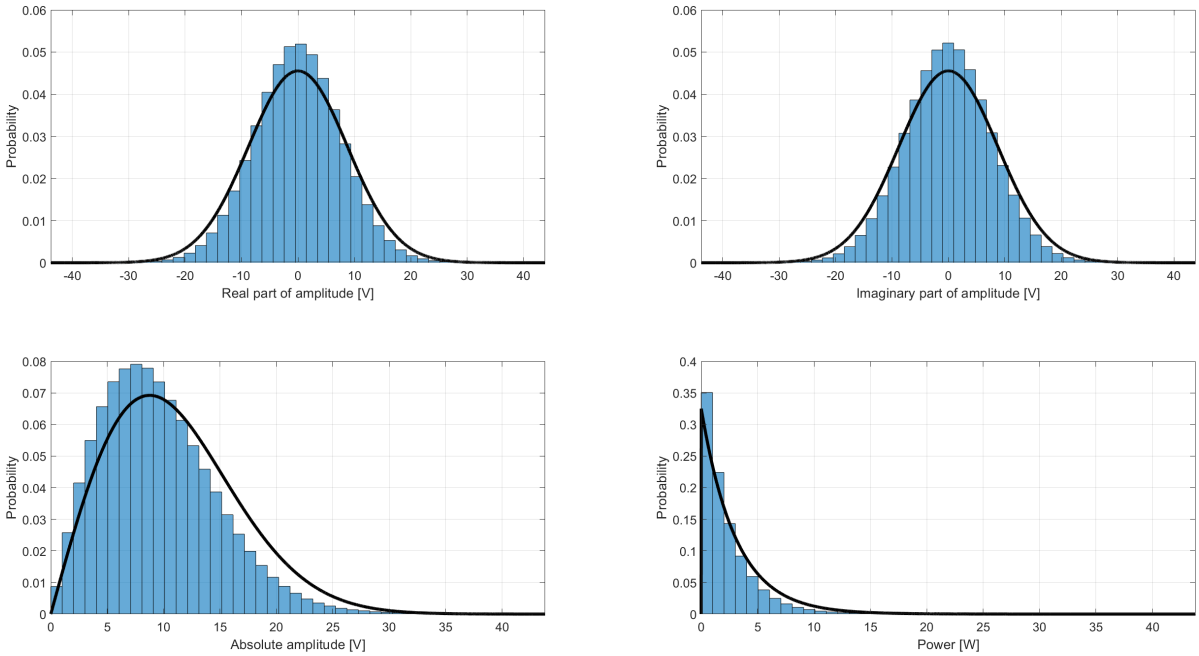

Figure A.6: Noise statistics in HV-polarized state

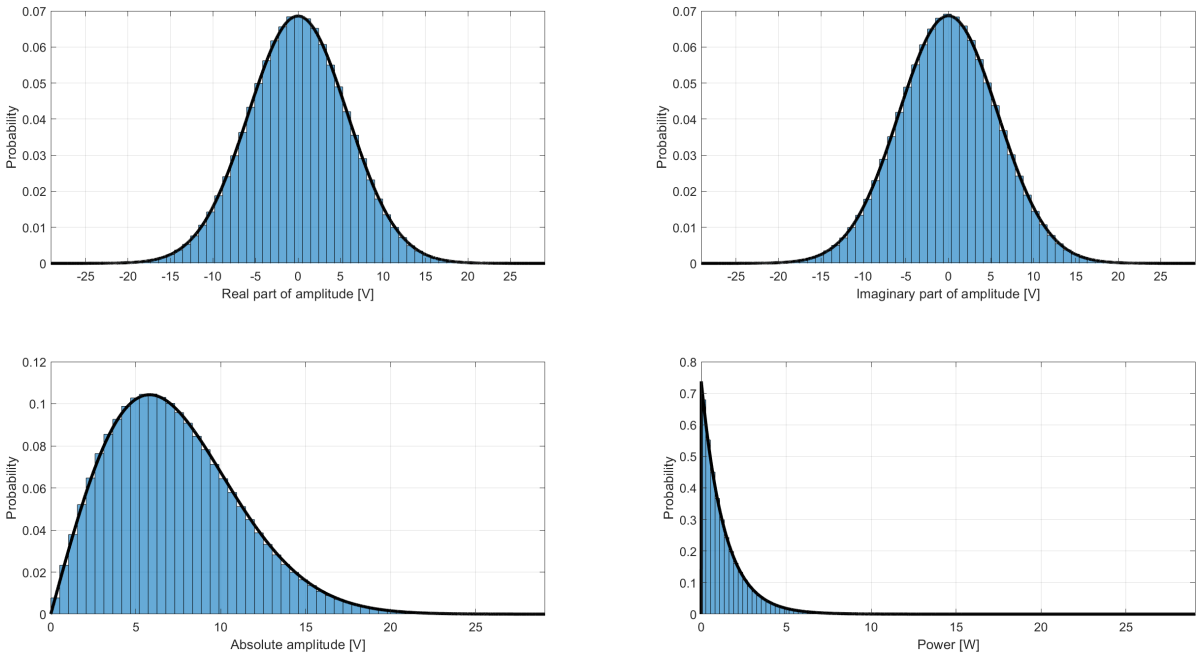

Figure A.7: Noise statistics in VH-polarized state

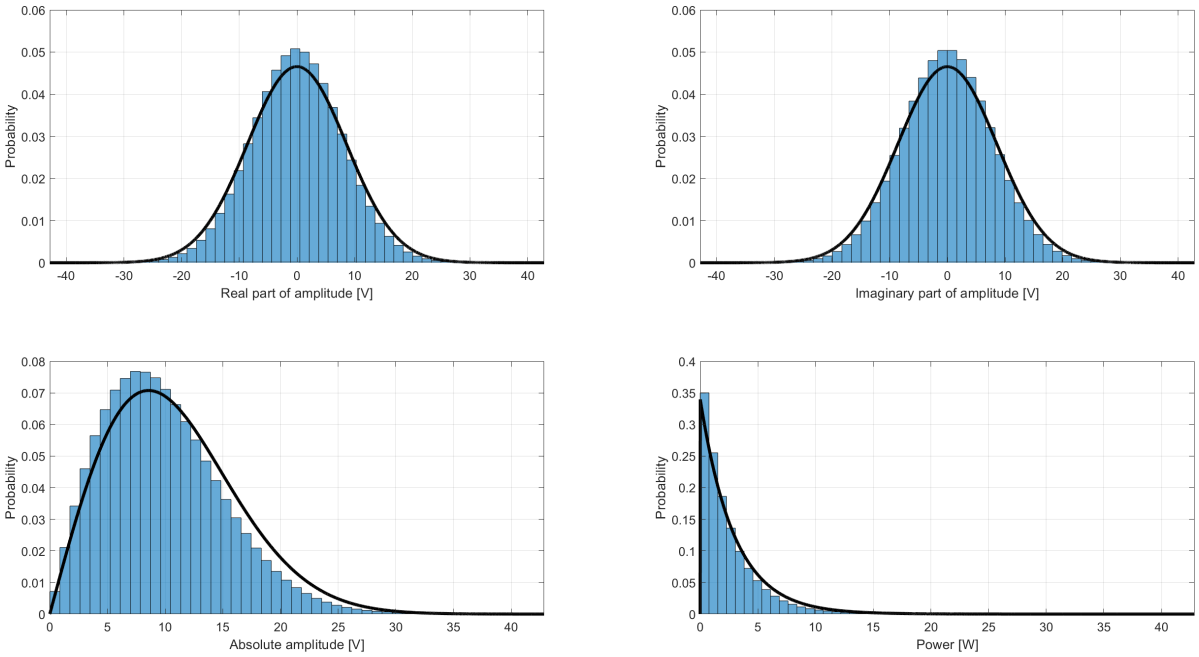

Figure A.8: Noise statistics in VV-polarized state

B

CFAR detection maps

B.1. Range-Doppler plots after OS-CFAR detector

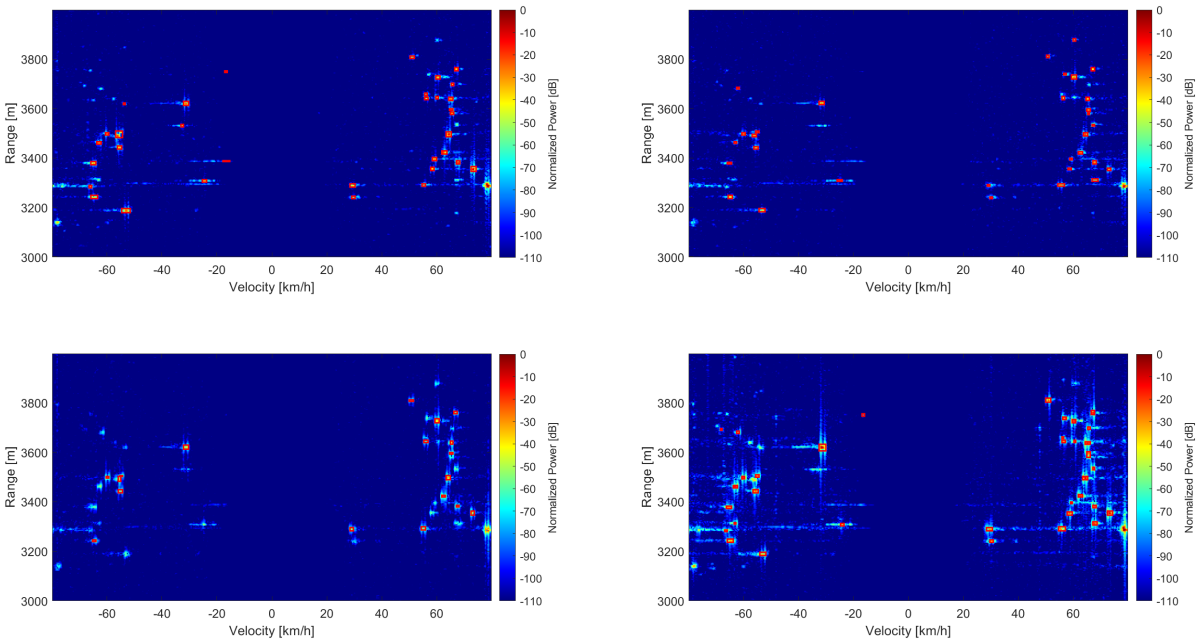

Figure B.1: Range-Doppler plots after applying the OS-CFAR detector

B.2. Detection maps after OS-CFAR detector

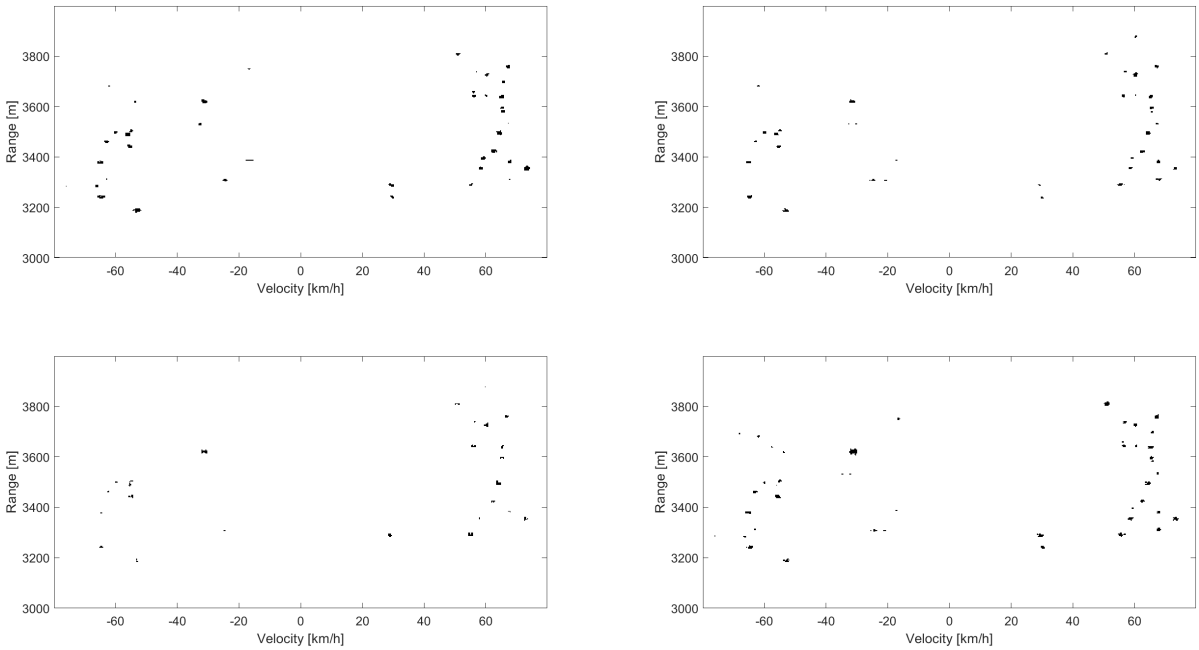

Figure B.2: Detection maps as a result of the OS-CFAR detector

C

Signal- and data processing overview

See next page for an enlarged version of the overview of the signal- and data processing chain.

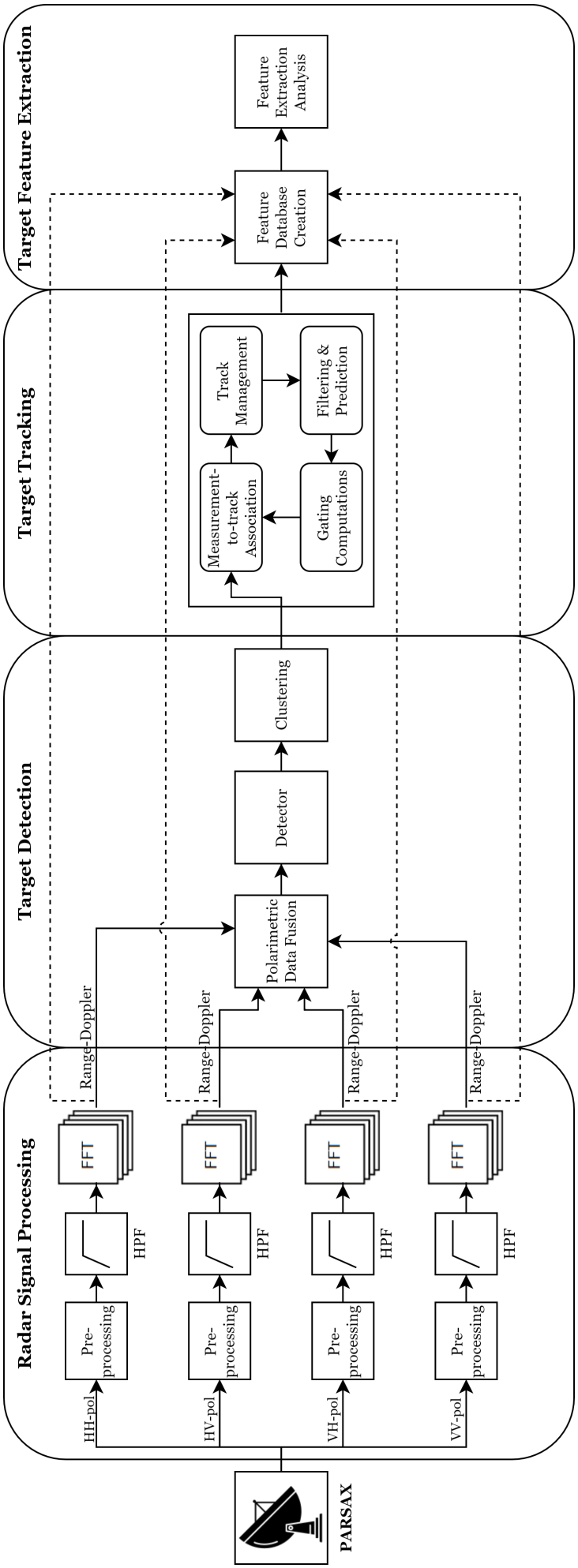
Target Feature Extraction
Feature Extraction Analysis
Feature Database Creation
Target Tracking
Track Management
Filtering & Prediction
Measurement-to-track Association
Gating Computations
Target Detection
Clustering
Detector
Polarimetric Data Fusion
Range-Doppler
Range-Doppler
Range-Doppler
Range-Doppler
Radar Signal Processing
FFT
FFT
FFT
FFT
HPF
HPF
HPF
HPF
Pre-processing
Pre-processing
Pre-processing
Pre-processing
HH-pol
HV-pol
VH-pol
VV-pol
PARSAX

D

Feature extraction analysis

D.1. Normalization by range

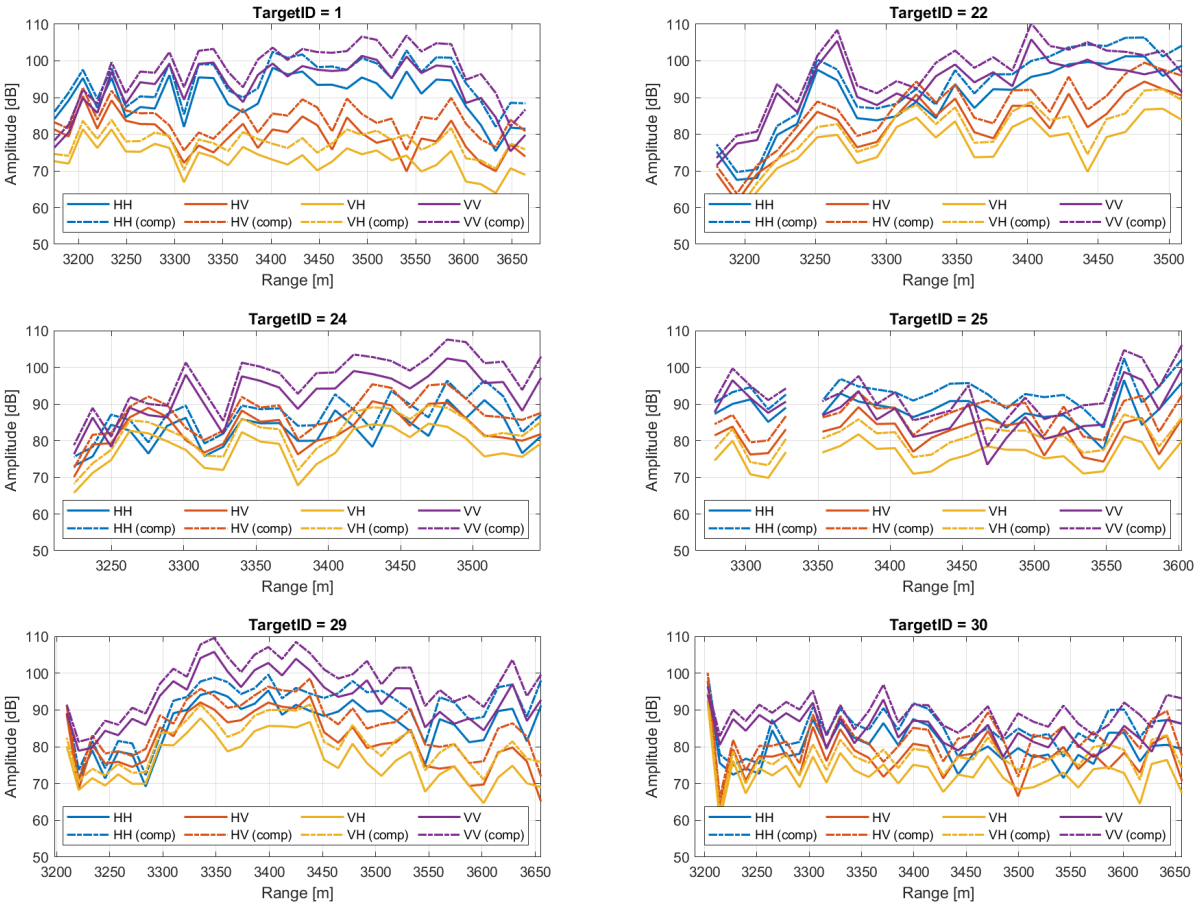

Figure D.1: Amplitude over range for 6 different targets without (solid) and with (striped) range normalization

D.2. Clustering quality after preliminary classification (amplitude-based features)

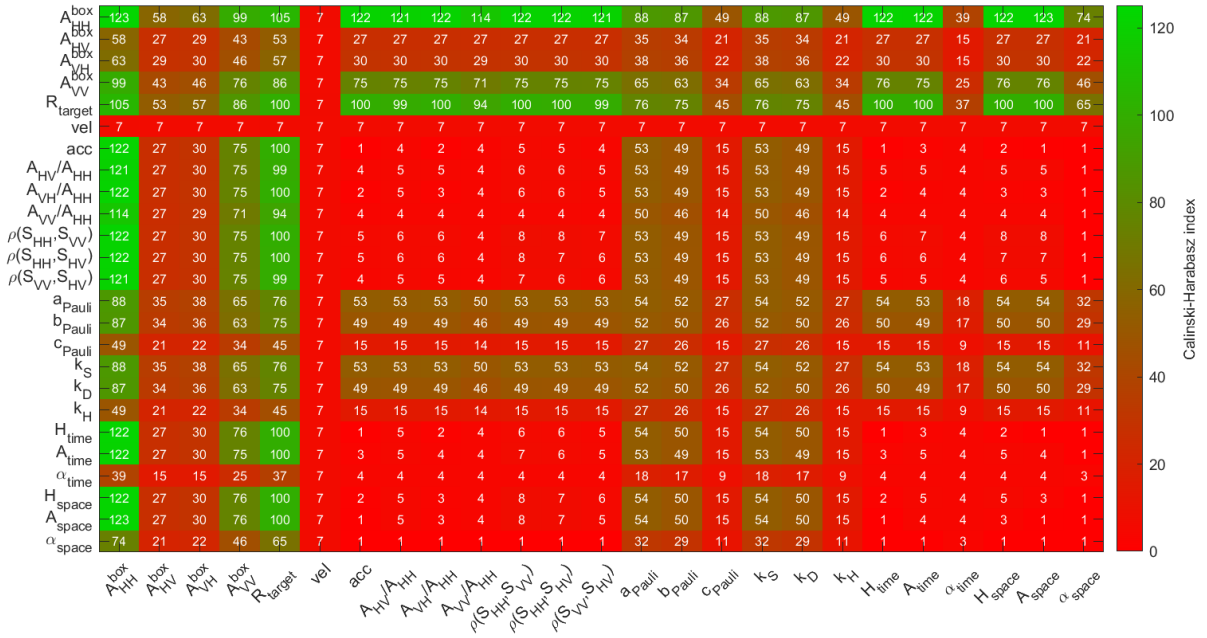

Figure D.2: Calinski-Harabasz index coefficient matrix, indicating the resulted coefficient values for all possible feature pairs when labeling the data based on the maximum amplitudes $|S_{HH}|$ and $|S_{VV}|$ of the target box (see Fig. 4.2a)

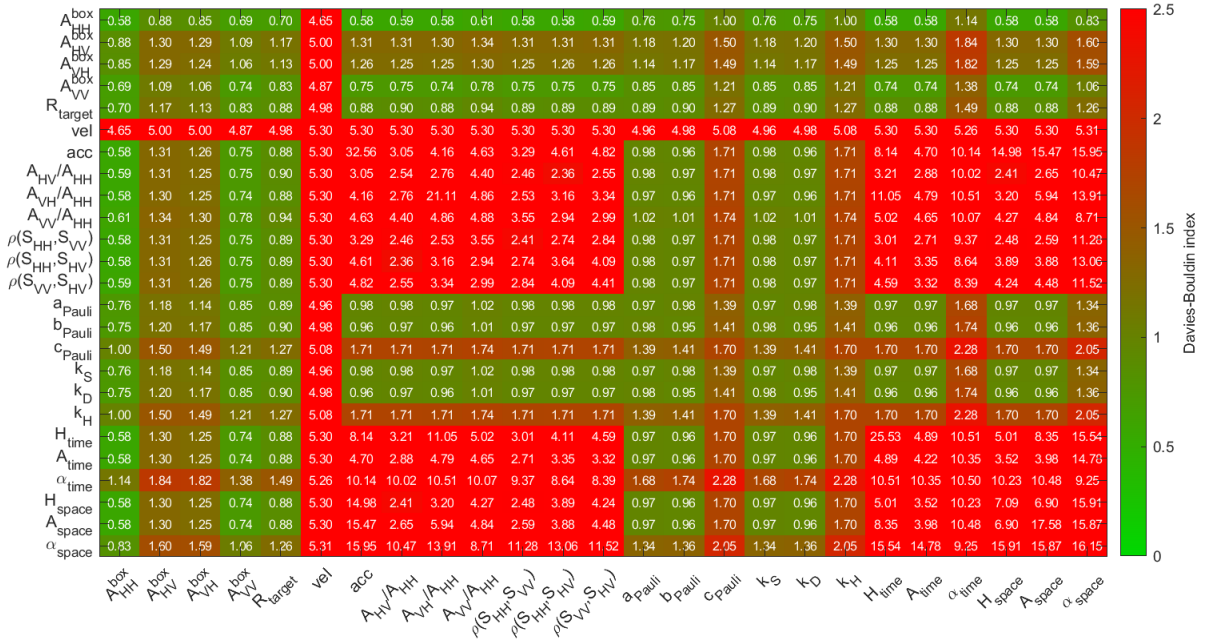

Figure D.3: Davies-Bouldin index matrix, indicating the resulted coefficient values for all possible feature pairs when labeling the data based on the maximum amplitudes $|S_{HH}|$ and $|S_{VV}|$ of the target box (see Fig. 4.2a)

D.3. Clustering quality after preliminary classification (correlation-based features)

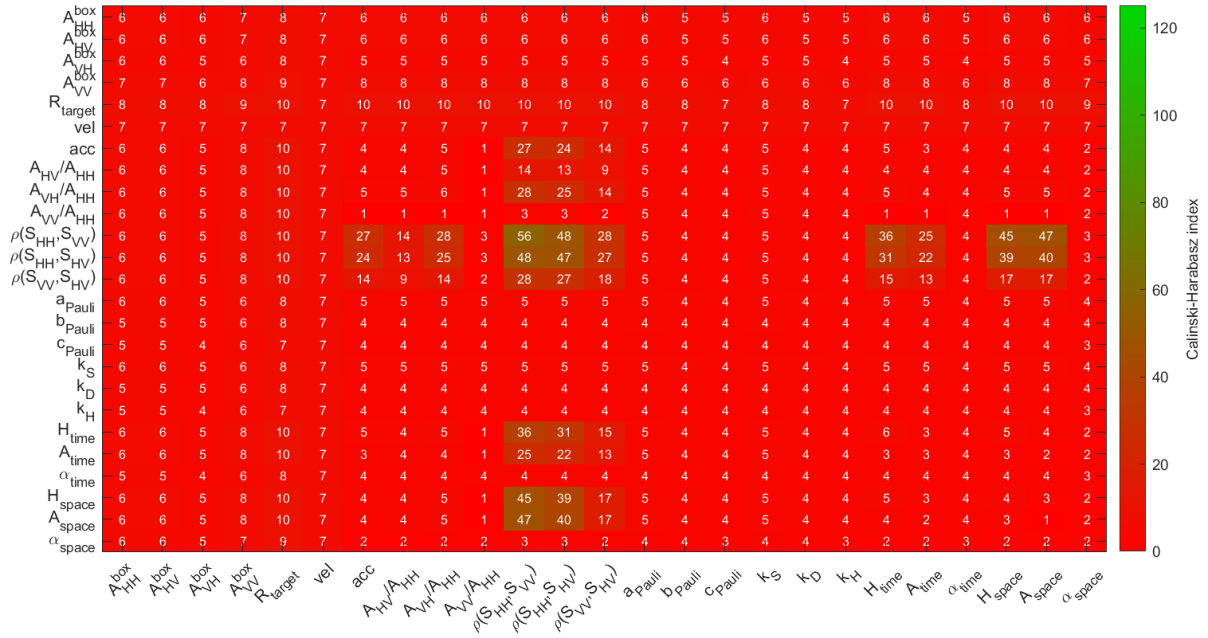

Figure D.4: Calinski-Harabasz index coefficient matrix, indicating the resulted coefficient values for all possible feature pairs when labeling the data based on the clusters originating from $\rho(S_{HH}, S_{VV})$ vs. $\rho(S_{HH}, S_{HV})$ (see Fig. 4.18a)

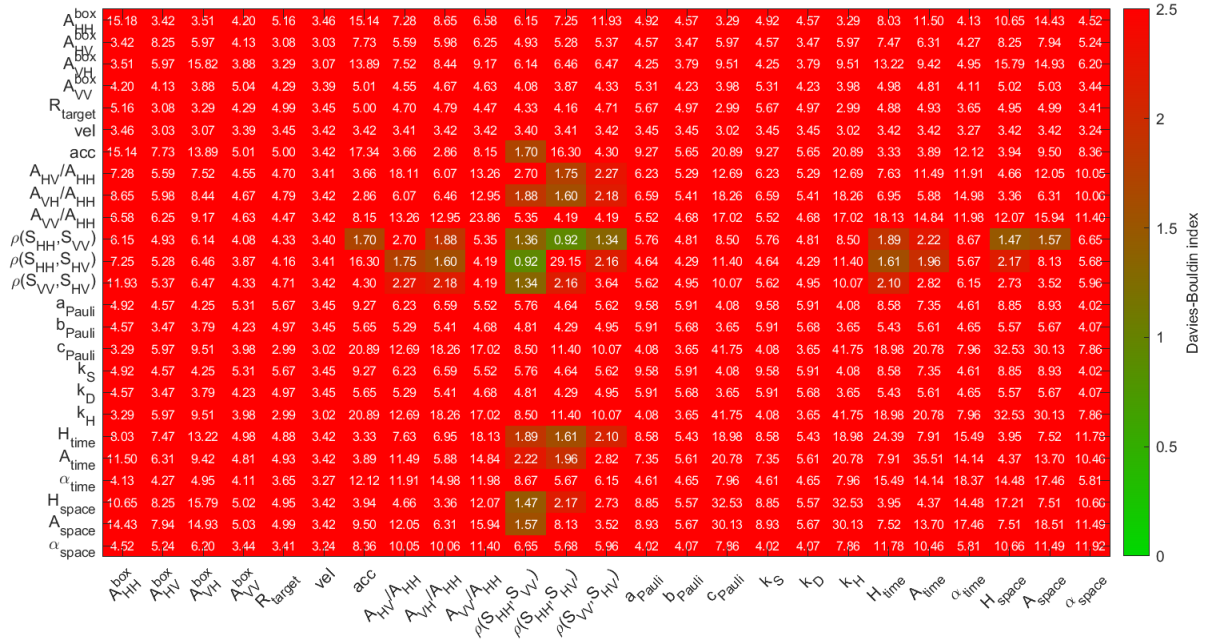

Figure D.5: Davies-Bouldin index matrix, indicating the resulted coefficient values for all possible feature pairs when labeling the data based on the clusters originating from $\rho(S_{HH}, S_{VV})$ vs. $\rho(S_{HH}, S_{HV})$ (see Fig. 4.18a)

D.4. Clustering quality after preliminary classification (entropy-based features)

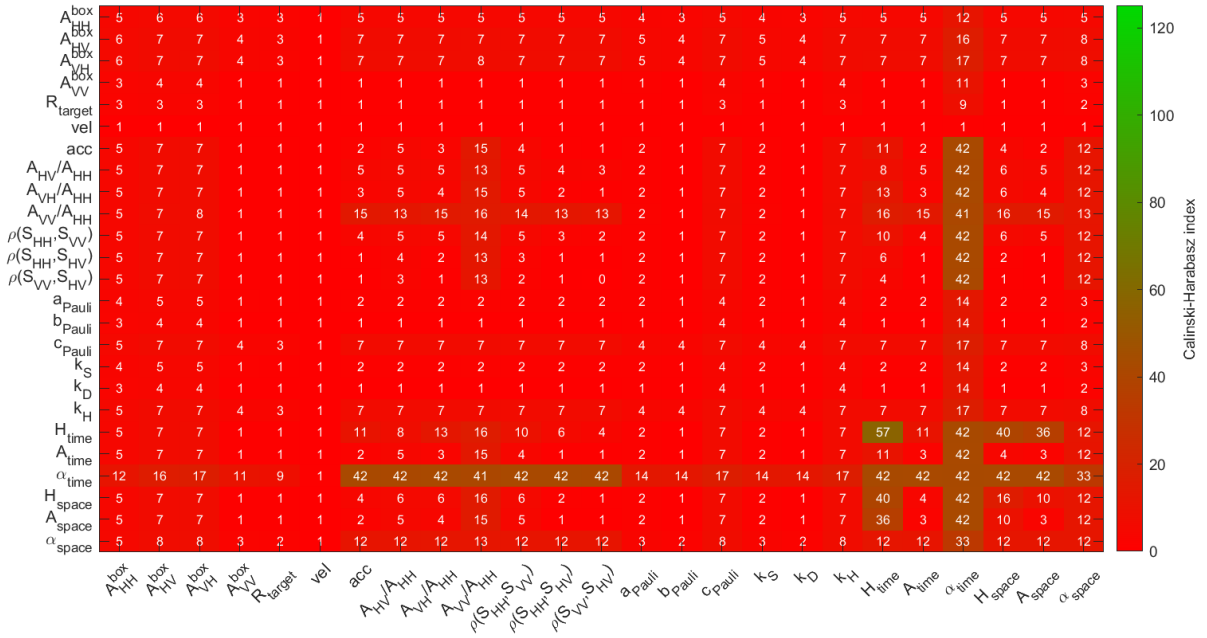

Figure D.6: Calinski-Harabasz index coefficient matrix, indicating the resulted coefficient values for all possible feature pairs when labeling the data based on the clusters originating from $\overline{H}_{time}$ and $\overline{\alpha}_{time}$ (see Fig. 4.26a)

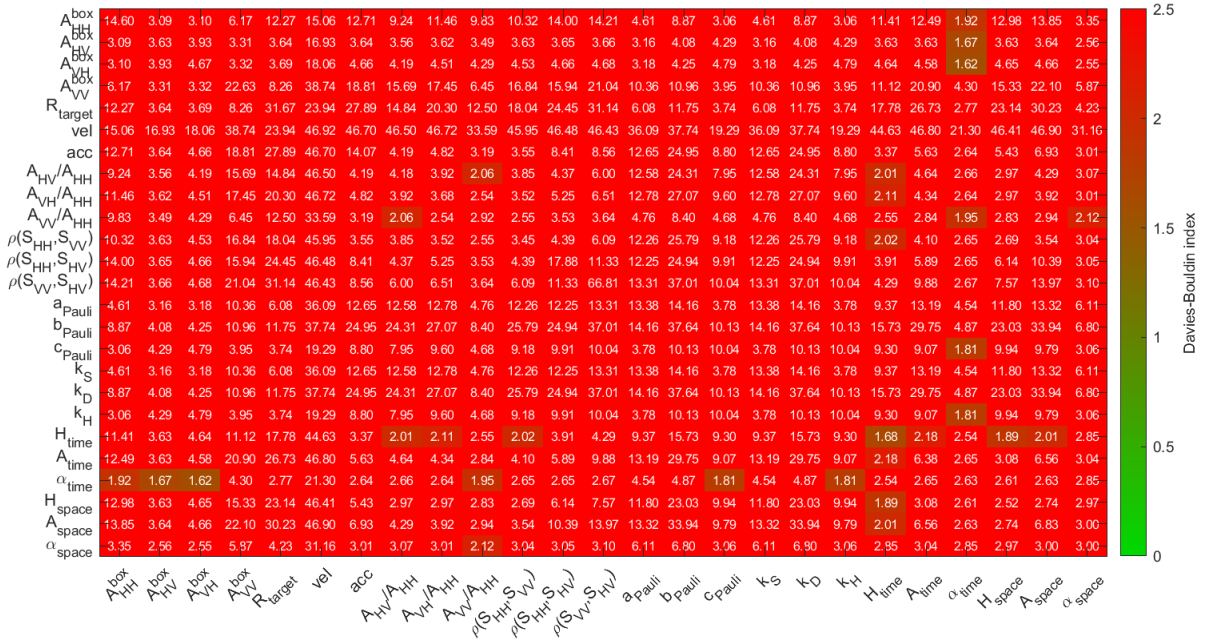

Figure D.7: Davies-Bouldin index matrix, indicating the resulted coefficient values for all possible feature pairs when labeling the data based on the clusters originating from $\overline{H}_{time}$ and $\overline{\alpha}_{time}$ (see Fig. 4.26a)

D.5. Clustering quality of target and clutter features

Figure D.8: Calinski-Harabasz index coefficient matrix, indicating the resulted coefficient values for all possible feature pairs when labeling the data based on the clusters originating from

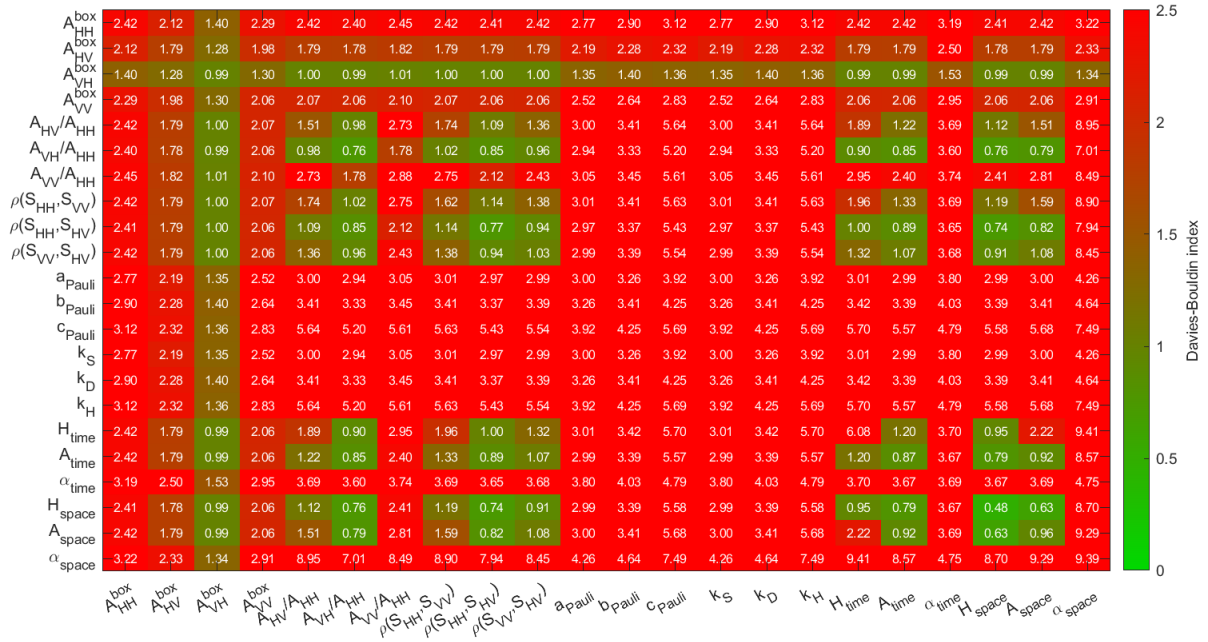

Figure D.9: Davies-Bouldin index matrix, indicating the resulted coefficient values for all possible feature pairs when labeling the data based on the clusters originating from

D.6. Clustering results of target and clutter features for similar data sets

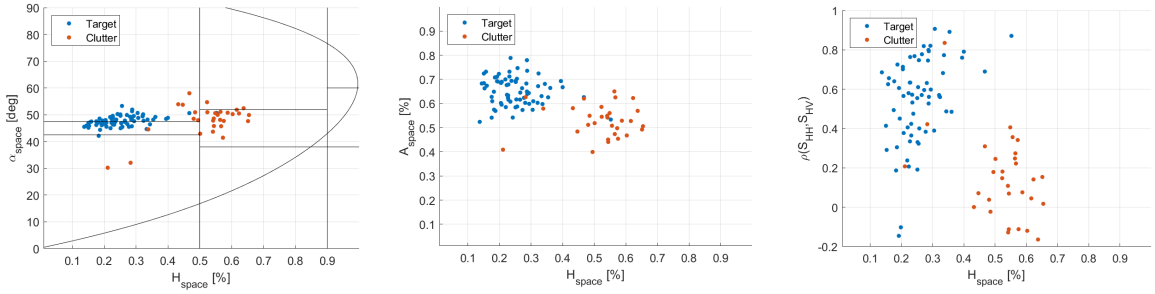

(a) (b) (c)

Figure D.10: Feature spaces with the entropy-based and correlation-based features of target scattering and static clutter scattering (as a result of data set 2)

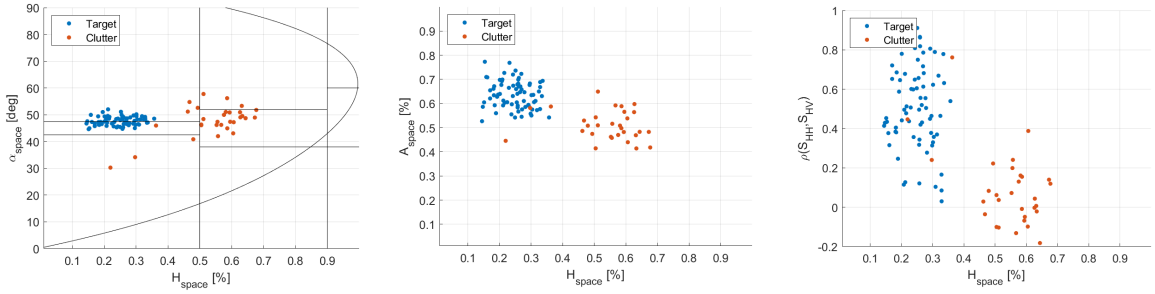

(a) (b) (c)

Figure D.11: Feature spaces with the entropy-based and correlation-based features of target scattering and static clutter scattering (as a result of data set 3)

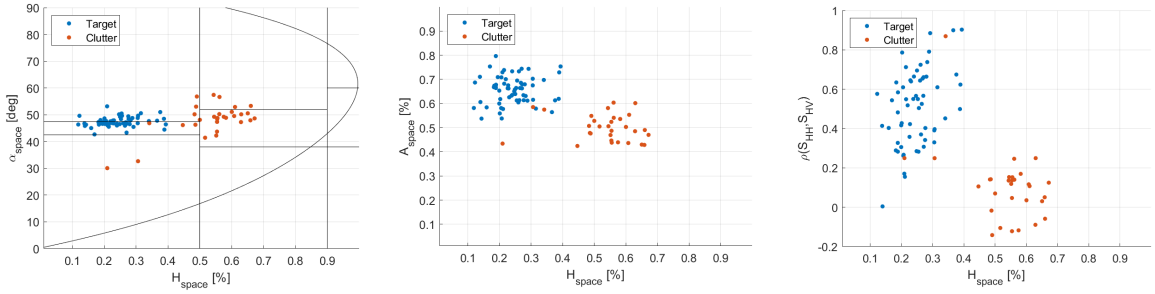

(a) (b) (c)

Figure D.12: Feature spaces with the entropy-based and correlation-based features of target scattering and static clutter scattering (as a result of data set 4)

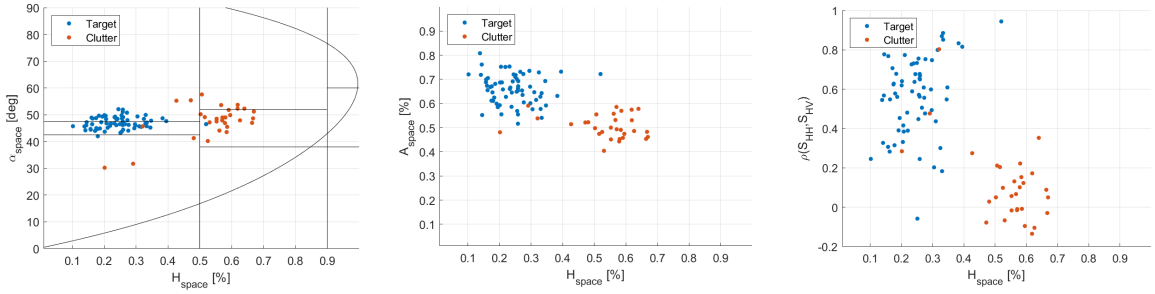

(a) (b) (c)

Figure D.13: Feature spaces with the entropy-based and correlation-based features of target scattering and static clutter scattering (as a result of data set 5)